Delft University of Technology

The interplay between wind and clouds in the trades

Helfer, K.C.

Important note
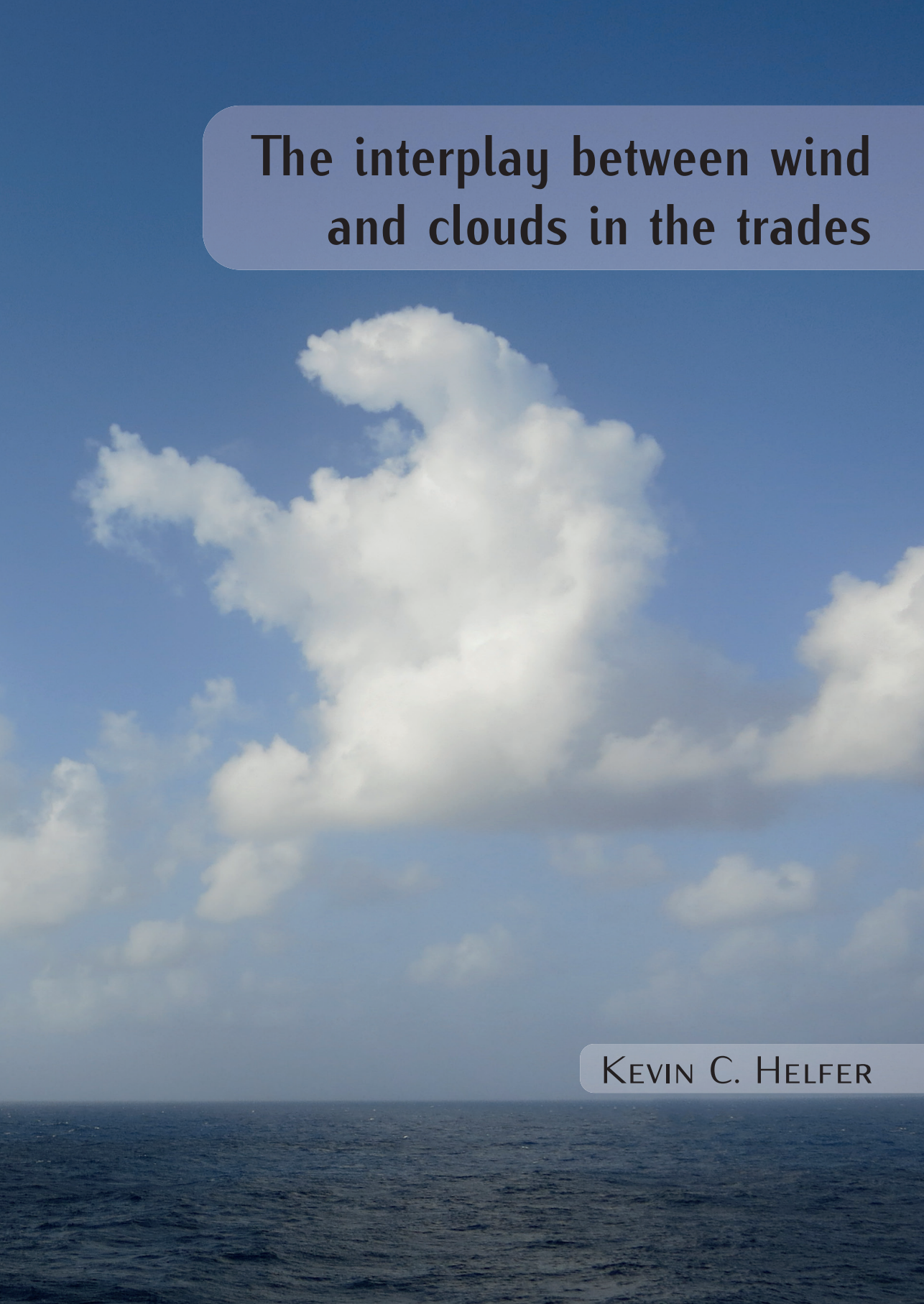To cite this publication, please use the final published version (if applicable).
Please check the document version above.

The interplay between wind and clouds in the trades

KEVIN C. HELFER

The interplay between wind and clouds in the trades

Kevin C. Helfer

The interplay between wind and clouds in the trades

DISSERTATION

for the purpose of obtaining the degree of doctor
at Delft University of Technology
by the authority of the Rector Magnificus
Prof.dr.ir. T.H.J.J. van der Hagen,
chair of the Board for Doctorates,
to be defended publicly on
Wednesday, 22 September 2021 at 12:30

by

Kevin Christopher HELFER

Master of Science in Geophysics,
Westfälische Wilhelms-Universität Münster, Germany,
born in Wipperfürth, Germany

This dissertation has been approved by the promotors.

Composition of the doctoral committee:

Rector Magnificus	chairperson
Prof. Dr. A. P. Siebesma	Delft University of Technology, promotor
Dr. A. A. Nuijens	Delft University of Technology, copromotor

Independent members:

Dr. C. E. Holloway	University of Reading
Prof. Dr. R. A. J. Neggers	University of Cologne
Dr. L. Schlemmer	Deutscher Wetterdienst, Goethe University Frankfurt
Prof. Dr. ir. B. J. H. van de Wiel	Delft University of Technology
Prof. Dr. P. Zuidema	University of Miami
Prof. Dr. ir. H. W. J. Russchenberg	Delft University of Technology, reserve member

Typeset by the author with the LaTeX document preparation system.
Font: Iwona (by Janusz M. Nowacki, GUST Font License)

This is the electronic version of this dissertation.

I remember that, as a kid, I owned a little book that enlisted all the different kinds of clouds and explained how to identify them and what kind of weather to expect from them. I loved learning from this book and telling my friends that we had no rain to fear of those cumulus clouds. I do not recall who gave this book to me, but if one of the readers thinks that they were the one: Thanks a lot, you are probably the reason why you are now reading this thesis!

As time passed on, the little book got lost and so did the simple thermometer I had nicked from my mum's freezer and the pine cone hygrometer. But the interest and awe for the physics of the natural world remained.

Contents

Summary

Cumulus clouds ('fair-weather clouds') form as a result of atmospheric convection and have vertical extents between a few hundred metres (humilis species) and several kilometres (congestus species). They are a major source of uncertainty in the estimation of climate sensitivity by climate models. In order to reach more agreement in cloud changes due to global warming as predicted by different climate models, a better understanding of the physics of these clouds is needed. Shallow cumulus clouds are particularly common over the oceans of Earth's trade-wind regions, which are situated roughly between the 10° and 30° parallels on both hemispheres and are characterised by steady easterly surface winds. These winds are part of the Hadley cell, a large-scale circulation system in which air flows away from the equator at high altitudes and towards the equator near the surface. As a consequence, vertical shear (i.e. vertical differences in wind speed and direction) is common in this region.

While recent studies have shown that (surface) wind speed is an important predictor of cloudiness in this region, little work has been done to elucidate how shear affects clouds. Vice versa, clouds also affect the wind by vertically transporting it. While this convective momentum transport (CMT) undoubtedly plays an important role in the force balance that sets the trade winds, only little is known about the details of how CMT sets the vertical structure of the wind and of the spatial scales of the momentum-transporting eddies. In this thesis, more light is shed on the bidirectional interaction between shallow cumulus convection and the wind. Particular focus is put on the effect of wind shear on convection and on the different spatial scales (convective and turbulent) at which convection affects the wind at different heights.

To this end, results from numerical large-eddy-simulation (LES) experiments are utilised in this thesis. Due to their fine horizontal resolution (of hundreds of metres and less), LES is able to numerically resolve clouds and the largest turbulent eddies explicitly. This leads to a high degree of realism in the simulation. Together with the possibility to artificially simplify the experimental set-up as well as the completeness of the output (in terms of time, space and quantities), this makes LES the ideal tool to understand physical mechanisms in the atmosphere.

To identify and understand the effect of wind shear on cumulus convection, LES experiments were carried out in which typical conditions of the trades were simulated, while the amount of wind shear was systematically varied. In these idealised LES, vertical wind shear effectively limits the deepening of trade-wind convection. Several mechanisms are responsible for this, which depend on the direction of the shear vector (vertically decreasing or increasing wind speed) as well as the altitude at which shear is present. A situation with easterly surface winds that weaken with height and eventually turn westerly is referred to as backward shear, and the opposite situation with easterlies that

strengthen with height is called forward shear. Different directions of wind shear cause different surface winds due to CMT, which in turn affect the surface evaporation: Faster surface winds occur in the presence of forward shear and lead to stronger evaporation of sea water, resulting in deeper convection. Forward shear in the subcloud layer also leads to a spatial separation of precipitative downdrafts and emerging updrafts, as clouds move faster than their subcloud-layer roots; this is favourable for convective development. Conversely, under backward shear, the surface evaporation is weakened and precipitative downdrafts interfere with updrafts, hindering convective deepening. However, once clouds grow to sufficient depths, they may produce precipitation so strong that the associated downdrafts spread out laterally near the surface, forming a distinct circular region of cold air, a cold pool. The spreading of this cold pool can cause uplift at its edges, triggering new convection. Backward shear limits the triggering of such secondary convection at cold-pool fronts, while forward shear facilitates it. Finally, shear of any direction in the cloud layer weakens cloud updrafts through an enhanced downward-oriented pressure perturbation force. The limiting effect of wind shear on cloud depth also affects the thermodynamic properties of the cloud layer: The relative humidity is larger and its decrease near the trade-wind inversion is more distinct if clouds are shallower.

Large-domain LES hindcasts of specific days during the NARVAL measurement campaigns (which took place in December 2013 and August 2016 in the North Atlantic trades) give a uniquely realistic and complete view on the momentum balance of the trade winds. The combined effect of advection resolved by the model — which here is interpreted as CMT — and unresolved small-scale turbulence is to decelerate the wind in a layer that extends from the surface up to a height of about 2 km in winter and 1 km in summer. However, the role of each term in the balance depends on the altitude. CMT itself acts to accelerate near-surface winds, and only due to strong small-scale turbulence, there is still an overall frictious force at this height. Halfway into the subcloud layer, CMT starts to act as a frictious force. This friction is strengthened by small-scale turbulence from cloud base upwards and quickly diminishes with height. Thus, the cumulus clouds themselves do not introduce significant friction at the altitude where the zonal trade-wind jet resides, which coincides with cloud base. In fact, combined with momentum transport against the wind gradient (counter-gradient momentum transport), they may help to sustain this jet.

Overall, wind shear appears to be an important player in setting the typical structure of the trade-wind atmosphere by modulating the depth of convection and may thus even affect cloud-radiative effects. Conversely, convection and turbulence give rise to an overall frictious force on the trade winds. CMT alone acts to accelerate the winds near the surface, which may weaken the Hadley circulation, while in the cloud layer, CMT hardly affects the wind.

Samenvatting

Cumuluswolken („mooiweerwolken") ontstaan door convectie in de atmosfeer en hebben een dikte tussen een paar honderd meters (humilis) en meerdere kilometers (congestus). Zij zijn een belangrijke bron van onzekerheid in de klimaatgevoeligheid voorspeld door verschillende klimaatmodellen. Om deze onzekerheid te verminderen, is er betere kennis van de fysica van deze wolken nodig. Lage cumuluswolken komen bijzonder vaak voor over de oceanen in de passaatregio's van de Aarde. Deze liggen in de subtropen (10–30°) en zijn gekenmerkt door bestendige oostelijke winden. Deze winden maken deel uit van de Hadleycel, een grootschalig circulatiesysteem waarin lucht op grote hoogte van de evenaar wegstroomt en vlak boven het oppervlak terug naar de evenaar stroomt. Daardoor zijn er verticale verschillen in de windsnelheid en windrichting (schering) aan te treffen in deze regio.

Hoewel recente studies aangetoond hebben dat de windsnelheid (aan het oppervlak) een meetbare relatie heeft met de bewolking in deze regio, is er nog weinig onderzoek gedaan naar de invloed van windschering op lage cumuluswolken. Verder beïnvloeden wolken ook de wind zelf door verticale menging. Dit zogenoemde convectieve impulstransport (*convective momentum transport*, CMT) speelt een belangrijke rol in het grootschalige budget van de wind. Maar we weten nog weinig over CMT bijvoorbeeld wat voor een invloed verschillende schalen van turbulente wervels hebben. In deze dissertatie wordt licht geworpen op de wederzijdse interactie van lage cumulusconvectie en de wind. Een belangrijke focus ligt op het effect van windschering op de convectie en op het effect van wervels (convectief en turbulent) op de wind op verschillende hoogtes.

Om de onderzoeksvragen te beantwoorden, zijn numerieke experimenten met large eddy simulaties (LES) uitgevoerd. Vanwege hun fijne resolutie (van enkele honderden meters en kleiner) zijn LES's in staat om wolken en de grootste turbulente wervels expliciet te simuleren. Dit leidt tot een hoge graad van realisme in de simulatie. LES biedt ook de mogelijkheid om het experiment te vereenvoudigen en zodanig stapsgewijs met behulp van vierdimensionale uitvoer natuurkundige mechanismen in de atmosfeer te begrijpen.

Om het effect van windschering op cumulusconvectie te begrijpen, zijn LES experimenten uitgevoerd waarin typische passaatcondities gesimuleerd zijn maar de hoeveelheid van windschering systematisch verandert is. In deze geïdealiseerde LES's beperkt windschering de verticale groei van passaatconvectie. Hiervoor zijn meerdere mechanismes verantwoordelijk die afhangen van de richting van de windschering (toenemende of afnemende windsnelheid met de hoogte) op verschillende hoogtes. Een situatie waarin een oostelijke wind met de hoogte verzwakt en uiteindelijk naar een westelijke wind draait

---

noemt men achterwaartse schering en de tegengestelde situatie waarin een oostelijke wind met de hoogte sterker wordt noemt men voorwaartse schering. Onder invloed van CMT leidt dit tot verschillende windsnelheden aan het oppervlak en daardoor andere vocht en warmte fluxen aan het oppervlak: Een snellere wind aan het oppervlak treedt op bij voorwaartse schering en zorgt voor meer verdamping van oceaanwater en dus diepere convectie. Voorwaartse schering onder de wolken zorgt er ook voor dat wolken sneller bewegen dan hun „wortels" richting het oppervlak een dus voor en ruimtelijke separatie van neerslag en valwinden en nieuw opkomende convectie. Omgekeerd is de forcering aan het oppervlak zwakker onder achterwaartse schering zodat regen het ontstaan van nieuwe convectie bemoeilijkt. Zodra de wolken echter diep genoeg zijn om zo sterk te regenen dat de bijbehorende valwinden zich naast het oppervlak zijwaarts uitbreiden, ont–staat er een groot gebied van koude lucht, een zogenaamde *cold pool*. Aan de randen van divergerende *cold pools* kan convergentie optreden wat tot nieuwe convectie kan leiden. Onder achterwaartse schering wordt dit proces belemmerd en onder voorwaartse schering gestimuleerd. Tenslotte verzwakt windschering in de wolkenlaag onafhankelijk van de richting de verticale wind in de wolk door een sterkere neerwaartse drukgradiënt. Het beperkende effect van windschering op de diepte van convectieve wolken heeft ook invloed op de thermodynamische eigenschappen van de wolkenlaag: De relatieve vochtigheid is hoger en de passaatinversie is sterker.

LES berekeningen op een groot domein van een reeks van dagen tijdens de NAR–VAL meetcampagnes (die in december 2013 en augustus 2016 in de noordatlantische passaatregio plaatsvonden) bieden een ongekend realistisch en compleet zicht op het impulsbudget van de passaatwinden. Advectie (wervels die door het model opgelost wor–den en hier als CMT worden beschouwd) en kleinschalige turbulentie (die niet door het model wordt opgelost) vertragen de wind in de onderste laag van de atmosfeer tot een hoogte van 2 km in de winter en 1 km in de zomer. Afhankelijk van de hoogte hebben CMT en kleinschalige turbulentie een verschillende invloed op de (grootschalige) wind. CMT versnelt de wind aan het oppervlak terwijl kleinschalige turbulentie deze vertraagd. Onder de wolken verandert CMT in een vertragende kracht. De vertraging wordt vanaf de wolkenbasis versterkt door wrijving van kleinschalige turbulentie, en neemt dan met de hoogte snel af. De cumuluswolken zelf zorgen nauwelijks voor vertraging op de hoogte waar de passaatwind het sterkst waait (bij de wolkenbasis), maar lijken zelfs dit maximum in windsnelheid te behouden.

Algeheel blijkt windschering een belangrijke speler te zijn in de typische structuur van de atmosfeer in de passaatregio door de diepte van convectie te beïnvloeden, enerzijds, anderzijds door het (niet) vertragen van de passaatwind. CMT versnelt de wind vlakbij het oppervlak wat de Hadleycirculatie mogelijk minder sterk maakt, terwijl het in de wolkenlaag nauwelijks effect heeft op de wind.

Zusammenfassung

Kumuluswolken („Schönwetterwolken") entstehen durch Konvektion in der Atmosphäre und sind zwischen einigen hundert Metern (humilis) und mehreren Kilometern (congestus) dick. Sie sind eine der Hauptursachen für die Unsicherheit in der Klimasensitivität von Klimamodellen. Um mehr Übereinstimmung zwischen verschiedenen Klimamodellen in den Wolkenveränderungen aufgrund der globalen Erwärmung zu erreichen, ist ein größeres physikalisches Verständnis dieser Wolken erforderlich. Flache Kumuluswolken kommen vor allem über den Ozeanen der Passatregionen vor, die in den Subtropen zwischen 10° und 30° geographischer Breite liegen und sich durch beständige östliche Winde auszeichnen. Diese Oberflächenwinde machen Teil der Hadley-Zelle aus, eines großskaligen Zirkulationssystems, in dem Luft auf großer Höhe vom Äquator wegfließt und nahe der Oberfläche zum Äquator hinfließt. Dies hat zur Folge, dass vertikale Unterschiede in der Windgeschwindigkeit und –richtung (Scherung) in dieser Region allgegenwärtig sind.

Während vergangene Studien gezeigt haben, dass der Wind (an der Oberfläche) stark mit der Bewölkung korreliert, ist noch wenig zum möglichen Einfluss von Windscherung auf Wolken geforscht worden. Anders herum beeinflussen Wolken auch den Wind selbst, indem sie ihn vertikal transportieren. Dieser konvektive Impulstransport (*convective momentum transport*, CMT) spielt eine wichtige Rolle im Kräftegleichgewicht, das die Passatwinde antreibt. Es ist jedoch wenig darüber bekannt, wie dies von der Höhe und der Größe der atmosphärischen Wirbel abhängt. In dieser Arbeit werden beide Richtungen der Interaktion von flacher Kumuluskonvektion und Wind beleuchtet. Besonderer Fokus liegt dabei auf dem Effekt von Windscherung auf die Konvektion und auf den unterschiedlichen Wirbelgrößen (konvektiv und turbulent), mit der die Konvektion den Wind auf verschiedenen Höhen beeinflusst.

Dazu werden Ergebnisse von numerischen Experimenten mit Large-Eddy-Simulationen (LES) herangezogen. Aufgrund ihrer feinen horizontalen Auflösung (von hunderten Metern und weniger) sind LES in der Lage, Wolken und die größten turbulenten Wirbel explizit aufzulösen. Dies führt zu einem hohen Realitätsgrad in der Simulation. Gemeinsam mit der Möglichkeit, den Experimentsaufbau künstlich zu vereinfachen, und der Vollständigkeit der Datenausgabe (räumlich, zeitlich und in Bezug auf physikalische Größen) macht dies LES zum idealen Werkzeug, um physikalische Prozesse in der Atmosphäre zu durchleuchten.

Um die Auswirkungen der Windscherung auf Kumuluskonvektion zu identifizieren und zu verstehen, wurden LES-Experimente durchgeführt, in denen typische Passatbedingungen simuliert wurden, aber die Windscherung systematisch variiert wurde. In diesen idealisierten LES verhindern Scherwinde das Wachstum der Passatkonvektion deutlich. Hierfür sind verschiedene Mechanismen verantwortlich, die abhängen von der Richtung des Schervektors (mit der Höhe zunehmende oder abnehmende Windgeschwindigkeit) sowie der Höhe, auf der die Windscherung auftritt. Eine Situation mit östlichen Winden

an der Oberfläche, die mit der Höhe schwächer werden und schließlich nach West drehen, nennt man Rückwärtsscherung und die entgegengesetzte Situation mit Ostwind, der mit der Höhe zunimmt, nennt man Rückwärtsscherung. Unterschiedliche Scherrichtungen haben aufgrund von CMT unterschiedliche Winde an der Oberfläche zur Folge, was wiederum die Flüsse von Wärme und Feuchte an der Oberfläche beeinflusst: Stärkerer Wind an der Oberfläche tritt unter Vorwärtsscherung auf und führt zu mehr Verdunstung von Meerwasser und somit höher reichender Konvektion. Vorwärtsscherung unterhalb der Wolken führt auch zu einer räumlichen Trennung von Regen-bedingten Abwinden und sich entwickelnden Aufwinden, da sich die Wolken schneller bewegen als ihre unterhalb liegenden „Wurzeln"; dies ist förderlich für die Entwicklung der Konvektion. Umgekehrt ist die Verdunstung an der Oberfläche bei Rückwärtsscherung abgeschwächt und Regen-bedingte Abwinde stören neue Aufwinde, was das Wachstum der Konvektion behindert. Sobald die Wolken allerdings hoch genug gewachsen sind, können sie so starken Niederschlag produzieren, dass sich die damit verbundenen Fallwinde an der Oberfläche seitwärts ausbreiten und ein scharf begrenztes Gebiet mit kalter Luft bilden, einen sogenannten *cold pool*. Die Ausbreitung eines solchen *cold pool* kann an dessen Rändern für Hebung sorgen und damit neue Konvektion auslösen. Rückwärtsscherung kann dies erschweren, während Vorwärtsscherung es begünstigt. Schließlich schwächen Schwerwinde in der Wolkenschicht unabhängig von der Scherrichtung Wolkenaufwinde ab, indem sie die nach unten gerichtete Druckstörungskraft verstärken. Der beschränkende Effekt von Scherwinden auf die Konvektionstiefe hat auch Auswirkungen auf die thermodynamischen Eigenschaften der Wolkenschicht: So ist die relative Luftfeuchtigkeit größer und die Passatinversion ist ausgeprägter, wenn die Konvektion flacher ist.

LES-Berechnungen auf einem großen Gebiet an bestimmten Tagen der NARVAL-Mess-kampagnen (die im Dezember 2013 und August 2016 in der nordatlantischen Passatregion stattfanden) bieten einen einzigartig realistischen und vollständigen Blick auf das Kräftegleichgewicht der Passatwinde. Kombiniert man Advektion (Wirbel, die im Modell aufgelöst sind und als CMT angesehen werden können) und Turbulenz (die nicht aufgelöst ist), so verlangsamen diese zusammen den Wind in der untersten Atmosphärenschicht bis auf eine Höhe von 2 km im Winter und 1 km im Sommer. Die Rolle der beiden Kräfte für sich genommen hängt jedoch von der Höhe ab. CMT alleine beschleunigt den Wind nahe der Oberfläche und nur aufgrund von starker kleinskaliger Turbulenz wirkt auf dieser Höhe netto eine Reibungskraft. Etwa auf halber Höhe zwischen Oberfläche und Wolkenunterkante verändert sich CMT in eine Reibungskraft. Oberhalb der Wolkenunterkante wird diese durch Reibung von kleinskaliger Turbulenz verstärkt, verliert aber mit der Höhe rasch an Intensität. Somit kann festgehalten werden, dass Kumuluswolken selbst keine signifikante Reibung auf der Höhe ausüben, auf der die Passatwinde am stärksten wehen. Tatsächlich helfen sie gemeinsam mit Impulstransport gegen den Windgradient dieses Windgeschwindigkeitsmaximum aufrecht zu erhalten.

Insgesamt scheint Windscherung somit ein wichtiger Faktor zu sein, um die typische Struktur der Atmosphäre in der Passatregion festzusetzen, indem sie die Tiefe der Konvektion reguliert, was selbst einen Einfluss auf die Strahlungsbilanz der Wolken haben könnte. Umgekehrt üben Konvektion und Turbulenz eine Reibungskraft auf die Passatwinde aus. Für sich selbst genommen beschleunigt CMT den Wind nahe der Oberfläche, was die Hadley-Zirkulation abschwächen könnte, während es innerhalb der Wolkenschicht nur geringen Einfluss auf den Wind hat.

1

Introduction

1.1 Cumulus clouds: major source of uncertainty in climate research

Global warming has been widely acknowledged as one of humankind's most urgent and concerning challenges. Great scientific, economical and — at times — political efforts are being undertaken to assess the risks of this threat and mitigate them. The basis for all climate action are model projections of future climate that are made with global climate models (GCMs[1]), which require a thorough understanding of countless physical processes. This thesis wishes to contribute a puzzle piece of research on Earth's climate system, hoping that it will be a contribution to preserving our planet for future generations.

Cloud feedback processes have been identified since 1979 as the greatest source of uncertainty in climate sensitivity (Charney et al., 1979). The climate sensitivity states how much Earth's mean climate would warm up if the CO_2 concentration in its atmosphere is doubled. Traditionally, it has been determined by GCMs, but recently efforts have been made to further constrain it by including other lines of evidence, like records from Earth's palaeoclimatological and recent history (Stevens et al., 2016; Sherwood et al., 2020). Only through this, some limited progress has been made in reducing the uncertainty in climate sensitivity, which is currently estimated to lie between 2.3 and 4.5 K (Sherwood et al., 2020). Bony et al. (2013) argue that a better understanding of the physics of cloud processes is one of the steps needed to improve future climate change assessments.

The underlying reason for the substantial spread in climate–sensitivity estimates can be found in the feedback mechanism caused by subtropical marine clouds — or rather our limited understanding of it (e.g. Bony & Dufresne, 2005; Vial et al., 2013; Zelinka et al., 2013; Caldwell et al., 2016). In particular, the question is to what extent a warmer climate will lead to fewer shallow clouds due to the warmer temperatures (as water condensates less quickly in warm air to form clouds). Fewer clouds, in turn, would reflect less sunlight

---

[1]The acronym GCM traditionally stands for general circulation model, which in many cases is an interchange-able term for global climate model.

A beginner's guide to cumulus convection

The Latin word *cumulus* means heap or pile, referring to the fact that cumulus clouds consist of liquid water that 'piles up' in the air, giving them a puffy or cauliflower-like appearance (see Fig. 1.1d). These clouds are however only the visible part of the physical process of convection in the atmosphere.

Let us consider a parcel of air that is situated near the surface and that has a certain temperature and contains a certain amount of water vapour. If the parcel's temperature is somewhat larger than that of its environment, it will start to rise through the atmospheric column, due to its lower density. The force that drives this ascent is called buoyancy and is proportional to the density difference between the parcel and the environment. During this adiabatic ascent, our parcel will be subjected to decreasing pressure and colder environmental temperature, allowing for continuous ascent. Note that due to the decreasing environmental pressure, our parcel expands and the temperature of the air parcel itself decreases, and if it becomes colder than the environment, its ascent may cease at a certain height before a cloud forms. But let us assume that this does not happen and that our parcel continues to rise. Due to the temperature decrease, the parcel's ability to hold water vapour gradually decreases, while the amount of water vapour it contains does not change. In other words, its relative humidity increases. At some height, the relative humidity will reach 100 per cent (saturation), and the water vapour contained in our parcel will start to condense, forming visible water droplets: a cloud. During the condensation, energy is released in the form of (latent) heat. This additional heating further drives the ascent of the parcel and the growth of the cloud.

Because air parcels start their journey near the surface under very similar conditions (in terms of temperature and humidity), they also reach saturation at the same height (called the lifting condensation level, LCL). As a consequence, cumulus clouds usually have a very well-defined base that, moreover, hardly varies among neighbouring clouds (Fig. 1.1a, b). The cloud-top height, on the other hand, can be much more variable (Fig. 1.1c), and it depends on a number of conditions. First, there are the properties of our rising air parcel itself: Once all its water vapour has condensed, no more latent heat release boosts the parcel's ascend. Second, the environmental conditions play a major role: For example, it is common — especially in the trades — that the temperature drastically increases within an often thin atmospheric layer, an inversion. The parcel's buoyancy may not suffice to overcome this inversion, capping cloud growth at this height. Finally, atmospheric turbulence leads to a continual mixing of the cloud's air with the environment (entrainment). This may result in a decrease of the cloud's water content (because the environmental air at great heights is rather dry) and hence in less latent heat available for the cloud to grow.

As already mentioned, it is important to point out that clouds are merely the visible part of the convection, and there is more to it than the clouds themselves. Below cloud base, where we speak of dry convection or thermals, updrafts and turbulence are already present (Fig. 1.2). But even above the LCL, parts of the convection remain invisible to the human eye: Generally, what goes up has to come down (mass continuity), meaning that downdrafts are part of the convective system as well. However, even though they originate from the visible clouds, downdrafts are usually not visible because as the air descends again, the temperature increases, and liquid water droplets evaporate.
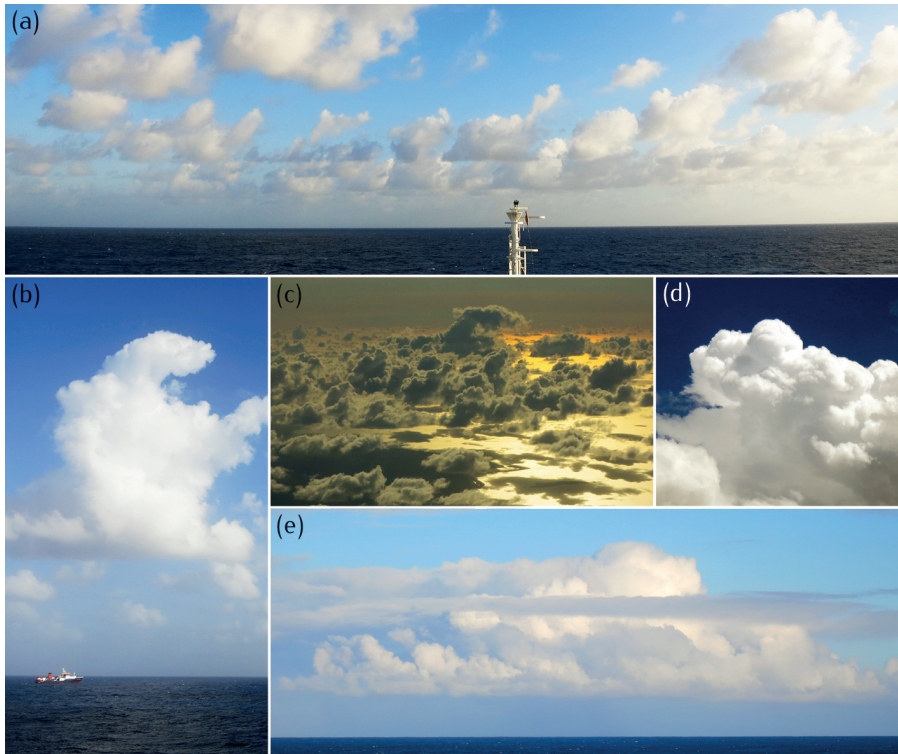
Figure 1.1: Photographs of exemplary cumulus clouds: (a, b, e) over the Atlantic Ocean near Barbados, (c) over Zeeland, the Netherlands, and (d) over the French Alps.

back to space and thus further amplify global warming: a positive feedback.[2] The fraction of the sky that is covered by clouds determines how much solar radiation they reflect back to space, and this is mostly set by the cloud amount at cloud base. Two processes that are believed to be most closely connected to uncertainties in cloud feedbacks as predicted by GCMs are convective mixing and its control of the cloud–base cloud amount (e.g. Vial et al., 2017, and references therein). It is thus crucial to unravel the physical processes that control cloudiness near cloud base (e.g. Vial et al., 2017; Bony et al., 2017). Moreover, clouds are strongly intertwined with large–scale circulation cells through their regulation of radiative cooling (e.g. Riehl et al., 1951; Fermepin & Bony, 2014).

Some of the advances discussed above are motivated by a 'grand challenge' on clouds, circulation and climate sensitivity that was formulated by the World Climate Research Programme (WCRP; Bony et al., 2015). It proposes to focus atmospheric research on four main questions:

1. What role does convection play in cloud feedbacks?

---

[2]Note that only recently, more and more climate models have come to agree that the cloud feedback is indeed positive (e.g Zelinka et al., 2020). If the cloud feedback was negative, more (sea) water evaporation in a warmer climate would increase the atmosphere's relative humidity and thus the amount of clouds, which could reflect more sunlight back to space, counteracting global warming.

1

Figure 1.2: Schematic of two different mechanisms in the subcloud layer: (a) roll structures causing convergence ('1' in the figure) and lifting of air parcels to the LCL ('2') or (b) root-like bouyan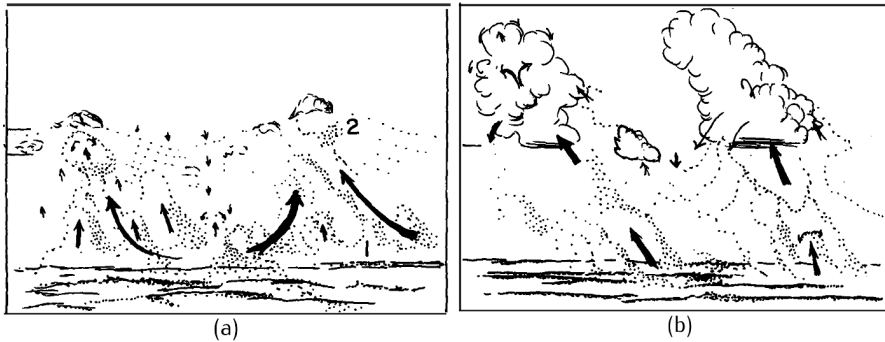t updrafts clearly connected to the clouds above. (Figure courtesy: LeMone & Pennell, 1976, ©American Meteorological Society)

2. What controls the position, strength and variability of storm tracks?

3. What controls the position, strength and variability of tropical rain belts?

4. What role does convective aggregation play in climate?

Despite the broad scope of these questions, this thesis contributes to answering them: The investigation of the interplay between convection (including its organisation) and wind in the trades is a contribution to Questions 1 and 4, but the findings may indirectly also aid in answering Question 2 and 3, as will be discussed below.

1.2   Clouds in the trades and their organisation

The WCRP grand challenge has sparked a wealth of new research in recent years, culminating in the EUREC^{4}A field campaign, which with great expenditure aimed to elucidate the link between cloudiness and large-scale atmospheric circulation in the North Atlantic trades (Stevens et al., 2021). However, despite significant progress in our understanding of trade-wind cumuli, their coupling to the circulation and their influence on the climate system, many topics have hardly been investigated or not been discussed so far (Nuijens & Siebesma, 2019). For example, although it has been known for a long time that shallow clouds organise in patterns (e.g. Malkus, 1963), it has been identified as a topic that needs further investigation (Vial et al., 2017; Nuijens & Siebesma, 2019). Consequently, a new classification system has emerged recently, which divides mesoscale cloud patterns into the four classes of sugar, gravel, fish and flowers (Stevens et al., 2020b). First fruitful attempts have been made to understand the physical mechanisms behind these patterns, but how they will change in a warmer climate and what their impact is on cloud feedbacks remains to be explored (Bony et al., 2020; Schulz et al., 2021).

This new line of research revealed that the most common type of clouds in the trades is so-called gravel, somewhat deeper, precipitating cumulus clouds, which may, at times, be accompanied by a secondary stratiform layer (flower) near the inversion (Schulz et al., 2021, an example is shown in Fig. 1.1e). This finding is at odds with the traditional idea of

trade–wind clouds being very thin, unorganised, non–precipitating cumulus humilis (sugar, see for example Fig. 1.1a). This idea had been established in particular through the Barbados Oceanographic and Meteorological Experiment (BOMEX; Holland & Rasmusson, 1973). Throughout the years, this concept got challenged more and more: The Rain in Cumulus over the Ocean campaign (RICO; Rauber et al., 2007) established that trade–wind cumuli commonly produce rain, and based on observations from a remote–sensing site on Barbados, Nuijens et al. (2014) argued that deeper clouds with stratiform layers near the inversion occur more regularly than modelling studies suggest. Therefore, in this thesis (in particular, Chapters 2 and 3), the focus is on the somewhat deeper cloud species of cumulus congestus, which has received only very little attention in the literature (Nuijens & Siebesma, 2019).

The aforementioned novel way of classifying mesoscale patterns of shallow clouds as sugar, gravel, fish and flowers is purely based on their visual appearance in satellite imagery, and as such, it overlaps with classical concepts of cloud organisation that are based on physical mechanisms. For example, clouds can organise in squall lines (Rotunno et al., 1988; Weisman & Rotunno, 2004), rain bands (Hildebrand, 1998), arcs (Zipser, 1969; Warner et al., 1979) and supercells (Rotunno & Klemp, 1982), and in all of these, wind shear (vertical changes in wind speed and direction) plays an important role, as will be discussed below.

Of particular interest in this thesis are mesoscale arcs, which are a result of cold pools. Cold pools are large cloud–free areas (with diameters of several tens of kilometres) that are encircled by clouds. Even early observational studies associated such large cloud–free areas with strong precipitative downdrafts that spread out as gravity currents near the surface, triggering new convection in arc–shaped patterns at their edges (Zipser, 1969; Black, 1978; Warner et al., 1979). The downdrafts are mostly driven by evaporation of precipitation, which enhances the negative buoyancy (e.g. Khairoutdinov & Randall, 2006). Zuidema et al. (2012) analysed similar arc structures in a shallow cumulus regime during the RICO campaign and found that they were caused by similar mechanisms as in deep convection. Shallow cumulus cold pools are a topic of ongoing research (e.g. Zuidema et al., 2012, 2017; Seifert & Heus, 2013), and of particular interest is how new convection is triggered at cold–pool edges (Torri et al., 2015): either through a thermodynamic (Tompkins, 2001) or through a mechanical mechanism (Li et al., 2014). In the latter, negative vorticity from near–surface wind shear and positive vorticity within the cold pool together facilitate mechanical lifting at the cold–pool edge, leading to the development of cloud arcs.

1.3   Trade winds and how they interact with clouds

The trade–wind regions are not only Earth's regions where shallow cumuli are most prominently found (Warren et al., 1988) but are also characterised by their steady surface winds (e.g. Brümmer et al., 1974). These trade winds form the inflow branch of the Hadley circulation cell (Fig. 1.3a): Upon converging near the equator, the air ascends and forms deep cumulonimbus towers. At high altitudes, the air spreads out poleward and descends again at higher latitudes to flow back towards the equator near the surface. As indicated in Fig. 1.3b, the surface winds are driven by a meridional pressure gradient directed towards the low surface pressure near the equator. Due to Earth's rotation, the Coriolis accel-
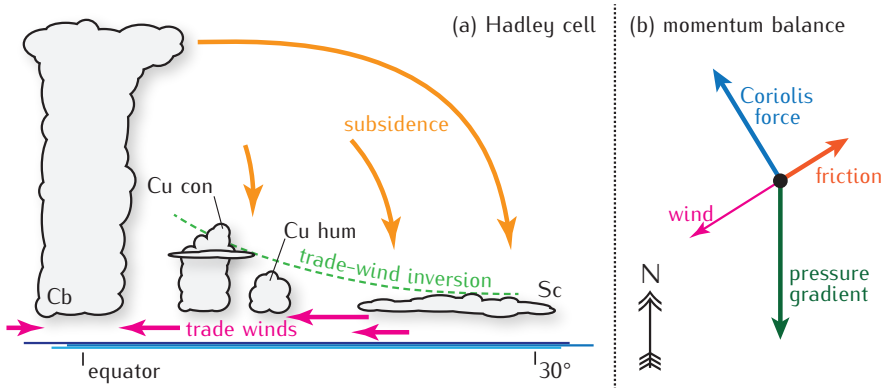
1

Figure 1.3: (a) Schematic of the Hadley circulation with its characterising cloud types: cumulonimbus (Cb), stratocumulus (Sc), cumulus humilis (Cu hum) and cumulus congestus (Cu con). (b) Idealised force balance of the (surface) trade–winds (in the northern hemisphere).

eration deflects the winds to the right, together with frictious forces leading to steady east–north–easterly winds (in the northern hemisphere). The meridional (north–south) component of this circulation is the Hadley cell (illustrated in Fig. 1.3a), and the zonal (east–west) component is called Walker cell.

As reflected in the title, a particular interest of this thesis are some of the various ways through which cumulus convection and the wind interact with each other. The most obvious of such an interaction is simply the fact that clouds 'drift' with the wind — a phenomenon everybody knows from the satellite videos we see every evening on television. But next to such direct effects on clouds, the trade winds also modulate ocean currents and upwelling, turbulent fluxes at the sea surface and its temperature, which are all crucial for atmospheric processes, including clouds and convection as well as their organisation.

A rather subtle wind–cloud interaction works via the surface fluxes of heat and moisture. A cloud parcel receives its basic ingredients already at the surface in the form of a certain amount of heat and moisture that it can take along on its journey. How much heat and moisture depends on three factors: (1) how warm and moist the underlying surface is compared to the overlying air, (2) the stability of the near–surface atmosphere and (3) how strong the wind blows near the surface. Hence, one could imagine that stronger surface winds also cause larger clouds. However, due to a feedback process, the picture is more complicated (Nuijens & Stevens, 2012): First, stronger wind will strengthen the surface heat and humidity fluxes and indeed cause deeper clouds. As a consequence, downdrafts originating at cloud tops will also transport air from higher altitudes to the surface, which is usually relatively dry and warm (in terms of potential temperature). When this warm and dry air reaches the surface, it will increase the surface humidity flux, but diminish the surface heat flux, meaning that the convection has more latent heat (moisture) but not more sensible heat at its disposal, ultimately resulting in deeper but not more 'energetic' clouds. The fact that these findings by Nuijens & Stevens (2012) are based on simulations of non–precipitating convection motivates studying the influence of wind speed again in a more realistic setting. Other studies have suggested that surface wind speed correlates

very well with shallow cloudiness (Brueck et al., 2015; Nuijens et al., 2015) and mesoscale cloud patterns (Bony et al., 2020; Schulz et al., 2021) and, furthermore, that it possibly affects convective self-aggregation (Wing et al., 2017). However, despite being a common feature of the trades, wind shear is not a factor that is regularly investigated and often merely a side note in cloud studies.

Wind shear is the underlying reason for some particularly illustrative effects of the wind on clouds: the slope that some clouds have (see Fig. 1.1a, c) or when clouds seemingly move against the wind that is felt at the ground (Malkus, 1949, 1952). For example, in the case of the clouds in Fig. 1.1a, the wind is strongly blowing from right to left near cloud base, but less strongly at greater heights, resulting in a visible tilt of the clouds towards the right. A consequence of this tilting is that a larger projected area of the sky is covered by cloud (Neggers et al., 2003; Yamaguchi et al., 2019). This results in less short-wave radiation in the form of sunlight reaching the surface and more of it being reflected back into space — a direct effect on Earth's heat budget.

Especially in studies of deep convection, wind shear has been shown to play an important role both in limiting the depth of convective towers as well as strengthening convection through spatial organisation. Already since the 1960s, the fact that clouds under the influence of shear often appear in elongated rolls or streets has been discussed (e.g. Malkus, 1963; Asai, 1964; Hill, 1968). Later it was shown that shear is crucial in explaining the formation of rain bands and squall lines, which are usually oriented perpendicular to the shear vector (e.g. Rotunno et al., 1988; Parker, 1996; Hildebrand, 1998; Robe & Emanuel, 2001; Weisman & Rotunno, 2004). Such organisation can significantly strengthen the circulation and influence the vertical extent of convection. For example, Park et al. (2018) demonstrated that the transition from shallow convective cells to rolls can be linked to the different vertical development of clouds. They attribute this link to a strong connection of clouds to subcloud-layer coherent structures. Indeed, in a much earlier airborne observational study, LeMone & Pennell (1976) already discussed such roll structures in the subcloud layer as one possible mechanism to supply moisture to shallow cumulus clouds (the other one being root-like plumes; both depicted in Fig. 1.2). However, shear can also limit convection. Especially in the early stages of the convective development, shear enhances the thermodynamic and dynamic perturbation pressure forces, which oppose the buoyancy force and thus weaken updrafts (Pastushkov, 1975; Peters et al., 2019). Another mechanism by which shear inhibits deep convection is by 'blowing off' cloud tops, i.e. entraining dry and less buoyant air (e.g. Sathiyamoorthy et al., 2004; Koren et al., 2010).

The interplay of wind and convection is not a one-way street on which only the wind influences the clouds. The other direction in which clouds affect the wind is just as interesting. Convection helps setting both local winds and large-scale wind systems through, among others, convective momentum transport (CMT; e.g. Brümmer et al., 1974; Carr & Bretherton, 2001; Stevens et al., 2002; Richter & Rasch, 2008; Lin et al., 2008; Back & Bretherton, 2009). Furthermore, studies suggest that CMT matters for the representation of large-scale circulations (Zhang & McFarlane, 1995) and the El Niño-Southern Oscillation in global models (Kim et al., 2008) as well as the forecast of tropical cyclones (Hogan & Pauley, 2007). Within the aforementioned cold pools, CMT may be responsible for an asymmetric structure, as faster momentum from greater heights is transported to the surface by the strong precipitative downdraft (Mahoney et al., 2009; Grant et al., 2020).

1

> ### Convective momentum transport in layperson's terms
>
> An important phenomenon discussed in this thesis is that of convective momentum transport (CMT). Noting that momentum is the product of mass and velocity, one can say that in this context momentum is essentially a different word for wind. This way, the concept of CMT becomes somewhat clearer right away.
>
> Let us remember the parcel of air from the beginner's guide to cumulus convection a few pages earlier. We established there that it contains a certain amount of heat and water vapour, which it transports around. In just the same way, the air parcel also carries a certain amount of momentum. For example, on its way up, the parcel carries with it momentum from near the surface. Anybody who has ever stood on top of a high building knows that the wind near the surface blows much slower than higher up, owing to the fact that vegetation, buildings and even the ground itself slow down the wind through friction. The result of our air parcel transporting this slow wind speed upward is that within clouds, the wind speed is usually much lower than in their vicinity.
>
> Similarly, descending air parcels transport momentum too. That should be obvious to anybody who has ever been outside when a thunderstorm was approaching. In this situation, one often feels a distinct front of strong, gusty wind arriving even before the rain starts. The reason behind this is that the strong rain and hail in the thunderstorm 'pulls' a lot of air with it on its way down from heights of several kilometres. As winds at greater heights are faster than near the surface, a front of strong (and cold) wind is felt at the surface.
>
> To what extent CMT affects the wind speed and direction as a whole both at the heights where clouds live and near the surface, is one of the questions that this thesis is concerned with.

While CMT by deep convection has been extensively studied (e.g Schneider & Lindzen, 1976; Wu & Yanai, 1994; Moncrieff, 1997; Badlan et al., 2017), shallow CMT has long been overlooked, and its research has only gained proverbial momentum in recent years (Zhu, 2015; Schlemmer et al., 2017; Larson et al., 2019; Saggiorato et al., 2020; Dixit et al., 2021). A recurring theme of these papers is the poor representation of the momentum flux through conventional mass-flux schemes, which are widely used in GCMs. The problem is that these schemes have been developed with scalar quantities in mind, like heat and moisture, but momentum transport works differently for a number of reasons. Not only is the momentum distribution in the cloud layer more complex than assumed in the top-hat approach that is underlying all mass-flux schemes. Momentum is also carried to much greater extent by small eddies than by coherent plumes, and the vertical and horizontal velocities are often out of phase with each other (Zhu, 2015). Furthermore, unlike scalar quantities, momentum is not a conserved variable but is subjected to more sinks and sources such as pressure-gradient forces, which are difficult to parametrise in a conventional mass-flux framework (Schlemmer et al., 2017).

Resolving the long-standing problem of a poor representation of (shallow) CMT in large-scale models requires a thorough understanding of the physical process itself. A better understanding of CMT will improve operational wind forecasts, and as such, it is of

immediate interest to the growing wind-energy sector (e.g. Petersen & Troen, 2012) and the weather-forecasting community (Sandu et al., 2020).

1.4 Objectives

The aim of this thesis is to find the physical mechanisms that explain the interaction of shallow cumulus convection and the wind profile and to assess to what extent they matter for the trades at large. As has become apparent in the previous sections, two directions can be considered here: the influence of the wind on the convection and the other way around. This prompts me to formulate the following research questions:

1. **How does wind shear influence trade-wind cumulus convection, in particular its depth, amount, precipitation, macrophysical structure and organisation as well as the trade-wind boundary layer as a whole?**

2. **To what extent does shallow cumulus convection determine the vertical structure of the trade winds through momentum transport, and in particular, what is the relative importance of small-scale turbulence and larger-scale coherent updrafts at different heights?**

In particular, the insights on convective depth from the first question are of great relevance for cloud-radiative effects. Furthermore, aggregation of convection will play a central role in the answer. As such, this line of research is a direct contribution to Questions 1 and 4 of the WCRP grand challenge (see p. 3), which ask about the role of convection and its convective aggregation in climate. Insight about CMT and the momentum budget from the second of the above research questions are a more indirect contribution to WCRP Questions 2 and 3, which ask about the position, strength and variability of both extratropical storm tracks and tropical rain belts. In particular, the role of CMT for the Hadley circulation, which is responsible for convergence near the equator, comes to mind.

1.5 Methodology: large-eddy simulation

Large-eddy simulations (LES) are utilised to find answers to the above research questions. After first pioneering work in the 1960s by Lilly (1962), Smagorinsky (1963) and Deardorff (1970), LES soon became a common tool in the atmospheric sciences (e.g. Sommeria, 1976; Nieuwstadt & Brost, 1986) and remains an essential method until present day, among others for studying shallow cumulus convection (e.g. Siebesma et al., 2003; Van Zanten et al., 2011). As opposed to the earlier mentioned GCMs, an LES only simulates a small volume of the atmosphere, typically a few tens of kilometres wide and a few kilometres high. Such an approach allows for a different use of the available computational power: While a GCM is restricted to a rather coarse spatial resolution of many kilometres in the horizontal, the smaller LES domain allows for a finer resolution down to a few tens of metres. This in turn allows the model to explicitly resolve many physical processes and hence to use parametrisations only for a very few processes, as outlined below.

Specifically, an LES numerically solves the system equations of mass, momentum, heat and other scalars after they have been filtered with a spatial filter of a certain length. The idea here is that a large fraction of the turbulence energy is contained in

1

scales larger than that LES filter and thus explicitly resolved by the model. Typically, LES studies of atmospheric convection use grid lengths of around 100 m, which is smaller than, for example, the largest eddies of convective updrafts. Processes that remain to be parametrised are the cloud microphysics, subgrid turbulence, radiation and surface fluxes. Overall, LES is thus considered 'our most realistic modelling tool for cloud-topped boundary layers' (Bretherton, 2015) and is ideally suited to unravel the physical mechanisms at play in the atmosphere. Intercomparison studies of LES models (like Siebesma et al., 2003; Van Zanten et al., 2011) have shown that today's models are able to robustly simulate many cloud processes and to provide reliable statistics of shallow cumulus convection in particular, which is of interest in this project.

The specific model that is mainly used in this thesis is DALES, the Dutch Atmospheric Large-Eddy Simulation (Heus et al., 2010). The roots of DALES date back to the 1980s, and it has since then been steadily developed further and used for a wide range of studies by atmospheric scientists all over the Netherlands and beyond. Additionally, this thesis utilises simulations that were run by scientists at Max Planck Institute for Meteorology (MPI-Met) in Hamburg using the Icosahedral Nonhydrostatic Large-Eddy Model (ICON-LEM; Dipankar et al., 2015). ICON is a modelling suite, jointly developed by the German Weather Service (DWD) and MPI-Met.

Despite their high degree of realism, LES studies may still suffer from model biases and uncertainties that are common to all modelling approaches. The only way to completely avoid this is by making use of field observations. However, with this more authentic view also come great complications, as physical processes are always affected by a multitude of factors that cannot be controlled (or at least be recorded) in a natural environment. For example, if a measurement shows that clouds are shallower on one day than on the previous one, which of the many factors that change from day to day is responsible for that? The use of a model offers great relief here, as it allows to adjust only a single factor at a time in a given experiment and even to artificially suppress certain physical processes. Furthermore, observations come with their own limitations, the most striking one in comparison to LES being the limited spatial or temporal availability of measurements of certain quantities. For example, measurements of the wind profile are often only available through radiosondes, which are launched at sparse times and locations, while an LES can provide output of the wind vector in a dense four-dimensional space. Besides, meteorological quantities are often only indirectly derived from the observation of other quantities, for example when one translates a weather radar signal into a precipitation rate.

In recent years great steps have been taken towards ever more realistic LES experiments. In particular, the domains that have been used have grown substantially. While many idealised studies in the past and present use LES domains of a few tens of kilometres width, more realistic settings have been explored on domains of several hundreds of kilometres width, for example covering the Netherlands (Schalkwijk et al., 2015), Germany (Heinze et al., 2017) or even large portions of the tropical and subtropical North Atlantic (Stevens et al., 2019). This approach has several advantages: Not only does the large domain allow to study larger-scale phenomena, like convective organisation, the set-up usually utilises open side boundaries where a realistic forcing from a numerical weather-prediction model can be applied, for instance. As opposed to the more traditional periodic boundary conditions, which may unphysically constrain the horizontal circulations (Bad-

lan et al., 2017; Dixit et al., 2021), this allows for a realistic depiction of both the large- and the small-scale conditions on specific days. While conventional large-scale models (e.g. GCMs) of course also have the advantages of a large domain, they use a much coarser resolution and rely on parametrisations for many physical processes, leading to a less accurate representation of clouds and precipitation (Stevens et al., 2020a). It should be noted though, that the merits of large-domain LESs come at a price, namely that of computational cost: Although LESs often produce superior results compared to modern numerical weather-prediction models, they are currently still computationally too expensive to be used as operational weather-forecast models on large domains (Schalkwijk et al., 2015; Heinze et al., 2017).

In this project, both LES approaches — idealised experiments on a small domain and realistic depictions of particular days on a large domain — are utilised. To answer the first research question posed above, it is desirable to have a great deal of control over the parameters at play and to have the ability to alter only a single factor in the experimental set-up at a time or to 'turn off' certain physical processes. This can best be achieved in an idealised LES experiment. On the other hand, the second research question calls for a close look at realistic conditions. Therefore, we make use of a realistic LES set-up that covers a large portion of the tropical and subtropical North Atlantic.

1.6   Outline

The content of this thesis is based on three journal articles, which form Chapters 2–4. Each of theses chapters is self-contained and has a separate introduction. Certain overlaps may thus be present.

Chapters 2 and 3 deal with different aspects of how wind shear affects trade-wind cumulus convection (first research question). Chapter 2 discusses the response of trade-wind convection to different amounts and types of wind shear. Inspired by the results of this study, Chapter 3 takes a more qualitative view, specifically shedding light on the morphology of sheared clouds as well as the structure of cold pools. The other side of the coin is considered in Chapter 4, which deals with the effect of cumulus convection on the wind, by analysing the momentum budget in the trades (second research question). An overarching summary with conclusions and recommendations is given in Chapter 5.

2

How wind shear affects
trade–wind cumulus convection

Motivated by an observed relationship between marine low cloud cover and surface wind speed, this study investigates how vertical wind shear affects trade-wind cumulus convection, including shallow cumulus and congestus with tops below the freezing level. We ran large-eddy simulations for an idealised case of trade-wind convection using different vertical shears in the zonal wind. Backward shear, whereby surface easterlies become upper westerlies, is effective at limiting vertical cloud development, which leads to a moister, shallower and cloudier trade-wind layer. Without shear or with forward shear, shallow convection tends to deepen more, but clouds tops are still limited under forward shear. A number of mechanisms explain the observed behaviour: First, shear leads to different surface wind speeds and, in turn, surface heat and moisture fluxes due to momentum transport, whereby the weakest surface wind speeds develop under backward shear. Second, a forward shear profile in the subcloud layer enhances moisture aggregation and leads to larger cloud clusters, but only on large domains that generally support cloud organization. Third, any absolute amount of shear across the cloud layer limits updraft speeds by enhancing the downward-oriented pressure perturbation force. Backward shear — the most typical shear found in the winter trades — can thus be argued a key ingredient at setting the typical structure of the trade-wind layer.

2.1   Introduction

In light of the uncertain role of trade–wind cumulus clouds in setting the cloud feedback in climate change, there is widespread interest in understanding the behaviour of these clouds, the different ways they interact with their environment and how this changes in response to global warming (e.g. Bony & Dufresne, 2005; Bony et al., 2013; Vial et al., 2017). Trade–wind cumuli are found in regions characterised by the trade winds, yet we understand relatively little about how they depend on the structure of the trade wind, compared to how they depend on temperature and moisture. Some studies have investigated the influence of the wind speed on low clouds in the trades and revealed that surface wind speed is one of the better predictors of low cloud amount (e.g. Nuijens & Stevens, 2012; Brueck et al., 2015; Klein et al., 2017). But it is unclear how much the wind shear plays a role in observed cloud amount–wind speed relationships, as one might expect both wind speed and wind shear to increase with larger meridional temperature gradients throughout the lower troposphere when assuming geostrophic and thermal wind balance. Furthermore, little work has concentrated on the influence of wind shear on convection, other than its role in increasing the amount of projected cloud cover.

From studies of deep convection we know that wind shear can have a number of effects. Shear is effective at organizing deep convective systems into rain bands and squall lines (e.g. Thorpe et al., 1982; Rotunno et al., 1988; Parker, 1996; Hildebrand, 1998; Robe & Emanuel, 2001; Weisman & Rotunno, 2004). At the same time, shear can limit convection during its developing stages (Pastushkov, 1975). A recent paper by Peters et al. (2019) clearly shows how shear reduces updraft speeds in slanted thermals by enhancing the (downward-oriented) pressure perturbations. Shear is also argued to inhibit deep convection by 'blowing off' cloud tops (e.g. Sathiyamoorthy et al., 2004; Koren et al., 2010), which we interpret as an increase in the cloud surface area that experiences entrainment, which also plays a role in setting updraft buoyancy and updraft speeds.

Malkus (1949) might have been one of the first to mention the effect of shear on shallow convection, noting that the tilting of clouds through shear causes an asymmetry in its turbulence structure with more turbulence on the windward than the leeward side. Through numerous studies we now know that shear helps organize shallow convective clouds in rolls or streets along with the development of coherent moisture and temperature structures in the subcloud layer (e.g. Malkus, 1963; Asai, 1964; Hill, 1968; LeMone & Pennell, 1976; Park et al., 2018). Li et al. (2014) explain how shear over the subcloud layer interacts with the low–level circulation induced by cold pools to enhance or limit the regeneration of convective cells and longevity of shallow cloud systems. In a recent LES study of shallow convection over the Sulu Sea in the Philippines, Yamaguchi et al. (2019) find that wind shear leads to a stronger clustering of clouds and slightly increased cloud–base cloud fractions as well as diminished cloud depths. Brown (1999) shows that shear can strongly affect the surface wind via momentum transport, but that it has little effect on the turbulence kinetic energy (TKE) budget, on scalar fluxes and on cloud properties. This is in contrast to the dry convective boundary layer, where shear has a strong impact on the TKE budget (Fedorovich & Conzemius, 2008, and references therein).

The present study investigates how vertical wind shear influences trade–wind cumulus convection, including shallow cumulus and cumulus congestus below the freezing level. For instance, we ask, how shear impacts cloud tops, cloud amount and the structure of

the boundary layer. To this end, we used an idealised large–eddy–simulation (LES) case — inspired by Bellon & Stevens (2012) and Vogel et al. (2016) and not unlike the typical atmosphere in the trades — aiming at a fundamental understanding of the sensitivity to forward and backward shear (by which we mean an increase and decrease, respectively, of the zonal wind velocity with height) of different strengths.

The remainder of this paper is structured as follows. We first explain our idealised LES set–up and the wind shear variations we impose. The results are then presented in a twofold manner. First, we discuss the effects of shear on the cloud and boundary–layer evolution, showing results from large– and small–domain simulations with interactive and prescribed surface fluxes. Second, focusing on the large–domain runs with constant surface fluxes, we discuss how shear impacts the cloud structure and cloud depth without surface flux responses. We end with a concluding discussion and an outlook on future work. In an appendix, we discuss the influence of shear on the clouds' vertical–velocity budget.

2.2   Experimental design

We carried out large–eddy simulations (LES) using version 4.2 of the Dutch Atmospheric Large Eddy Simulation (DALES; Heus et al., 2010). In our experimental set–up, we prescribed large-scale forcings and initial profiles typical of the North Atlantic trades at a latitude of $\varphi = 15°$ N (Sections 2.2.1–2.2.3). We used a domain of 50.4×50.4 km^2, with a resolution of 100 m in the horizontal directions and doubly periodic boundary conditions. The domain top is at about 18 km and the vertical grid is non-uniform: starting with 10 m at the surface and increasing by a factor of 0.01 at each level to about 190 m at the domain top. In order to evaluate the effect of different surface winds and surface heat fluxes that develop under shear, we performed simulations with interactive and prescribed sensible and latent surface fluxes (Section 2.2.4). We also conducted simulations on a smaller domain (12.6×12.6 km^2) where the development of cold pools and deeper clouds is less pronounced (Vogel et al., 2016).

2.2.1   Thermodynamics

The standard case set–up is inspired by that of Vogel et al. (2016) and Bellon & Stevens (2012), who introduced an idealised modeling framework with only a limited set of parameters that represent the large–scale flow. The initial temperature and humidity profiles of our simulations (Fig. 2.1) have a well–mixed layer of 1 km depth over a surface with a constant sea–surface temperature (SST) of 300 K. The mixed layer is topped by a 600–m–deep inversion layer. In the free troposphere, the profile of liquid water potential temperature θ_l follows a constant lapse rate of 4 K/km, and the relative humidity is constant with height at 50 per cent. We applied a constant radiative cooling rate of -2.5 K/d to θ_l (i.e. no diurnal cycle), which promotes relatively strong shallow convection, allowing for the development of the congestus clouds we are interested in. Compared to Vogel et al. (2016), we increased the domain top to 18 km to allow for deeper convection. Between 10 and 18 km, the radiative cooling is quadratically reduced to zero. The relative humidity reaches zero at about 14 km, which is also the lower boundary of the sponge layer in our LES. The θ_l lapse rate above 10 km is 8 K/km reflecting a stable upper atmosphere. In
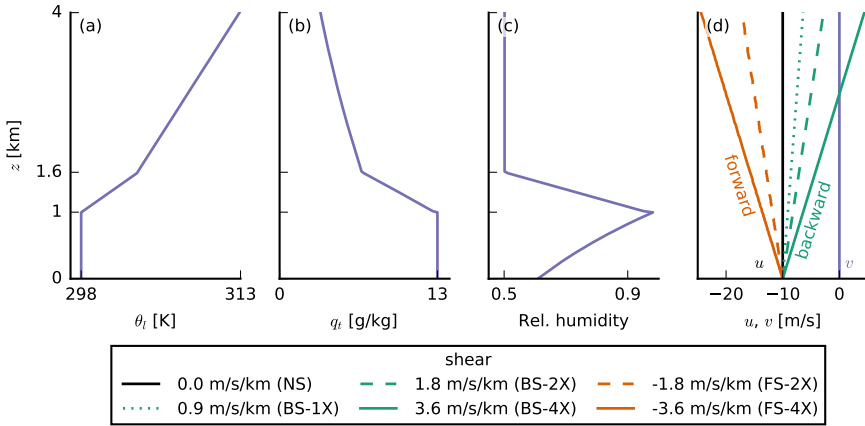
Figure 2.1: Initial profiles of (a) the liquid water potential temperature θ_l, (b) total water specific humidity q_t, (c) relative humidity and (d) the two wind components u and v. Purple profiles are the same in all simulations. Orange stands for forward shear (FS) and green for backward shear (BS). Same line types indicate the same amounts of absolute shear (1X, 2X, 4X). The colour coding of the different shears is the same for all other figures.

all simulations, we used a single–moment ice microphysics scheme (Grabowski, 1998) and allowed for precipitation assuming a constant cloud droplet concentration of 60 cm^{-3}.

2.2.2   Large–scale subsidence

Different than Vogel et al. (2016), we used a weak–temperature–gradient (WTG) assump–tion to calculate the subsidence profile, as the deeper congestus clouds that develop increasingly violate the assumption of a strongly subsiding atmosphere. Practically, the WTG method was implemented following Daleu et al. (2012): Above a reference height, we calculated the subsidence rate w_s such that it maintains the virtual potential temperature θ_v close to its initial (reference) profile $\theta_{v,0}$ according to

$$w_s = \frac{1}{\tau} \frac{\overline{\theta_v} - \theta_{v,0}}{\partial_z \theta_{v,0}}, \qquad (2.1)$$

where the overbar indicates slab averaging, ∂_z symbolizes the vertical derivative and τ is the relaxation time scale, which can be thought of as the time scale over which density anomalies are redistributed by gravity waves and thus how fast the circulation acts to counteract the heating induced by convection. We set $\tau = 1$ h, a rather short time scale that avoids the build–up of large density anomalies and unphysically high subsidence rates during episodes of deeper convection. WTG is not valid at levels where turbulence and convection effectively diffuse gravity waves. Therefore, we only apply WTG above 3 km, and below that (aligned with the bulk of the cloud layer above which cloud fraction becomes small), we linearly extrapolate w_s to zero. We also apply a nudging with a time scale of 6 h towards the initial q_t (total water specific humidity) profile in the free troposphere (above 4 km) to avoid spurious moisture tendencies.
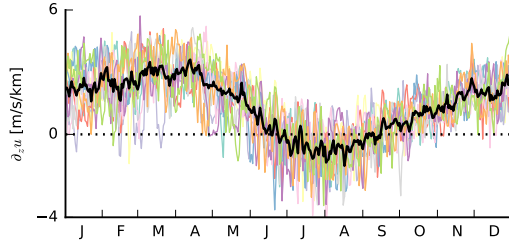
Figure 2.2: Time series of the amount of zonal shear between 1 and 3 km for the years 2008 to 2017 averaged over the area from 9° to 19° N and from 50° to 59° W (coloured lines). The black line is the average over all 10 years. The dotted horizontal line indicates 0 m/(s km). Data are from the ERA5 reanalysis.

2.2.3 Winds

The winds in our simulations are subjected to a large-scale forcing that involves only the pressure-gradient and Coriolis forces:

$$\left(\frac{du}{dt}\right)_{ls} = fv - \frac{1}{\rho}\frac{dp}{dx} \quad = \quad f(v - v_g), \tag{2.2}$$

$$\left(\frac{dv}{dt}\right)_{ls} = -fu - \frac{1}{\rho}\frac{dp}{dy} \quad = \quad -f(u - u_g), \tag{2.3}$$

where f is the Coriolis parameter, ρ the density, p the pressure, and u_g and v_g are the geostrophic winds. We use initial profiles of zonal and meridional winds that are equal to the imposed geostrophic wind ($u_0, v_0 = u_g, v_g$). We neglect large-scale horizontal wind advection, so that departures in the wind away from the geostrophic profiles are entirely due to the Coriolis force and the frictional force stemming from turbulence and convection. Because initially, the surface winds are in geostrophic balance, the simulation will undergo a transition towards ageostrophic surface winds (an Ekman balance). In this transition, the wind shear is effectively felt and adjusted through vertical mixing.

We based the wind profiles in our simulations on typical conditions in the trades, where vertical shear in the zonal wind component u is most common and to first order set by large-scale meridional temperature gradients through the thermal wind relation:

$$\frac{\partial u_g}{\partial z} \simeq -\frac{g}{fT}\frac{\partial T}{\partial y}, \tag{2.4}$$

where T is the temperature and g the gravitational constant. In the northern hemisphere, temperature decreases poleward ($\partial_y T < 0$), so that $\partial_z u_g > 0$, which implies that winds become increasingly westerly (eastward) with height. $\partial_z u > 0$ is indeed typical for most of the year, as derived from daily ERA5 data (12:00 UTC) from 2008 to 2017 within 9°–19° N and 50°–59° W (Fig. 2.2). In boreal summer, when the ITCZ is located in the northern hemisphere and meridional temperature differences within the subtropical belts are smaller, $\partial_z u$ is closer to zero or even negative. Vertical shear in the meridional wind component is close to zero year-round (not shown).

Table 2.1: Overview of the various LES experiments on a large (50.4 × 50.4 km^2) or small domain (12.6 × 12.6 km^2) and with interactive (constant SST) or fixed surface fluxes. For each set, we differentiate between runs without wind shear (NS), runs with weak (1X), medium (2X) or strong (4X) backward (BS) shear and runs with medium or strong forward (FS) shear (see also Fig. 2.1d).

Shear	acronum	NS	BS			FS	
			1X	2X	4X	2X	4X
	$[10^{-3}\ \text{s}^{-1}]$	0.0	+0.9	+1.8	+3.6	−1.8	−3.6
Large domain	interactive sur–face fluxes	√	√		√		√
	prescribed sur–face fluxes	√	√		√		√
Small domain	prescribed sur–face fluxes	√	√	√	√	√	√

2

Further analysis of daily profiles (not shown) reveals substantial day–to–day vari–ability in the zonal wind profiles, regardless of the season, with reversals from negative to positive shear or zero shear from one day to the next, or vice versa. Forward shear (here $\partial_z u < 0$) is to some extent a frequent feature of the atmospheric flow in the trades — not only during summer. However, backward shear (here $\partial_z u > 0$) is still the most common.

The magnitude of shear we imposed in our simulations is not far from what we derived from ERA5. We ran simulations with different values of zonal shear, while setting $\partial_z v_g = 0$. The zonal wind profile has either no shear (NS, solid black line in Fig. 2.1d), forward shear (FS, $\partial_z u_g < 0$, orange lines) or backward shear (BS, $\partial_z u_g > 0$, green lines). The FS and BS simulations have different shear strengths ranging from $|\partial_z u_g| = 0.9 \times 10^{-3}$ s^{-1} (1X, dotted line in Fig. 2.1d) over $|\partial_z u_g| = 1.8 \times 10^{-3}$ s^{-1} (2X, dashed lines) to $|\partial_z u_g| = 3.6 \times 10^{-3}$ s^{-1} (4X, solid coloured lines); see also Table 2.1.

The response to shear is not entirely insensitive to the choice of advection scheme. Here, scalar and momentum advection was performed using a 5th–order advection scheme in the horizontal direction and a 2nd–order advection scheme in the vertical direction. Using a 2nd–order scheme in the horizontal further increased the differences among the shear cases (in particular under free surface fluxes), which we attribute to the fact that the 2nd–order scheme accumulates a lot of energy on the smallest length scales close to the grid size. To reduce horizontal advective errors and allow for a larger time step, the grid was horizontally translated using a velocity that is equal to the imposed wind at 3 km height (Galilean transform, see e.g. Wyant et al., 2018).

2.2.4   Surface fluxes

The control simulations were run for two days with interactive surface fluxes, which are parametrised using standard bulk flux formulae:

$$(\psi w)_s = -C_S U_1 (\psi_1 - \psi_s), \tag{2.5}$$
$$u_* = \sqrt{C_M} U_1, \tag{2.6}$$

where $\psi \in \{q_t, \theta_l\}$, U is the wind speed, u_* the surface friction velocity, and the subscripts s and 1 stand for the surface values and values on the first model level, respectively. The

constants C_S and C_M are the drag coefficients, and they depend on the stability and on the scalar and momentum roughness lengths, which we both set to $z_0 = 1.6 \times 10^{-4}$ m. The drag coefficients are computed following Monin-Obukhov similarity theory (as described in Heus et al., 2010). Additionally, a set of experiments was conducted in which the surface fluxes were kept constant.

2.3   Impact of shear on cloud- and boundary-layer evolution

We first focus on the differences in cloud and boundary-layer structure that have developed by the end of a two-day simulation, using twelve-hourly averaged profiles (hour 36–48), unless noted otherwise.

2.3.1   Interactive surface fluxes

Similar to the findings of Brown (1999), who ran simulations for different wind shear on a very small domain (6.4×6.4 km^2), the influence of shear (Fig. 2.3b–d) on the thermodynamic structure of the boundary layer is overall marginal (Fig. 2.3a–b), but nonetheless evident in the relative humidity (RH), cloud fraction, liquid water and rain water profiles (Fig. 2.4a–d). In the presence of shear, regardless of its direction, cloud fractions above cloud base (approximately 700 m) are larger. In the FS-4X case the layer above 2 km is notably moister, whereas the BS-4X case has a more pronounced decrease of RH (which we interpret as the boundary-layer top) around 2 km. From strong backward to strong forward shear we thus observe a deepening of the moist layer and the disappearance of a pronounced hydrolapse.

Differences in the depth of convection are best seen from the rain water profiles (Fig. 2.4d) as well as the time series of average and maximum cloud-top heights (CTH), surface precipitation and low cloud cover, defined as the projected cloud amount from heights up to 4 km (Fig. 2.5a, c, e, g). Differences in cloud tops start to be pronounced only on the second day of the simulations, but looking closer, one can see that the highest cloud tops on day one are those of the FS-4X simulations (in orange). On day two, the NS simulation develops the deepest clouds with even an average cloud top near 7 km, whereas clouds in the simulations with shear, regardless of its sign, remain shallower and rain less. During the final twelve hours, clouds in all simulations show a pronounced deepening, and the FS-4X case even develops deeper clouds than the NS case, as well as more rain. Because we only use a simple single-moment ice microphysics scheme here, we are cautious with the interpretation of the cloud field when it deepens beyond the freezing level. Instead, we wish to focus on the deepening from shallow cumuli to congestus with tops near 4 km. Apparently, shear plays a role at hindering that development, in particular under BS.

Figure 2.5 shows that the surface heat fluxes play a key role in the deepening responses. Heat fluxes diverge very early on in the simulations, whereby the largest and smallest fluxes develop for the FS-4X and BS-4X cases, respectively (Fig. 2.5m, o). This exemplifies an important and perhaps often overlooked influence of wind shear. Given the same constant (geostrophic) forcing at the surface, a difference in zonal wind velocities can develop at the surface, due to the different zonal wind shear, which is felt near the surface through turbulent mixing, at first, and then also through the Coriolis force as

2

Figure 2.3: Slab–averaged profiles of thermodynamic quantities of the large–domain simulations with interactive surface fluxes (top row, a–d), with prescribed surface fluxes (middle row, e–h) and small–domain simulations (bottom row, i–l). Shown are averages over the last twelve hours of each simulation of (a, e, i) the liquid water potential temperature θ_l and (b, f, j) zonal, (c, g, k) meridional and (d, h, l) total wind velocity, u, v and U, respectively. The line colours and types are explained in Fig. 2.1 and are the same in all following figures.

the wind starts to turn (see Eq. 2.2 and Fig. 2.3b–c). These differences in surface winds (Fig. 2.5i) give rise to the differences in surface fluxes (see Eq. 2.5).
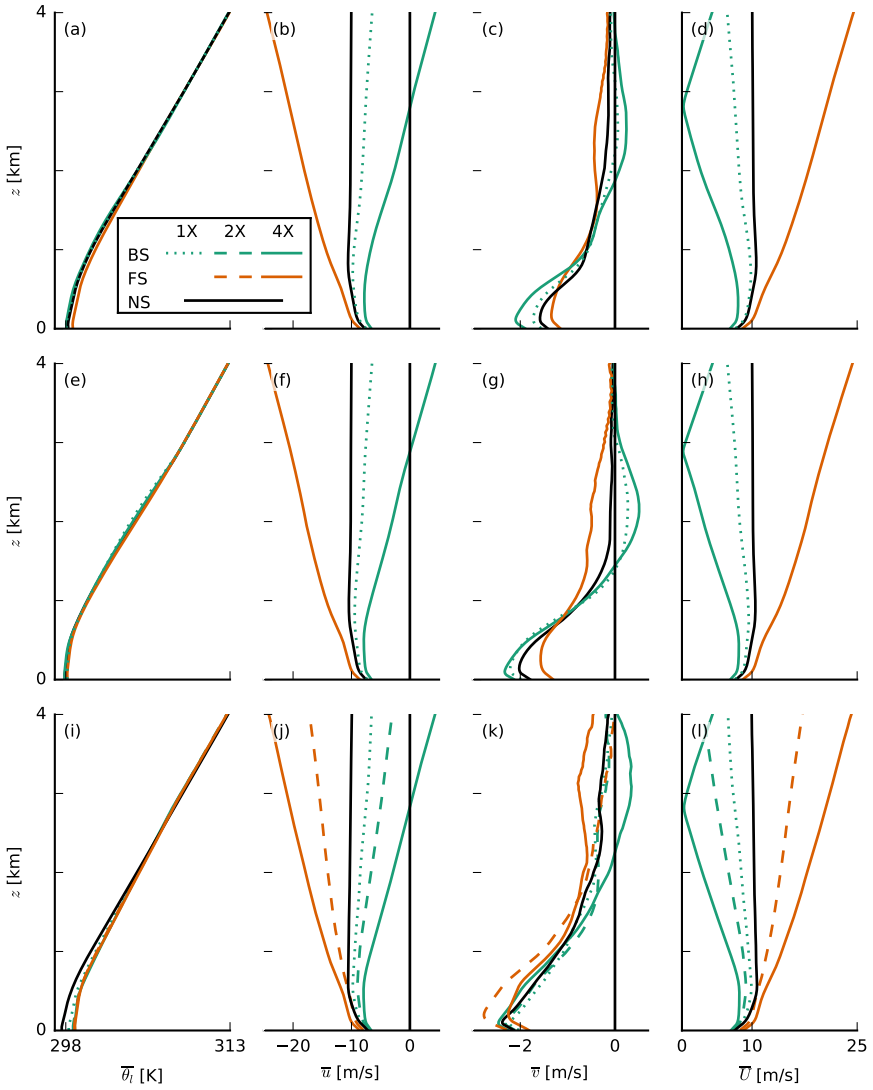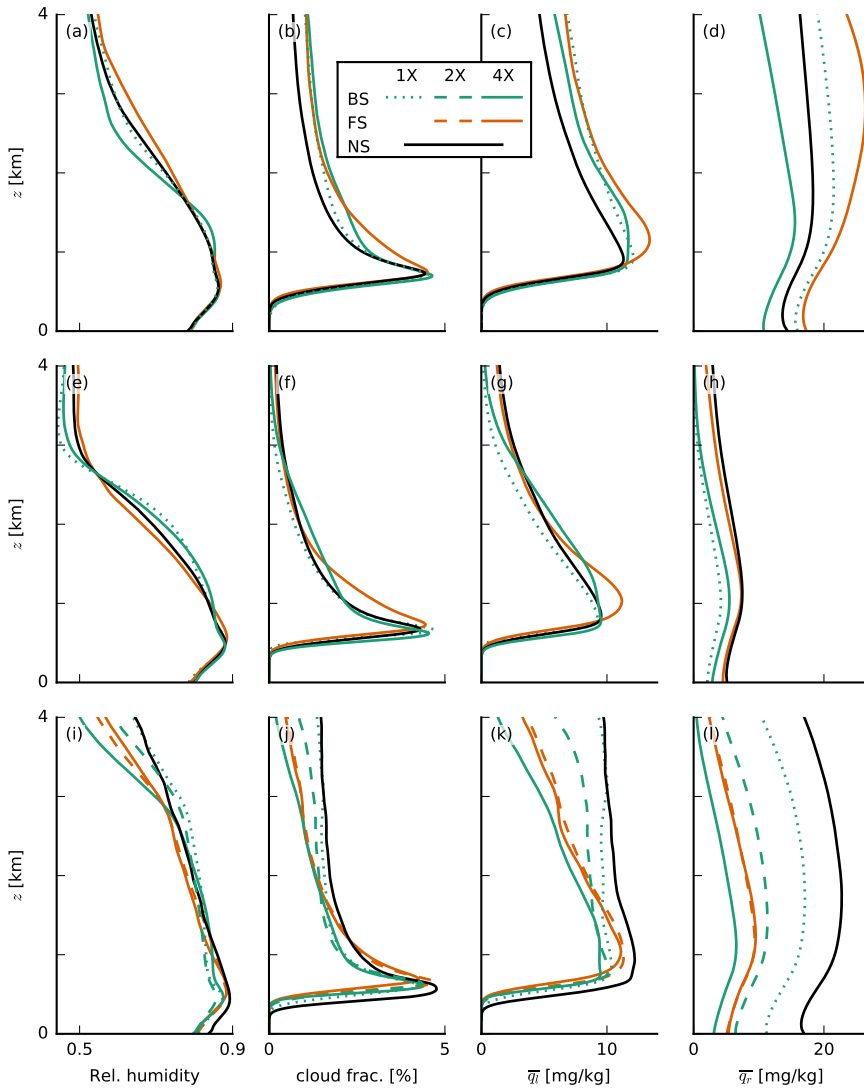
Figure 2.4: Slab–averaged profiles of thermodynamic quantities of the large–domain simulations with interactive surface fluxes (top row, a–d), with prescribed surface fluxes (middle row, e–h) and small–domain simulations (bottom row, i–l). Shown are averages over the last twelve hours of each simulation of (a, e, i) the relative humidity, (b, f, j) cloud fraction, (c, g, k) liquid water specific humidity q_l and (d, h, l) rain water specific humidity q_r.

As clouds deepen in all simulations during day two, the difference in surface heat fluxes becomes smaller, as downward mixing of warm and dry free tropospheric air reduces the surface sensible heat flux while promoting the latent heat flux (Nuijens & Stevens, 2012). The increase in the sensible heat fluxes in the final six hours may be attributed to

2
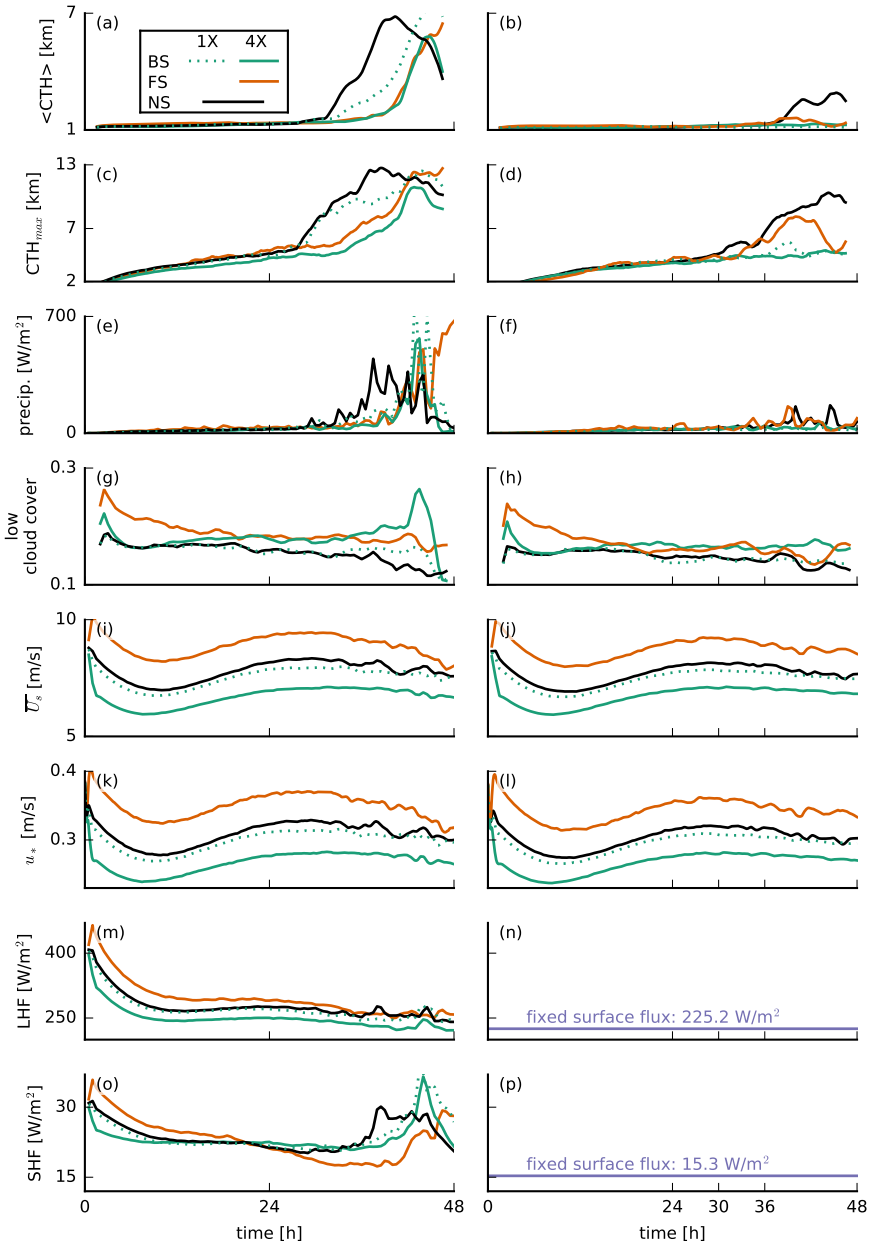
Figure 2.5: Time series of (a, b) the average and (c, d) the maximum cloud-top height (CTH), (e, f) the surface precipitation flux, (g, h) the low cloud cover ($z < 4$ km), (i, j) the domain-averaged total wind speed at 5 m height U_s, (k, l) the surface friction velocity u_*, (m, n) the surface latent heat flux LHF and (o, p) the surface sensible heat flux SHF for the interactive- (left column) and prescribed-surface-flux simulations (right column).

precipitation and evaporative cooling of rain water in the subcloud layer (e.g. cold pools, Fig. 2.5e).

2.3.2 Prescribed surface fluxes

In light of these results, an important question is whether the surface fluxes are the only factor that plays a role in the development of convection, or whether shear has other more direct effects, including on the organization of clouds. Therefore, we carried out simulations with prescribed surface heat fluxes with relatively low magnitudes (namely $SHF = 15.3$ W m^{-2} and $LHF = 225.2$ W m^{-2}, see the right column in Fig. 2.5 and second row in Figs. 2.3 and 2.4) as to minimize the development of very deep convection. Note that the surface friction (or surface momentum flux) is unchanged (Fig. 2.5k, l).

Apparently, the sensitivity of cloud deepening to shear does not change its overall character when we prescribe the surface heat fluxes. Clouds are overall shallower with lower cloud fractions above 1 km (Fig. 2.4f, Fig. 2.5b, d), because the prescribed surface fluxes are smaller than in the interactive flux runs. But the FS–4X case still develops the largest relative humidities above the boundary layer (>2.5 km), whereas the BS–4X case has the most pronounced hydrolapse near the boundary-layer top (Fig. 2.4e). Again the FS–4X case tends to produce somewhat deeper clouds during day one, but falls behind the NS case on day two. The BS–4X and BS–1X cases remain even shallower.

From previous studies (e.g. Malkus, 1949; Neggers et al., 2003; Yamaguchi et al., 2019) it is known that shear tilts clouds and thus increases cloud cover. In our FS and BS simulations, the tilt occurs in the negative and positive x direction, respectively, which enhances the low cloud cover by 10–20 % (Fig. 2.5g, h). A similar increase develops within a short time also after instantaneously introducing shear into a previously non-sheared system (Fig. 2.6c, discussed below). Besides this expected impact on cloud cover, there are also some small differences in the cloud fraction profiles — including near cloud base, whose sensitivity has received much attention in recent climate studies (e.g. Vial et al., 2017; Bony et al., 2017). In the presence of shear, we observe a slightly larger maximum cloud fraction near cloud base (500–700 m) in the simulations with prescribed surface heat fluxes (Fig. 2.4b, f), in line with previous studies (e.g. Brown, 1999; Yamaguchi et al., 2019). BS–4X has a higher q_t variance at these heights, which are due to a few per cent more active cloud (not shown) and which could explain the higher cloud fraction. In the FS–4X case, the larger cloud-base cloud fraction is explained by more passive cloud (not shown).

2.3.3 Sensitivity tests on a smaller domain

The same difference in deepening between the shear cases can be observed when applying instantaneous perturbations to the (geostrophic) wind shear, while keeping the surface fluxes constant (Fig. 2.6). In these sensitivity tests, carried out on a 16-fold smaller domain (see Table 2.1, which is still 4 times as large as the one used by Brown (1999)) we start from the equilibrium state of the NS case after two days, and then apply a perturbation. We then let the system evolve for another 36 hours. Also here it is evident that when wind shear is introduced, convective deepening is prevented (Fig. 2.6a–b) in comparison with how the simulation develops without a perturbation (dashed black line
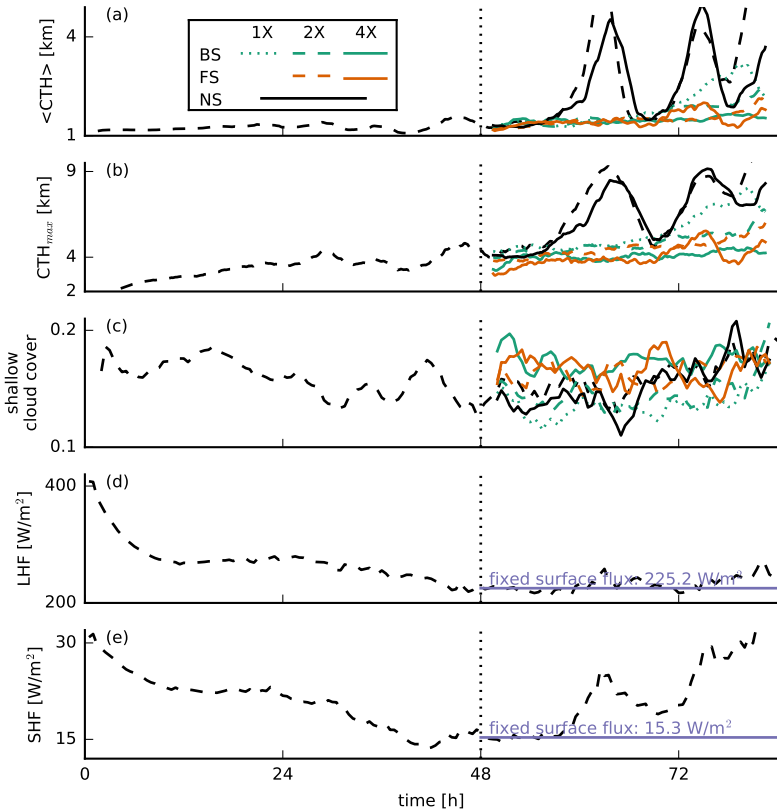
2

Figure 2.6: Time series of (a) the average and (b) the maximum cloud–top heights (CTH), (c) the low cloud cover ($z < 4$ km) and the (d) surface latent and (e) surface sensible heat fluxes for the small–domain simulations (48–84 h). In addition to the standard line types (see Fig. 2.1), the dashed black lines indicate a non–sheared simulation with interactive surface fluxes that is used to initialise the simulations at $t = 48$ h by perturbing the wind profiles and fixing the surface fluxes.

in Fig. 2.6). Even very weak shear (BS–1X, dashed green line) can effectively reduce the clouds' depth and delay cloud deepening.

It is worthwhile to compare the profiles of RH and cloud fraction on the small domain (Figs. 2.3i–l and 2.4i–l) with those on the large domain. The 16–fold smaller domain leads to much higher relative humidities and cloud fractions above 2 km. This can be explained by the lack of spatial organization of shallow convection on the small domain. Increasing the domain size generally tends to organize the shallow convection into deeper and larger clusters, which leads to a shallower, warmer and drier domain. Vogel et al. (2016) found that on a larger domain the likelihood of developing a strong updraft and deep cloud increases and that larger domains support stronger and deeper updrafts by allowing them to spread their compensating subsidence over a larger area. In the absence of spatial organization on the small domain, we can observe that only the FS–4X case behaves differently compared to the large domain. This case is no longer comparably moist or
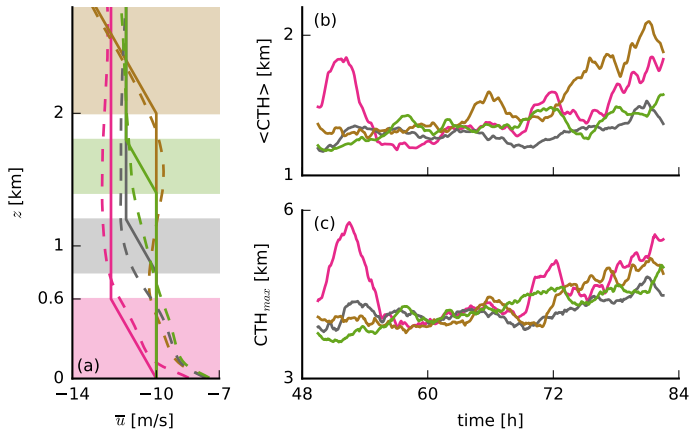
Figure 2.7: (a) Initial (solid lines) and slab–averaged profiles (from the last twelve hours; dashed lines) of the zonal wind u of simulations in which shear is only applied at limited height levels, as well as (b–c) the corresponding time series of the (b) average and (c) maximum cloud–top heights. Pink lines depict FS–4X shear at 0–0.6 km, grey at 0.8–1.2 km, green at 1.4–1.8 km and brown at 2–10 km.

even moister than the NS case and its cloud fraction and RH profile is now more in line with that of the BS–4X case. This hints at a role of spatial organization in explaining the response to forward shear, which we address later.

Using the same experimental set–up (i.e. small domain, fixed surface fluxes and sudden perturbation of the wind profile), we carried out some further sensitivity tests in which we applied forward shear to specific layers (Fig. 2.7). These simulations show that shear is particularly effective at keeping convection shallow when applied in the lower cloud layer (grey and green lines in Fig. 2.7), whereas shear in the subcloud layer (pink) or near cloud tops (brown) still leads to cloud deepening.

2.4 Sensitivity of convective deepening to shear

Overall, the previous section has shown that the presence of even weak backward shear effectively inhibits convective deepening, while forward shear only slightly weakens the potential to develop deeper clouds: This inhibition reveals itself as a delay (if surface feedbacks are present) or as a complete suppression of deepening (if surface heat fluxes are fixed). On a smaller domain, forward shear has the same strong inhibitive effect as backward shear. If not through a surface flux response, what is the mechanism through which backward shear oppresses convection, while forward shear seems to allow for cloud deepening (on a sufficiently large domain)? Two hypotheses, borrowed from studies of deep convection, are as follows:

1. Wind shear changes the rate of entrainment, the updraft buoyancy and updraft speed: As clouds get tilted through any absolute amount of shear, they may suffer
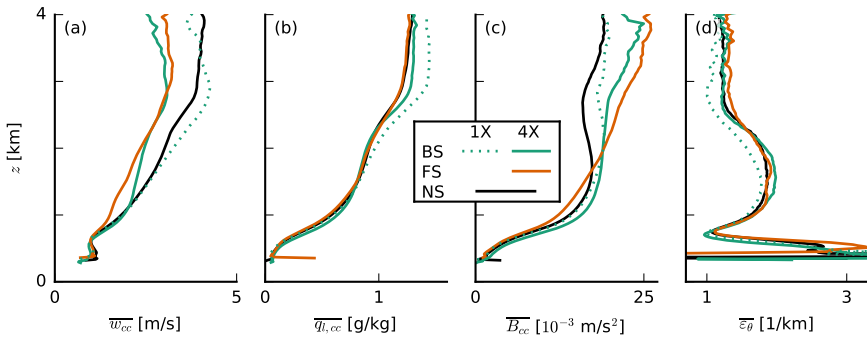
Figure 2.8: Slab-averaged profiles of (a) the cloud–core vertical velocity w_{cc}, (b) the cloud–core liquid water specific humidity $q_{l,cc}$, (c) the cloud–core buoyancy B_{cc} and (d) the fractional entrainment rate ε_θ of θ_l (averaged from 30 to 36 h of the simulations with prescribed surface fluxes).

from more lateral entrainment and opposing pressure perturbations that limit updraft speeds and cloud vertical extent.

2. Wind shear changes the structure and organization of shallow cloud systems. For instance, forward shear helps to separate regions of updrafts and downdrafts and may therefore sustain larger subcloud circulations that continue to feed moisture into already cloudy areas. Forward shear may also interact with cold–pool fronts to force stronger updrafts.

To investigate these ideas, we consider only the simulations with prescribed surface fluxes and focus on the period between 30 and 36 h (unless noted otherwise). In this period, clouds first start to deepen from shallow cumulus to congestus at different rates depending on shear, and the cloud field has not developed deep convection yet (cf. Fig. 2.5b, d).

2.4.1   Entrainment and updraft speeds

The FS-4X and BS-4X cases have significantly lower updraft speeds in the cloud cores ($q_l > 0$ and $\theta_v' > 0$) compared to the NS and BS-1X cases (Fig. 2.8a), which appears key to explaining the lower cloud–top heights that develop under shear. However, the strongly sheared simulations contain nearly the same amount of cloud-core liquid water and are notably more buoyant, especially above 2 km (Fig. 2.8b, c). A similar picture is established if we sample on cloudy points ($q_l > 0$). Furthermore, the vertical mass flux is hardly affected by shear (not shown), as also found by Neggers et al. (2003). Buoyancy itself is evidently not key to explaining the weaker updrafts under shear (although it likely explains the stronger updrafts below 1 km in the BS-4X case). The relatively low buoyancy in cloud cores of the NS case (at least above 2 km) is because the environment surrounding the non–sheared clouds is warmer in terms of θ_v (not shown), because clouds in that simulation are already mixing across a deeper layer (Fig. 2.5d), while the clouds themselves have a similar θ_v in each case. Vogel et al. (2016) also showed how quickly the thermodynamic structure of the boundary layer changes as shallow cumuli develop into cumulus congestus.
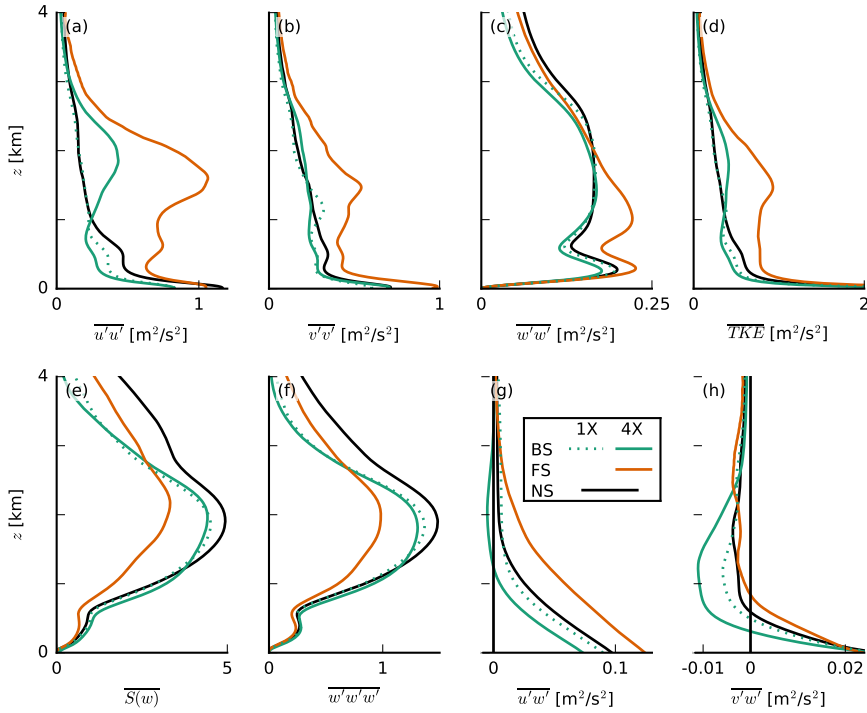
Figure 2.9: Slab–averaged profiles of the resolved variances of (a) the zonal wind velocity $u'u'$, (b) the meridional wind velocity $v'v'$ and (c) the vertical velocity $w'w'$, (d) the turbulence kinetic energy (TKE), (e) the skewness $S(w)$, (f) the third moment $w'w'w'$ of the vertical velocity and (g) the zonal and (h) the meridional momentum fluxes, $u'w'$ and $v'w'$, respectively (averaged from 30 to 36 h of the simulations with prescribed surface fluxes).

Using the simple entraining plume model by Betts (1975) to calculate the fractional entrainment rate ε_θ of θ_l (Fig. 2.8d), we find that clouds in the BS and FS cases entrain only marginally more environmental air than in the NS case if anything (also if we consider entrainment of q_t, not shown). This suggests that there is no larger lateral entrainment due to shear that could explain weaker vertical development. We also find that lateral entrainment plays a relatively small role in the conditionally sampled vertical–velocity budget (Appendix 2.A).

The weaker cloud–core vertical velocities under shear are in line with studies of deep convection in squall lines, in particular the recent study by Peters et al. (2019) and ear-lier work by similar authors (Parker, 2010; Peters, 2016), who show that slanted updrafts are weaker than upright ones. Peters et al. (2019) decompose the vertical momentum equation into four terms that describe the processes that regulate the vertical acceler-ation of updrafts: (1) a term associated with momentum entrainment and detrainment, (2) a (downward–oriented) dynamic pressure acceleration term, (3) a (downward–oriented) buoyancy pressure acceleration term and (4) a buoyancy acceleration term (which includes the entrainment of thermodynamic properties that can limit updraft buoyancy). They show
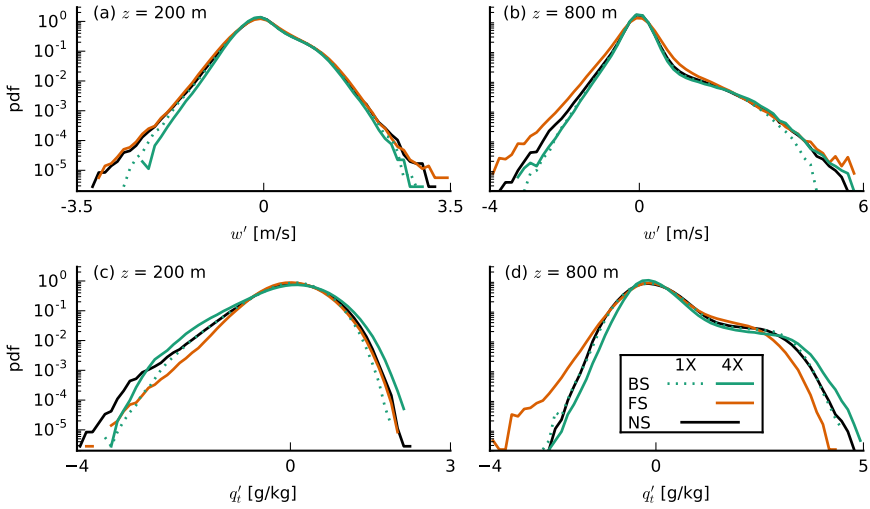
Figure 2.10: Probability density functions of the vertical velocity w (top) and the total water specific humidity deviations q'_t (bottom) at constant heights of (left) $z = 200$ m and (right) $z = 800$ m (averaged from 30 to 36 h of the simulations with prescribed surface fluxes).

that shear mostly enhances the dynamic pressure perturbations, which can be interpreted as an aerodynamic lift force due to the shear-driven crossflow (perpendicular to the direction of ascent). Unlike the lift associated with aircraft wings, the lift in slanted thermals experiencing crossflow is directed downward. A handful of studies on the vertical-velocity budget of shallow convection have also noted a minor role of entrainment in explaining updraft speeds (e.g. De Roode et al., 2012; Romps & Charn, 2015; Morrison & Peters, 2018; Tian et al., 2019).

An investigation of the vertical-velocity budget — a subject on its own as demonstrated by the aforementioned studies — goes beyond our goal, but we can get an impression of the importance of the pressure perturbations by sampling the vertical-velocity budget in cloudy updrafts, following De Roode et al. (2012), here included in 2.A. We find that differences that contribute to the vertical velocity in the cloud layer are predominantly found in the pressure-gradient and buoyancy terms, whereas differences in the horizontal flux of resolved and subgrid vertical momentum across the cloud boundaries (e.g. entrainment) are only important near cloud base (< 1 km) where other tendencies are small. Near cloud tops (> 2 km), updrafts in the sheared runs experience a larger negative pressure-gradient force. A quick look at the total pressure perturbations in x–z cross sections also confirms that pressure perturbations, especially near the slanted sides and tops of the clouds, are more pronounced under shear (not shown).

Overall, our results emphasise that shear keeps clouds shallower by weakening updrafts. However, we also observe that clouds under forward shear have a tendency to get deeper than under backward shear. This is explored next.
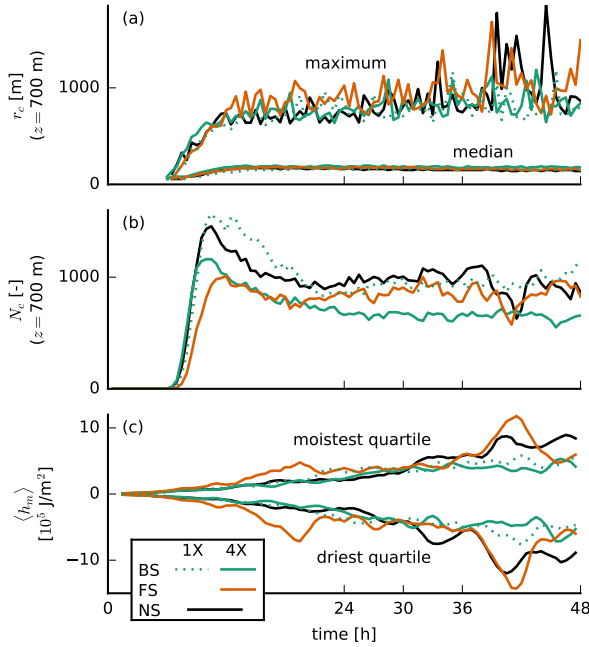
Figure 2.11: Time series of (a) the median and maximum cloud radius r_c at $z = 700$ m, (b) the number of clouds N_c at that height and (c) the vertically integrated moist static energy anomalies $\langle h_m \rangle$ in the moistest and the driest quartiles of 12.6×12.6 km^2 blocks for the simulations with prescribed surface fluxes.

2.4.2 Structure and organization of turbulence and clouds

In Fig. 2.9 we show a number of quantities that reveal changes to the character of the turbulence structure of the boundary layer: the domain-averaged variances of the velocity components, the turbulence kinetic energy (TKE), the skewness S and third central moment of the vertical velocity $\overline{w'^3}$ and finally the zonal and meridional momentum fluxes. Velocity variances are clearly enhanced in the FS-4X case, where the vertical gradient in wind speed between the surface and cloud tops — the shear — is largest (cf. Fig 2.3f–h). Consequently, TKE and the momentum fluxes are larger, in agreement with Brown (1999). Momentum fluxes at the surface are also largest for the FS-4X case, leading to a larger surface friction (see also Fig. 2.5i, j) and larger surface-layer shear.

Several authors have noted that convection can transition from a closed-cell structure to roll structures due to shear (e.g. Sykes & Henn, 1989; Khanna & Brasseur, 1998; Salesky et al., 2017). A parameter that controls this transition is the ratio of the surface friction velocity u_* to the convective velocity scale w_* (Sykes & Henn, 1989) or equivalently the ratio of the Obukhov length and the boundary-layer height. While the exact value of u_*/w_* at which the transition takes place depends on other properties of the flow (different studies report values between 0.27 and 0.65), low values are clearly associated with cellular convection and high values with roll structures (Fedorovich & Conzemius, 2008; Salesky et al., 2017). In our simulations, u_*/w_* has rather low values, which do
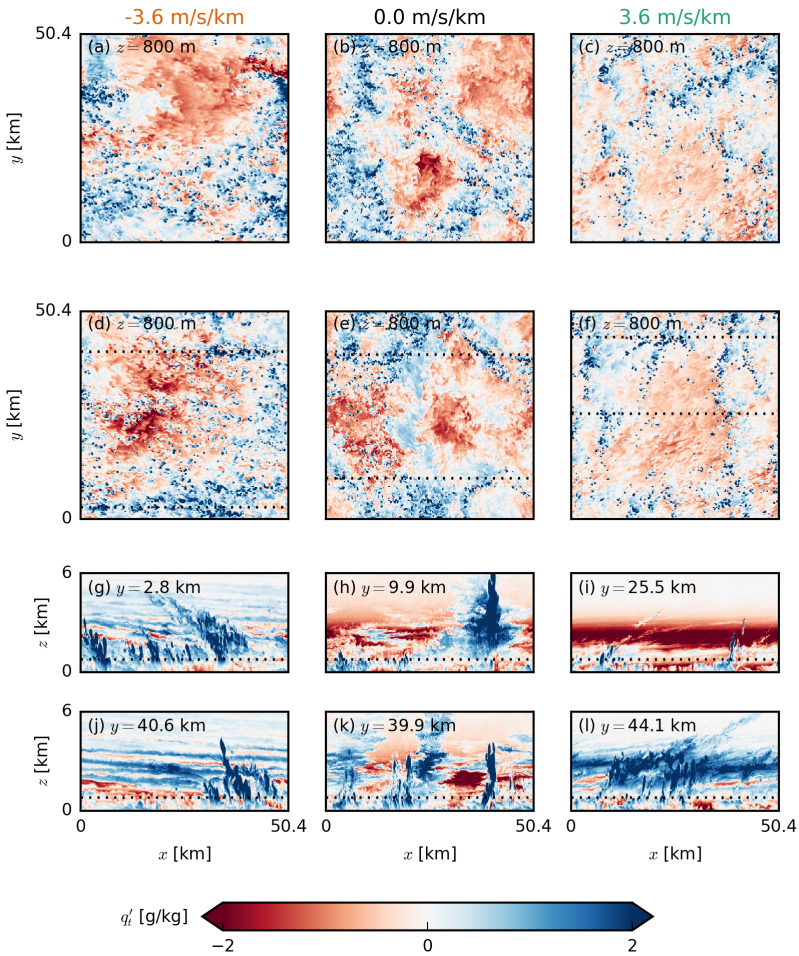
Figure 2.12: Snapshots of the LES domains of FS-4X (left), NS (centre) and BS-4X (right) exhibiting typical characteristics in the late stages of the simulations with prescribed surface fluxes. The top two rows (a–f) show horizontal x–y cross sections at two times ($t = 39.0$ h and $t = 46.5$ h) near cloud base ($z = 800$ m) of the deviations from the mean of the total water specific humidity q_t'. The bottom two rows (g–l) show corresponding vertical x–z cross sections from the lowest 6 km of the domain of the latter of the two times (d–f). The horizontal dotted lines indicate the position of the respective other cross sections.

not differ greatly among the various shear cases (ranging from about 0.30 for BS-4X to 0.37 for FS-4X), indicating that convection is mainly buoyancy- and not shear-driven in all our simulations.

The skewness of the vertical velocity $S(w) = \overline{w'^3}/\overline{w'^2}^{\frac{3}{2}}$, which is a measure for the asymmetry of the vertical velocity distribution, is reduced with FS. This is primarily caused by the reduction in the advection of vertical velocity variance, $\overline{w'^3}$, due to on average weaker updrafts into the cloud layer (Fig. 2.8a). The variance of w instead is
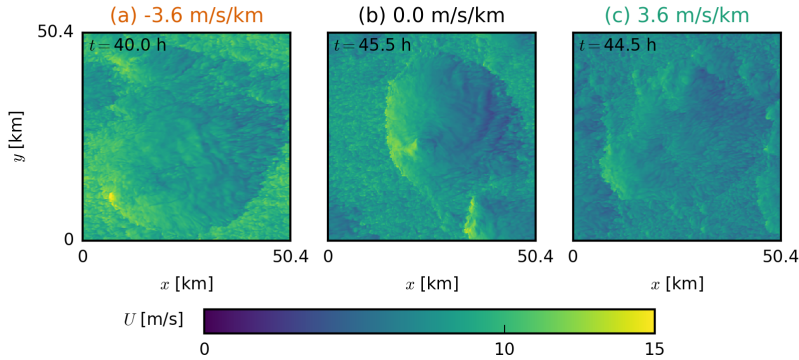
Figure 2.13: Snapshots of the LES domains of (a) FS–4X, (b) NS and (c) BS–4X exhibiting typical characteristics of the total wind speed U in the late stages of the simulations with prescribed surface fluxes. Shown are horizontal x–y cross sections at $z = 5$ m.

larger under FS–4X (Fig. 2.9c). Although the PDFs of w at 200 m and at 800 m (near cloud base) in Fig. 2.10a–b are overall very similar, the FS–4X case has notably stronger updrafts as well as stronger downdrafts (tails of the PDF). This might be a signature of the downdrafts being separated from the updraft regions. Because the FS–4X case also has the largest absolute amount of wind shear across the subcloud layer, it has the largest positive (anticlockwise) vorticity. These results suggest that instead of narrow updrafts closely surrounded by subsidence, the FS–4X case develops stronger ascent and descent in separated branches of a circulation that enhances moisture transport into cloudy areas.

Indeed, the FS–4X case has the largest amount of domain–averaged liquid water and cloud fraction between 800 m and 1.5 km on both small and large domains (Fig. 2.4f, g, j, k) and larger relative humidities just above cloud base (Fig. 2.4e, i), even though cloud base is on average higher than for the BS and NS cases. By analysing the mean and maximum cloud radii and the number of clouds, we also find that the FS–4X case develops the fewest but the largest clouds (Fig. 2.11a, b), whereas the NS case has more numerous smaller clouds, similar to findings by Yamaguchi et al. (2019).

The formation or aggregation of larger clouds is also evident from the moisture field. Figure 2.11c shows deviations of the vertically integrated moist static energy within blocks of 12.6×12.6 km^2 compared to the domain mean, and compares the moistest and the driest quartiles of the domain (in terms of total water path), which is a common measure for self–aggregation (Bretherton & Blossey, 2017). This reveals that during the first 24 h the strongest moistening of the moist regions and strongest drying of the dry regions takes place in the FS–4X cases. Furthermore, snapshots of the moisture field (Fig. 2.12) show that large patches of high or low moisture are less common in the simulations with backward shear compared to the other cases.

After the first day of simulation when precipitation increases, cold–pool effects might play an additional role in organizing the cloud and moisture field. The cold–pool boundaries may interact with the environmental shear in the subcloud layer to trigger stronger force–lifted updrafts under FS (e.g. Li et al., 2014). The FS and BS cases also have a

different wind speed distribution within the cold pools (Fig. 2.13). Whereas the BS case reveals the typical diverging flow with a strong easterly current left from the cold pool center and relatively stronger westerly winds towards the right, the FS case has much stronger easterly winds throughout. This may signify a role of downward momentum transport as well. The role of cold pool–shear interaction is the subject of a follow–up study.

2.5   Conclusions

In this paper, we have used idealised large–eddy simulations initialized and forced with a geostrophic wind that is equal at the surface, but has a different vertical profile (vertical wind shear). We showed that vertical wind shear influences the depth and characteristics of shallow cumulus convection, and thereby the depth and structure of the trade–wind layer. Even weak vertical shear in the zonal wind component can retard the growth of cumulus clouds, in particular when the shear vector is directed against the mean wind direction (backward shear). Furthermore, we have shown that shear increases the cloud fraction — an effect that has been of major interest in recent climate studies (e.g. Vial et al., 2017; Bony et al., 2017).

Backward shear, whereby surface easterlies become upper westerlies, is typical for the winter trades, presumably because this season has a larger meridional temperature gradient between the equator and subtropics. Simulations with interactive surface fluxes reveal that backward shear can slow down vertical cloud development. Under backward shear, mean cloud tops remain near 2 km for at least 36 hours of simulation, at which point the simulations without (imposed) shear have developed clouds with mean tops near 7 km. Given the same geostrophic wind forcing at the surface, and in absence of horizontal wind advection, the weakest surface winds develop under backward shear. When initialising the simulations with surface winds in geostrophic balance, and no horizontal wind advection is applied, the weakest surface winds are reached under backward shear as the simulation approaches an Ekman balance: Relatively weaker wind speeds are then mixed towards the surface, compared to the simulations with forward shear or no shear.

Weak shear and forward shear (easterlies become stronger with height) are not un–common during boreal winter, even if they are more typical for boreal summer when the ITCZ and deep convection shift northward. The vertical development of clouds under for–ward shear is also delayed, but not as much as with backward shear, because simulations with forward shear develop the strongest surface winds and (initially) the largest surface heat fluxes.

To elucidate more direct effects of vertical shear, we repeated the simulations with prescribed surface heat fluxes. These show that the presence of shear in the cloud layer, regardless of its sign, limits updraft speeds, in line with studies of deep convection that have shown shear to inhibit convective development (e.g. Peters et al., 2019). Entrainment appears to play a minor role in setting the weaker updrafts (e.g. De Roode et al., 2012; Romps & Charn, 2015; Morrison & Peters, 2018; Tian et al., 2019). Instead, larger downward–oriented pressure perturbations under both forward and backward shear appear to weaken vertical accelerations.

In addition, shear changes the turbulence structure of the subcloud layer. Though our simulations remain buoyancy–driven and do not develop roll structures or cloud streets,

forward shear develops stronger updrafts and downdrafts, a moister layer near cloud base with larger cloud fraction, fewer but larger cloud clusters and more moisture aggregation. Forward shear maintains the largest absolute amount of shear in the sub-cloud layer, which leads to a larger background vorticity and separates regions with updrafts from regions with downdrafts. This may develop a stronger subcloud circulation with sustained regions of ascending motion that feed moisture into areas of clouds. The larger cloud clusters can become deeper, as they do in the first day of simulation under forward shear, but are ultimately limited by weaker updraft speeds.

As clouds remain shallower under backward shear, the moistening of the cloud layer is more pronounced and the top of the cloud layer is marked by a steeper decrease in humidity, as is typical near the trade-wind inversion (e.g. Riehl et al., 1951). The moister subcloud and cloud layer, as well as a stronger inversion, will lead to more cloudiness. Therefore, we may argue that the trade winds themselves help to set the trade-wind inversion and thus that backward shear is a crucial ingredient in defining the typical trade-wind-layer structure.

2.A   Impact of shear on the vertical-velocity budget

To study a difference in the forcing acting on the vertical velocity of cloudy updrafts in simulations with and without shear we follow the method by De Roode et al. (2012) who applied the top-hat approach by Siebesma & Cuijpers (1995) to compute the conditionally sampled vertical-velocity budget in DALES:

$$\frac{\partial w_c}{\partial t} = \underbrace{\frac{g(\theta_{v,c} - \overline{\theta_v})}{\theta_0}}_{B} - \underbrace{\left[\frac{\partial \pi}{\partial z}\right]_c}_{P} \underbrace{+2\Omega \cos \varphi u_c}_{C} - \underbrace{\frac{1}{2\rho}\frac{\partial w_c^2}{\partial z}}_{A} - \underbrace{\frac{1}{\rho\sigma_c}\frac{\partial \sigma_c \overline{w''w''}^c}{\partial z}}_{S_p} - \underbrace{\frac{\epsilon_w w_c^2}{1-\sigma}}_{E}, \quad (2.A1)$$

where the subscript c stands for conditional sampling (here: on cloudy updrafts, i.e. $q_l > 0$ and $w > 0$), g the gravitational acceleration, θ_v the virtual potential temperature, θ_0 a reference temperature, π the modified pressure, Ω Earth's angular velocity, φ the latitude, σ the area fraction, ϵ_w the fractional entrainment rate of w and ρ the slab-mean density. The modified pressure π is defined as

$$\pi = \frac{1}{\rho}(p - \overline{p_h}) + \frac{2}{3}e, \quad (2.A2)$$

where p is the pressure, p_h the hydrostatic pressure and e the subgrid-scale TKE. The latter is included because in DALES, $\frac{2}{3}e$ is subtracted from the subgrid momentum flux to simplify its computation; to compensate for this, the term is added back to the pressure (Heus et al., 2010). Preliminary tests show, however, that the subgrid TKE contribution to the conditionally sampled pressure term is small and insensitive to shear (not shown). The tendency on the l.h.s. of Eq. 2.A1 is calculated directly from the LES. Averaged over six hours (30 to 36 h) it is close to zero. This tendency closely matches the sum of the terms on the r.h.s., which represent the buoyancy acceleration (B), the vertical pressure gradient (P), the Coriolis force (C), the vertical advection (A), the subplume vertical advection (S_p), and the lateral entrainment E.
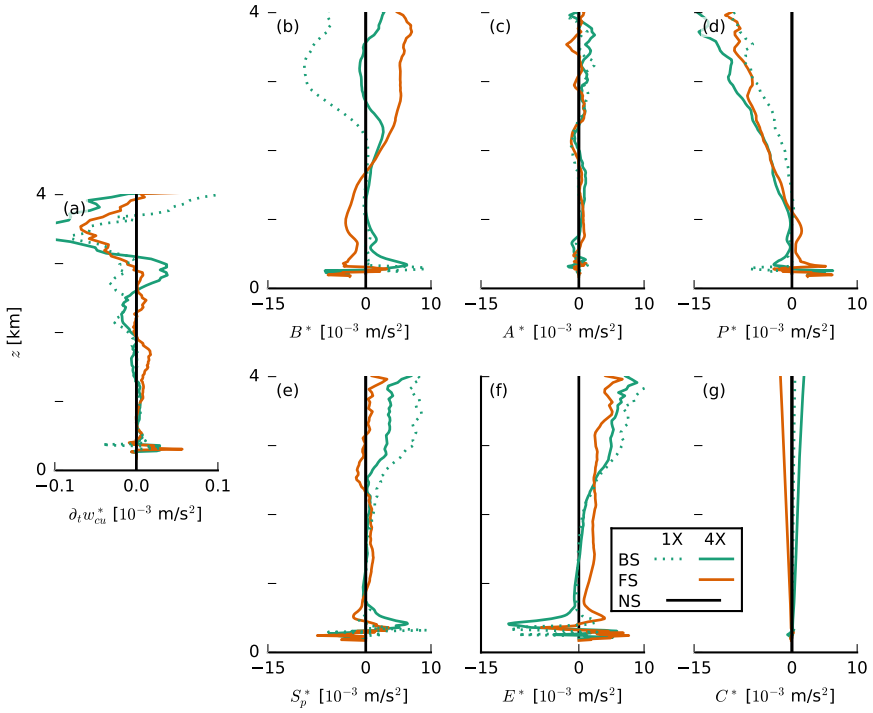
Figure 2.A1: Slab–averaged profiles (averaged from 30 to 36 h of the simulations with prescribed surfaces fluxes) of the terms of the cloudy–updraft vertical-velocity budget (Eq. 2.A1) plotted as differences from the NS case (indicated by the asterisks).

Above 1 km, in the cloud layer, the production of vertical velocity from positive buoy-ancy B is largely balanced by a sink of vertical velocity due to the pressure gradient P, followed by a smaller sink from advection A. The subplume term S_p is close to zero in the cloud layer, and C is also small (negative). The lateral entrainment term E is small yet positive, counter to the conventional idea that entrainment is contributing negatively to cloud updraft quantities. This unexpected sign of the diagnosed lateral entrainment rate was also observed by De Roode et al. (2012) who argued that changes in the number of sampled points as parcels enter or leave cloudy updrafts (so-called Leibniz terms) may violate the implicit assumption that lateral entrainment is dominated by horizontal ad-vection. As Young (1988) explained, any sampled derivative, such as of vertical velocity,

$$\left[\frac{\partial w}{\partial t}\right]_c = \frac{\partial w_c}{\partial t} + \frac{w_c}{\sigma}\frac{\partial \sigma}{\partial t} + \left\{\frac{\partial w}{\partial t}\right\}_L, \qquad (2.A3)$$

introduce an additional term that stems from Leibniz's rule of differentiation. It represents temporal changes in the sampled vertical velocity due to changes in the sampling set.

To let the lateral entrainment term in Eq. 2.A1 be consistent with parametrised vertical-velocity equations (see Eq. 3 in De Roode et al., 2012), we diagnosed it as

$$-\frac{\epsilon_w w_c^2}{1-\sigma} = -\frac{w_c}{\sigma}\frac{\partial \sigma}{\partial t} - \frac{w_c}{\sigma}\frac{\partial M_c}{\partial z} - \left[\frac{\partial u_h w}{\partial x_h}\right]_c - \left[\frac{\partial \tau_{3h}}{\partial x_h}\right]_c$$
$$-\left\{\frac{\partial w}{\partial t}\right\}_L - \left\{\frac{\partial w w}{\partial z}\right\}_L - \left\{\frac{\partial \tau_{33}}{\partial z}\right\}_L,$$

(2.A4)

where M_c is the mass flux. The Leibniz terms are of significant magnitude. Besides, a more complicated behaviour of vertical velocity than assumed in the top-hat approach is present (e.g. Heus & Jonker, 2008), therefore lending itself less well for estimating the fractional entrainment rate (as compared to thermodynamic quantities).

To explain how different forcings under shear can contribute to differences in the updraft speeds, Fig. 2.A1 shows these budget terms as deviations from the NS case. Positive values indicate a stronger positive contribution to updraft speed (or a smaller negative contribution). In particular, above 1 km, the FS and BS cases have a larger negative P contribution (Fig. 2.A1d), which is present at the same altitude where we see slower updraft speeds in the presence of shear (Fig. 2.8a). The differences in P are balanced mostly by differences in E (in the BS-4X case) or B (in the FS-4X case). The latter result from the different development of environmental temperature and humidity, as discussed in Section 2.4.1 and shown in Fig. 2.8c. The NS case with its strongest updrafts develops the deepest clouds and thus the warmest boundary layer, which reduces B, leading to a balance in the budget over six hours. It thus appears that initial differences in updraft speeds develop due to differences in pressure gradients under shear, which are maintained throughout the simulation, as a balance with the buoyancy force is established.

3

The morphology of trade-wind convection and cold pools under wind shear

A growing body of literature investigates convective organisation, but few studies to date have sought to investigate how wind shear plays a role in the spatial organization of shallow (trade-wind) convection. The present study hence investigates the morphology of precipitating marine cumulus convection using large-eddy-simulation experiments with zonal forward and backward shear and without shear. One set of simulations includes evaporation of precipitation, promoting for cold-pool development, and another set inhibits evaporation of precipitation and thus cold-pool formation. Without (or with only weak) subcloud-layer shear, conditions are unfavourable for convective deepening, as clouds remain stationary relative to their subcloud-layer roots so that precipitative downdrafts interfere with emerging updrafts. Under subcloud-layer forward shear, where the wind strengthens with height (a condition that is commonly found in the trades), clouds move at greater speed than their roots, and precipitation falls downwind away from emerging updrafts. Forward shear in the subcloud layer appears to promote the development of stronger subcloud circulations, with greater divergence in the cold-pool area downwind of the original cell and larger convergence and stronger uplift at the gust front boundary. As clouds shear forward, a larger fraction of precipitation falls outside of clouds, leading to more moistening within the cold pool (gust front).

3.1   Introduction

Triggered by the World Climate Research Programme's grand challenge on clouds, circulation and climate sensitivity (Bony et al., 2015), tremendous research efforts have been undertaken in recent years to study maritime shallow clouds, with an increasing interest in their organisation. A culmination was the EUREC[4]A field campaign in 2020 (Stevens et al., 2021), which also motivated the successful classification of trade-wind cloud patterns by their visual appearance from space into classes called fish, flower, sugar and gravel (Stevens et al., 2019). This classification indicates that the dominant pattern of trade-wind convection is not the unorganised, non-precipitating cumulus humilis cloud (sugar) but rather the somewhat deeper, precipitating congestus (gravel) that may have a stratiform outflow (flower) at greater heights (Schulz et al., 2021). This finding motivates us to shed more light specifically on cumulus congestus clouds from large-eddy simulations (LES) using a set-up that differs from the traditional BOMEX and ATEX cases that have been intensely used in the past decades (Nuijens & Siebesma, 2019).

Surface wind speed (and to lesser extent wind shear) is considered as one of the predictors of the aforementioned cloud patterns (Bony et al., 2020; Schulz et al., 2021). Helfer et al. (2020) (Chapter 2 of this thesis; hereafter: HNRS20) ran idealised large-eddy simulations (LES) to investigate the effect of wind shear on trade-wind cumulus convection, differentiating between backward shear (BS), where surface winds weaken with height, and forward shear (FS), where surface winds strengthen with height. Indicative of their representativeness of the trades, these simulations are dominated by clouds that resemble gravel, which sometimes have stratiform outflows near clouds tops that resemble flowers. A main result in HNRS20 is that any absolute amount of wind shear limits the strength of cloud updrafts because of a stronger downward-oriented pressure perturbation force (as found in studies of deep convection, e.g. Peters et al., 2019). As a consequence, cloud deepening is hampered in the presence of shear. However, under FS, convection appears to have a tendency to grow deeper, which seems related to this system's enhanced potential to aggregate column moisture on mesoscales. Another noteworthy observation of HNRS20 is that wind anomalies within cold pools depend on the direction of the shear. This may hint at a possible role of downdrafts introducing different cloud-layer momentum in the surface and subcloud layers. In modelling studies of deep convective cold pools, convective momentum transport (CMT) has been found to significantly influence cold-pool winds (Mahoney et al., 2009; Grant et al., 2020). HNRS20 speculated about the role of wind shear in the triggering of new convection at cold-pool edges.

It has long been known that cold-pool edges can trigger secondary convection (e.g. Zipser, 1969; Warner et al., 1979; Intrieri et al., 1990; Weckwerth & Wakimoto, 1992) for which several (not necessarily mutually exclusive) mechanisms are being discussed in the literature. A purely thermodynamic mechanism involves enhanced moisture and thus buoyancy at the edges of cold pools, favouring convection (Tompkins, 2001; Seifert & Heus, 2013; Romps & Jeevanjee, 2016). Using a cloud-resolving model, Tompkins (2001) showed that during the development of deep convective cold pools, evaporation of precipitation cools and moistens the boundary layer. The cold pool's gust front is consequently moister than the cold-pool centre. The lowered temperature can quickly recover, which removes nearly all convective inhibition (CIN) and allows new convection to develop in response to minimal lifting. In the reduced entrainment 'near environment' hypothesis (Böing et al.,

2012; Schlemmer & Hohenegger, 2014), the interplay of moisture aggregation at cold–pool edges (as opposed to depletion of moisture inside cold pools) and vertical uplift at the leading edge of the cold pool's gravity current promotes the formation of wider, and thus deeper clouds less affected by entrainment. Gaining ground in recent literature is the dynamical or mechanical mechanism, whereby the leading edge of the cold pool's spreading gravity current is associated with a band of horizontal convergence in the wind field, which triggers uplift (Xue et al., 2008; Böing et al., 2012; Li et al., 2014; Torri et al., 2015; Meyer & Haerter, 2020). As moist near–surface air is lifted to higher levels above the level of free convection (LFC), it can moisten the upper boundary layer and lower troposphere, and trigger new convective events. This forced uplift may be enhanced by the collision of two or more cold–pool fronts (e.g. Feng et al., 2015; Meyer & Haerter, 2020).

In their LES study of a specific RICO day, Li et al. (2014) found little evidence that supports a thermodynamic mechanism for shallow convection. Inspired by studies on mid–latitude squall lines (Rotunno et al., 1988; Weisman & Rotunno, 2004), they pointed out a possible role of wind shear in the tilting of updrafts and clouds, which decides whether precipitation can fall into pre–existing cold pools and possibly strengthen them. In their simulations, the vorticity of the cold–pool boundary is weaker than that of the ambient wind profile, and the updraft thus tilts away from the cold pool, gaining access to converged moisture at the cold–pool boundary, which is advantageous for convective development. Hence, it seems plausible that this process could help explain the cloud–top–height differences between FS and BS that were reported in HNRS20. A recent study by Mulholland et al. (2021) focusing on squall–line deep convection also notes that forced uplift is larger under stronger subcloud–layer shear as it helps larger mass fluxes and deeper clouds.

In our present study, we aim to address why cloud deepening may be inhibited more under BS than under FS in the presence and absence of cold pools. We describe the morphology of shallow convective systems under shear in idealised large–domain LES with and without the evaporation of precipitation. By turning off evaporation, we limit the formation of cold pools and thus the organization of convection in arc–shaped bands surrounding cold pools. We utilised a computational domain of 50×50 km^2, which is sufficiently large for cold–pool organisation (Seifert & Heus, 2013).

The remainder of this paper is structured as follows. In the following section, we shortly review the simulation set–up as well as the additional simulations we ran for the present paper. We then present the results in a twofold manner. First, we discuss the effects of wind shear on cold pools and the triggering of new convection at their fronts. Second, we ask how clouds behave under wind shear before cold pools emerge, by analysing simulations in which cold–pool formation is suppressed. Finally, we discuss and summarise our findings in a concluding section.

3.2 Experimental design

We utilised the same experimental set–up as in HNRS20 and only point out its most important aspects here. Using version 4.2 of the Dutch Atmospheric Large–Eddy Simulation model (DALES; Heus et al., 2010), we simulated an idealised shallow cumulus case, typical of the North Atlantic trades (Fig. 3.1). Our domain has a size of $50.4 \times 50.4 \times 17.9$ km^3,
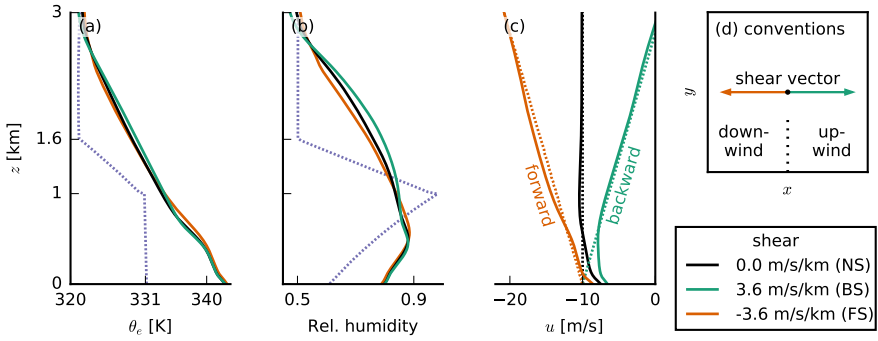
Figure 3.1: (a–c) Profiles of (a) equivalent potential temperature θ_e, (b) relative humidity and (c) the zonal wind components u. Dotted lines are initial profiles and solid lines indicate profiles that are averaged over the last 10 hours of the STD simulations. Orange stands for forward shear (FS), black for no shear (NS), green for backward shear (BS) and purple profiles are the same in all simulations. This colour coding is the same for all other figures. (d) Schematic of the directional conventions used in this paper: downwind is in the negative x-direction, upwind in the positive x-direction.

with a grid spacing of 100 m in the horizontal and a non–uniform vertical grid (stretched from 10 m at the surface to 190 m at the top). Simulations were run for 48 h, to allow for the development of sufficient precipitation. Advection was computed by a 5th–order scheme in the horizontal and a 2nd-order scheme in the vertical, and a Galilean transform was performed to reduce advective errors. We deployed a single–moment microphysics scheme that includes ice and allows for precipitation (Grabowski, 1998; Böing et al., 2012). The model uses an isotropic eddy–diffusivity approach to parametrise subgrid turbulence.

For the sensible and latent surface heat fluxes, we prescribed $SHF = 15.3$ W m^{-2} and $LHF = 225.2$ W m^{-2}, respectively. These values allow for the development of the cloud species that we are interested in: cumulus congestus, which are somewhat deeper than shallow cumuli. The use of constant fluxes removes interactions between cold pools and surface fluxes, including those that could enhance or inhibit thermodynamic mechanisms of triggering convection. While over land interactive surface enthalpy fluxes are crucial for cold–pool modelling, Gentine et al. (2016) suggested that over oceans they only matter for cold pools of scales much larger than our domain. The surface momentum flux was computed interactively by the model, which implies that simulations that develop stronger surface winds (e.g. under FS) also develop larger surface friction. Interactions between the density current and surface friction may matter for setting the scales of cold pools and organisation (Stephan, 2021), but are not explored here. We applied a constant radiative cooling rate of -2.5 K/d to the liquid water potential temperature θ_l. Large–scale subsidence was calculated interactively, using a weak–temperature–gradient approach (WTG; Daleu et al., 2012). The total water specific humidity q_t was nudged towards its initial profile above 4 km with a time scale of 6 h to avoid spurious moisture tendencies.

To investigate the dependence of shallow convection and cold pools on vertical wind shear, we ran experiments with different wind profiles (Fig. 3.1c). As discussed by HNRS20, backward shear, where surface easterlies weaken with height and turn wester–
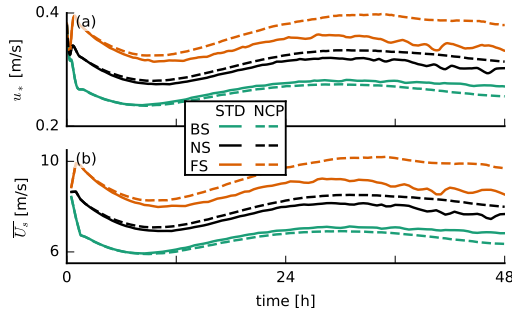
Figure 3.2: Time series of (a) the surface friction velocity u_* and (b) the domain–averaged total wind speed at 5 m height U_s. As explained in Fig. 3.1, orange indicates forward shear (FS), black no shear (NS) and green backward shear (BS), while solid lines indicate the standard (STD) runs and dashed lines the no–cold–pool (NCP) runs. The line colours and types are the same in all following figures, unless indicated otherwise.

lies eventually, is by far the most common in the North Atlantic trades. However, forward shear, where surface easterlies strengthen with height, occasionally occurs as well, in particular in July and August. The analysis of HNRS20 revealed distinct differences in the effect that shear has on convection when it is forward as opposed to backward. The authors further showed that the strength of shear does not play a major role. Hence, we here investigated three different zonal wind profiles with either no shear (NS, black line in Fig. 3.1c), backward shear (BS, green, $\partial_z u = 3.6 \times 10^{-3}$ s^{-1}) or forward shear (FS, orange, $\partial_z u = -3.6 \times 10^{-3}$ s^{-1}). (Note that our BS and FS cases correspond to the BS-4X and FS-4X cases of HNRS20, respectively.) These wind profiles were used as both the initial profiles and the geostrophic forcing. We did not prescribe any meridional wind ($v = 0$). In the calculation of the Coriolis acceleration, we take a latitude of 15° N.

It is important to realise that the wind profiles that develop during the course of the simulation differ from the initial profiles and the geostrophic forcing. After the initialisation of the simulation, the winds evolve to reach an equilibrium after about 24 h and stay approximately constant thereafter (Fig. 3.2). Figure 3.1 shows the profiles from the end of the simulation with solid lines and the initial profiles with dotted lines. This reveals that in the subcloud layer, forward shear occurs even in the BS case, which is also a common feature of the trades (e.g. Holland & Rasmusson, 1973). The presence of forward shear in the subcloud layer is important throughout this paper.

In addition to one set of standard runs with each of the three wind profiles (labelled STD), we performed another set of experiments in which we suppressed the formation of cold pools (labelled NCP, no cold pools). To this end, we turned off the evaporation of precipitation in the LES, which Böing et al. (2012) showed to be very effective. All precipitation in these simulations reaches the surface, and no latent cooling due to the evaporation of rain occurs, which is a crucial ingredient for the formation of cold pools (e.g. Khairoutdinov & Randall, 2006).
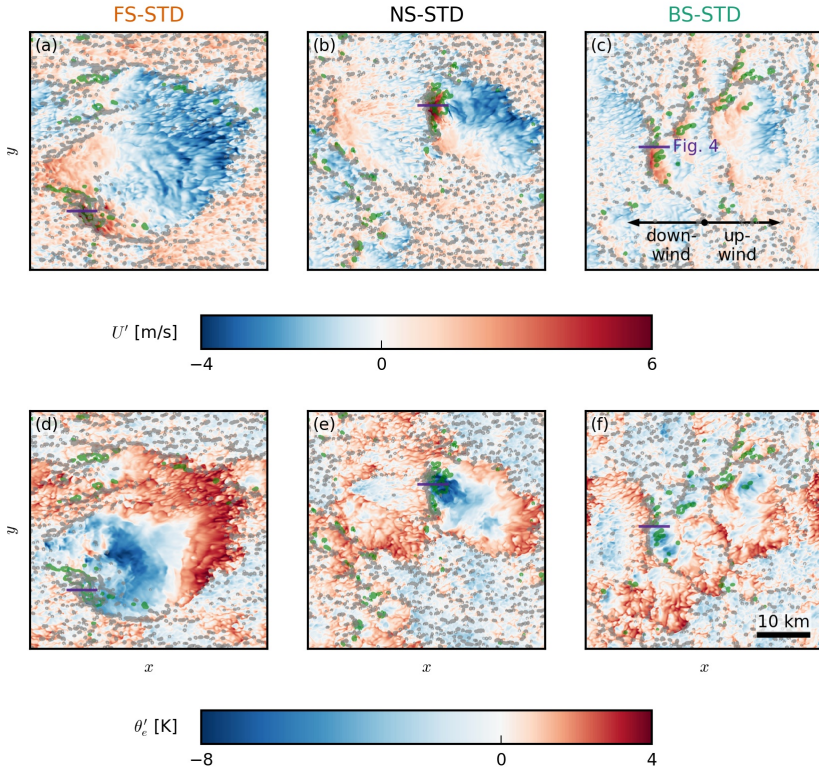
Figure 3.3: Snapshots of the LES domains during exemplary cold-pool events in the (a, d) FS-STD, (b, e) NS-STD and (c, f) BS-STD case. The colourmaps in the x-y cross section show (a–c) total wind speed deviations U' and (d–f) equivalent potential temperature deviations θ'_e (both from the slab average) at the lowest model level (5 m). The grey outlines indicate strong updrafts in the subcloud layer ($w = 1$ m/s at 400 m), and the green outlines indicate surface precipitation ($q_r > 0$). The snapshots were taken around 40 h. The cross sections of Fig. 3.4 are marked in purple.

3.3   Cold pools under shear

3.3.1   Cold-pool structure and behaviour

All our standard simulations (STD) are characterised by the gravel type of organisation including cold pools (Fig. 3.3). In Fig. 3.3, we present top-down views of the computational domain, showcasing the different structure of cold pools in our three shear cases. In these snapshots, the mean wind ($\sim u$) blows from right to left (east to west), and hence, the left is referred to as downwind, the right as upwind (see also Fig. 3.1d) and north would be at the top.

Cold-pool formation starts with the precipitative downdraft (rain shaft) of a deep-enough cloud. Near the surface, the cold and dense air mass spreads out laterally as a gravity current, which is reflected by the diverging wind patterns shown in Fig. 3.3a–c.

In those snapshots, red areas have (total) wind speeds faster than the slab average and are most prominently found at the downwind front of the cold pool, where the gust front adds up to the mean wind speed. Conversely, on the upwind side of the cold pools, the cold-pool front moves against the mean wind, leading to slower total wind speeds (shown in blue).

The cold pools have a characteristic thermodynamic signature (Fig. 3.3d–f). Very low values of equivalent potential temperature θ_e (which combines information about the temperature and the relative humidity) are found in the centre of the cold pool, indicating that the air mass has its origin at higher altitudes where the air is cold and dry (see Fig. 3.1). The outermost edges of the cold pool, especially on the upwind edge, have high values of equivalent potential temperature, which indicates the presence of moist air. Because the surface fluxes are held fixed, the spatial differences in temperature and humidity may be more persistent than in nature. While in the NS and FS cases, cold pools of significant size and strength occur (like the ones in Fig. 3.3a and b), they are much smaller in the BS case (Fig. 3.3c). As we will later elaborate, they also occur more rarely in the BS and the FS cases.

Similar to what observations show, our cold pools are usually not symmetric in their appearance. Visual inspection of a large number of scenes from our simulations shows that new convection (strong subcloud-layer updrafts indicated in grey in Fig. 3.3) is preferably triggered at the downwind edge of the cold pools (i.e. on the left in the panels of Fig. 3.3), where strong winds and presumably large horizontal convergence lead to mechanical uplift (Mulholland et al., 2021).

We further investigate the vertical cloud and boundary-layer structure accompanying the exemplary cold pools from Fig. 3.3 by presenting vertical x-z cross section (Fig. 3.4). In each panel in Fig. 3.4, a strong precipitative downdraft is located near the right edge of the excerpt, but note that in the FS and BS cases, precipitation is or has already ceased there (see Fig. 3.4a, e, i). Focusing on the NS-STD case (middle row), the cold pool itself is visible as a low-temperature tongue (in terms of equivalent potential temperature θ_e) extending from the right edge of the snapshot to nearly the $x = 1$ km mark (Fig. 3.4f). Ahead of this cold pool (downwind), updrafts and new clouds (secondary convection) are developing near cloud base (Fig. 3.4e). Similar signatures of w and θ_e can be seen in the FS and BS cases. An important ingredient in the triggering of new convection by cold pools is the convergence that occurs at its downwind gust front (see Fig. 3.3a–c). Horizontal convergence, $C_h = -\partial_x u - \partial_y v$, between the front and the ambient wind is largest near $x = 1 \ldots 2$ km in Fig. 3.4c, g, k, where vertical uplift is also strong (Fig 3.4a, e, i). In the FS and NS cases, there is also greater zonal wind shear in the density current (upwind tilting of the cold pool boundary) as reflected by positive values of the meridional vorticity, defined as: $\omega_y = \partial_z u - \partial_x w$ (Fig 3.4d, h, l). In the mean or ambient wind, the subcloud-layer vorticity is instead negative (left edge of Fig. 3.4d, h, l), as winds tend to increase with height away from the surface where they experience the strongest friction. In the FS and NS cases, the density current is apparently much stronger (compared to the BS case).
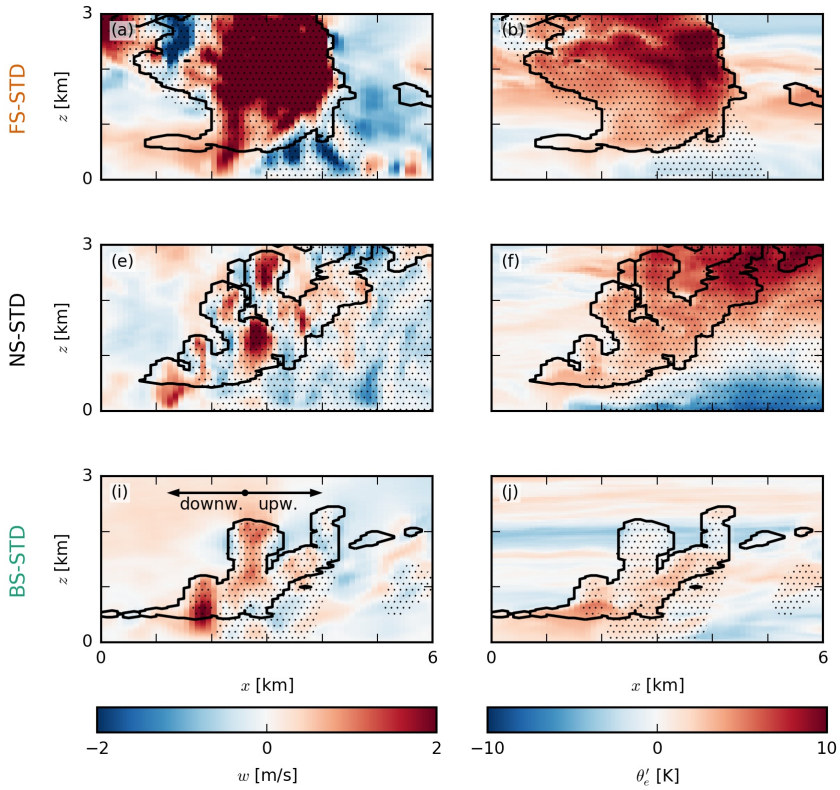
Figure 3.4: Snapshots of exemplary cold-pool fronts in the (a–d) FS-STD, (e–h) NS-STD and (i–l) BS-STD cases. The colourmaps in the x-z slices show (left column) the vertical velocity w and (right column) the equivalent potential temperature anomaly θ'_e. In each panel, the black outlines indicate clouds (i.e. the $q_l = 0$ isoline), the dotted areas indicate precipitation. The location of each snapshot is marked in purple in Fig. 3.3. Each panel is 6 km wide and averaged over 1 km in the meridional direction.

3.3.2   Convergence, vorticity and uplift at cold-pool fronts

The above figures are merely some exemplary snapshots, but we may analyse probability density functions (PDFs) of the entire domain at specific heights to support these impressions (Fig. 3.5). In addition, we construct composite profiles conditioned on all cold-pool gust fronts as well as the ambient environment (Fig. 3.6). To this end, we classify columns as belonging to a cold pool if $\theta'_e < -2$ K at the lowest model level (where the prime indicates anomalies with respect to the slab average). The equivalent potential temperature is a commonly used quantity to identify cold pools (e.g. Zuidema et al., 2012; Schlemmer & Hohenegger, 2014). From this sample, we can identify the downwind gust front through positive anomalies of the total wind speed U' (see Fig. 3.3a–c). We focus on the period from 24 h to 36 h when convection is still shallow and cold-pool fractions are small. Note
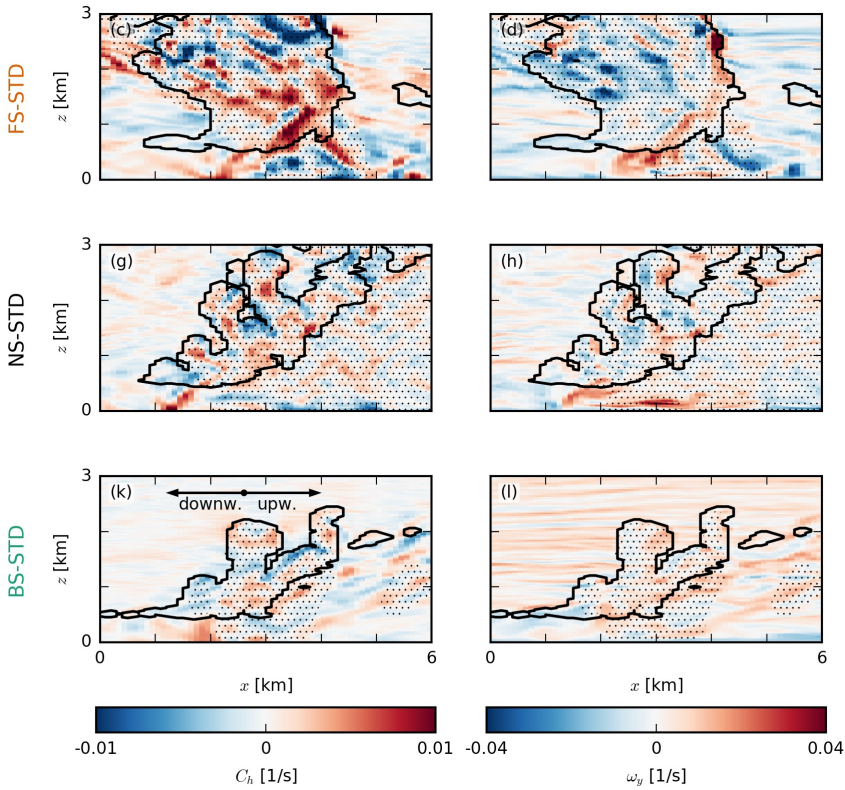
Figure 3.4: (continued) The colourmaps in the x–z slices show (left column) the horizontal convergence C_h and (right column) the meridional component of the vorticity ω_y.

that with our sampling approach it is not possible to capture profiles of convergence and updrafts at the gust front because they are located outside the cold pool (see Fig. 3.4).

In the PDFs in Fig. 3.5, we find indications of more vigorous cold–pool gust fronts in the FS and NS cases. The figure shows a similar frequency of negative anomalies of θ_e in all STD cases (Fig. 3.5a) but more frequent large values of horizontal convergence and divergence in the FS and NS cases (Fig. 3.5b). These can be attributed to larger wind–speed anomalies (Fig. 3.5f). The FS and NS cases also have stronger subcloud–layer updrafts (Fig. 3.5c), which is in line with a more idealised study of deep convective cold pools by Mulholland et al. (2021) who showed that low-level (forward) shear, which is pronounced in our FS and NS cases, leads to stronger, deeper and wider squall–line updrafts as well as an increased mass flux.

Li et al. (2014) pointed out that the vorticity contrast between the cold–pool front and the ambient wind profile sets the tilt of forced updrafts and therefore the degree to which they may tap into existing moist air in the cold pool front or in already moistened cloud air above the mixed layer and near cloud base (see their Fig. 15). With a more pronounced negative vorticity in the ambient wind (Fig. 3.5e), the updrafts are slanted forward more
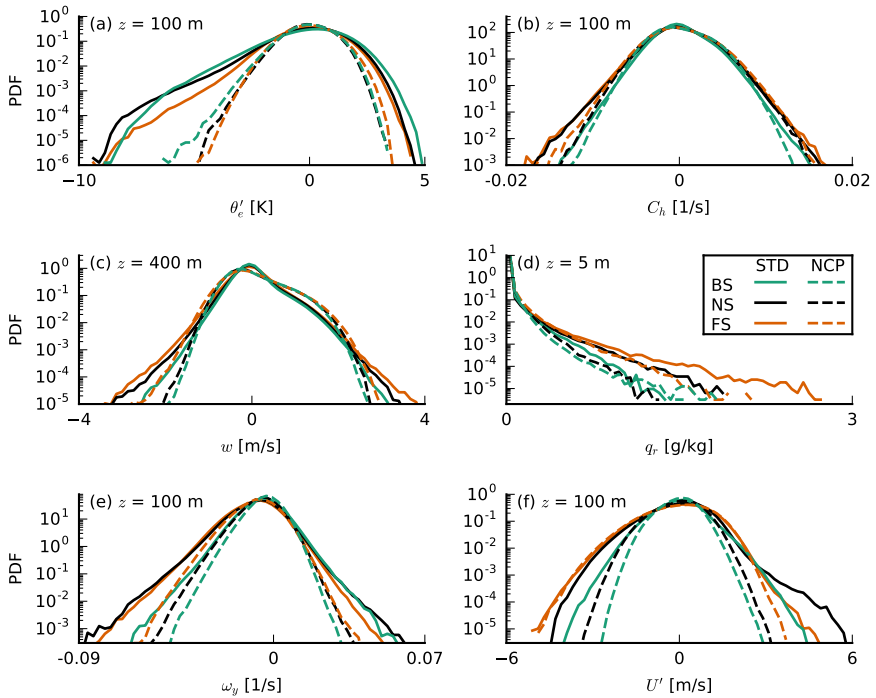
Figure 3.5: Probability density functions (PDFs) of (a) the equivalent potential temperature anomaly θ'_e at 100 m, (b) the horizontal convergence C_h at 100 m, (c) the vertical velocity w at 400 m, (d) the rain water specific humidity q_r at 5 m, (e) the meridional vorticity component ω_y at 100 m and (f) the zonal wind velocity anomaly u' at 100 m, all averaged over Hours 24–36 of each simulation.

in the FS and NS cases than in the BS case, where the gust front has zero vorticity over a much deeper layer (Fig. 3.6b). It is therefore unclear how a vorticity argument alone (as in the original RKW theory; Thorpe et al., 1982; Rotunno et al., 1988; Weisman & Rotunno, 2004) would lead to stronger updrafts in the FS and NS case, because slanted updrafts are generally subjected to a stronger downward-oriented pressure gradient force than updrafts that are upright. The FS case has a higher equivalent potential temperature in both the environment and the gust front (Fig. 3.6c), due to larger absolute humidity (not shown), which may result from more evaporated precipitation during Hours 12–24 of the simulation (see Fig. 3.7e), as in the FS case a larger fraction of rain falls outside of clouds (discussed in Section 3.4). The extra humidity would aid cloud development, but one can also imagine such differences to be quickly diminished in the presence of surface-flux feedbacks (absent in our simulations).

The largest difference in the cold-pool structure among our shear cases appears to be in the near-surface wind speed. Figure 3.5f shows that the FS case, followed by the NS case, has larger negative and positive wind-speed anomalies. This is not only true for the STD runs with cold pools, but also in the NCP runs where no gust fronts develop. Along with the stronger updrafts and downdrafts (Fig. 3.5c), this implies that the FS case has

Figure 3.6: Composite profiles of (a) total wind speed U, (b) meridional vorticity ω_y and (c) equivalent potential temperature θ_e sampled over cold-pool gust fronts ($\theta'_e < -2$ K and $U' > 0$ at the lowest model level; dotted lines) and the environment ($\theta'_e > -2$ K), all averaged over Hours 24–36 of the STD simulations.

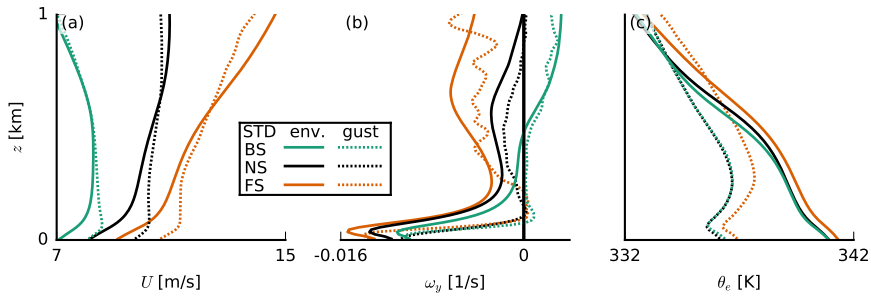stronger circulations (see also HNRS20). CMT might play a role here. In the presence of shear, vertical (convective) transport of momentum can introduce larger wind–speed anomalies. Under FS, updrafts will carry slow surface winds, introducing convergence in a narrow updraft region through the depth of the mixed layer, while downdrafts (which are displaced downwind from the updrafts under FS, as discussed below in Section 3.4) introduce faster winds and broad regions of divergence in the raining areas. The downward transport of larger momentum may be even more pronounced in the presence of rain evaporation, as suggested in studies of deep convection (Mahoney et al., 2009; Grant et al., 2020). CMT can help sustain or even strengthen the cold–pool circulations under FS. Under BS instead, the updrafts and downdrafts are not separated in space (Section 3.4), nor are the wind–speed anomalies introduced by transport very different.

Because our simulations were run with constant and homogenous surface fluxes, differences in forced uplift we observe (Fig. 3.5c) are not caused by thermodynamic fluxes, e.g. the mechanism proposed by Tompkins (2001). The only difference being wind shear, it thus appears likely that the underlying cause of stronger uplift in the FS and NS cases (as compared to BS) lies in the process of momentum transport.

As discussed in HNRS20, moisture aggregation and precipitation in our simulations differ between the shear cases. In the time series in Fig. 3.7, we show the cold–pool fraction, defined as the area fraction where $\theta'_e < -2$ K on the lowest model level; the average and maximum cloud-top height (CTH); deviations of moist static energy from the domain mean within the moistest and driest quartiles (in terms of total water path) of blocks of 12.6×12.6 km^2 compared to the domain mean (as a measure for moisture aggregations; see Bretherton & Blossey, 2017); the domain–mean surface precipitation and the cloud cover. Even on the first simulation day, around 16 h, the FS case begins to aggregate moisture (Fig. 3.7d) and develop deeper clouds (Fig. 3.7b, c), which rain more (Fig. 3.7e) and form cold pools (Fig. 3.7a). This advantage of the FS case underlines that subcloud–layer forward shear seems to favour stronger circulations, more divergence in the cold pool and more convergence and forced uplift at the outflow boundary.

The BS case instead seems to be at a disadvantage in the sense that it develops no deep clouds and significantly less cold pools (Fig. 3.7a–c). In the following section we
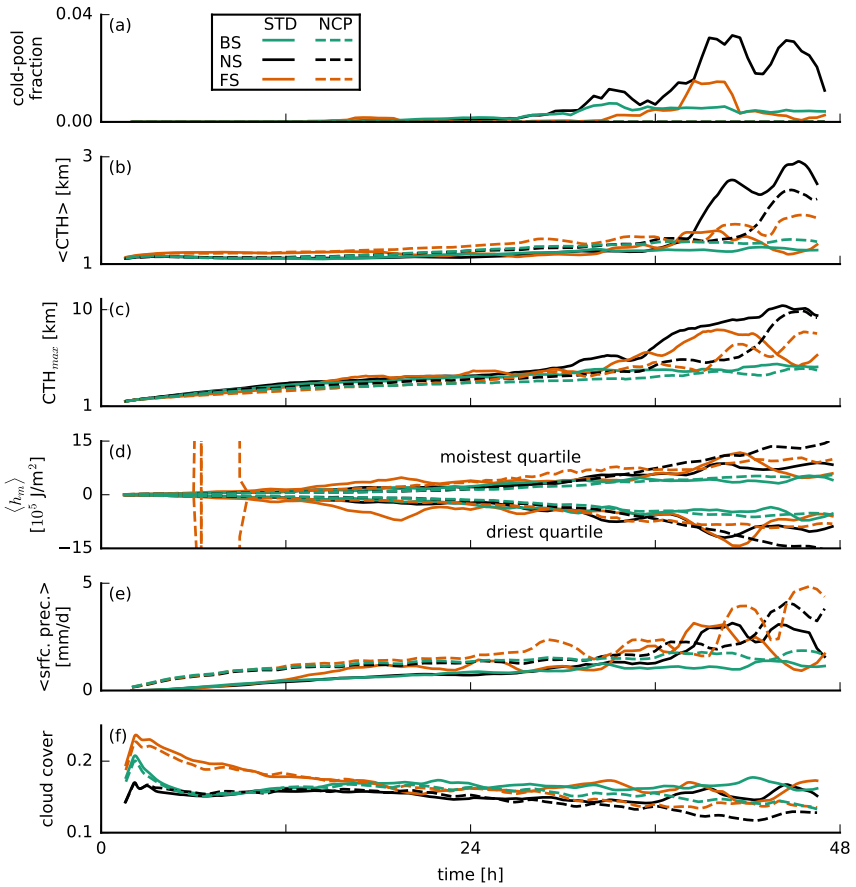
Figure 3.7: Time series of (a) the area fraction of cold pools ($\theta'_e < -2$ K) at the lowest model level, (b) average and (c) maximum cloud top height (CTH), (d) vertically integrated (up to 1 km) moist static energy anomalies $< h_m >$ in the moistest and driest quartiles of 12.6×12.6 km^2 blocks, (e) surface precipitation and (f) cloud cover. The data are smoothed using a 3-hour running-average filter.

wish to shed more light on this and look more closely at the triggering of convection in simulations in which cold pools are suppressed (NCP).

3.4   Sheared convection without cold pools

3.4.1   System development without evaporation of precipitation

Turning off the evaporation of precipitation (NCP runs) effectively suppresses cold pools (Fig. 3.7a), but moisture aggregation is still a common feature (Fig. 3.7d). Without cold pools, the thermodynamic structure of the simulated atmosphere is significantly different (Fig. 3.8). While the amount of rain in the cloud layer differs only little (Fig. 3.8a), surface
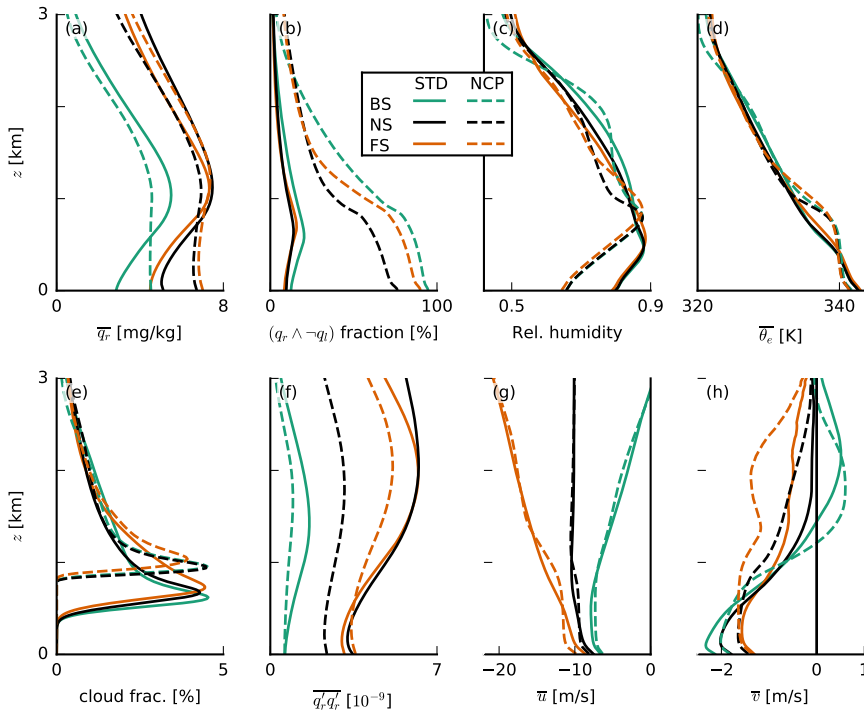
Figure 3.8: Slab–averaged profiles of (a) rain water specific humidity q_r, (b) the ratio of rainy grid points outside of clouds, (c) relative humidity, (d) equivalent potential temperature θ_e, (e) cloud fraction, (f) the variance of q_r, (g) zonal wind velocity u and (h) meridional wind velocity v, all averaged over the last ten hours of each simulation.

precipitation is higher in the NCP runs than in the STD runs (see also Fig. 3.7e) because in the NCP runs all the rain reaches the surface, while in the STD runs, a large fraction evaporates in the subcloud layer (Fig. 3.8a). Consequently, in the NCP runs, more grid points outside of clouds contain rain compared to the STD runs (Fig. 3.8b), while within clouds, the ratio is unchanged (not shown). The lack of rain evaporation in the subcloud layer leads to a decreased relative humidity there (Fig. 3.8c). This is caused by both the lack of transfer of rain water to water vapour and by the lack of evaporative cooling, which results in a warmer subcloud layer (Fig. 3.8d). Furthermore, we observe a higher cloud–base height (Fig. 3.8e) and a deeper mixed layer, for example evident in the temperature, relative–humidity and zonal wind profiles (Fig. 3.8c, d, g), which contributes to the drier boundary layer. Without evaporation of precipitation and thus cold pools, cloud tops are not significantly lower, but convective deepening is delayed by some extent (Fig. 3.7b–c).

3.4.2   Convective structure along the shear vector

Exemplary snapshots of cloud systems from the NCP simulations (Fig. 3.9) suggest that under FS and NS, precipitation is falling downwind from the clouds and downwind from the
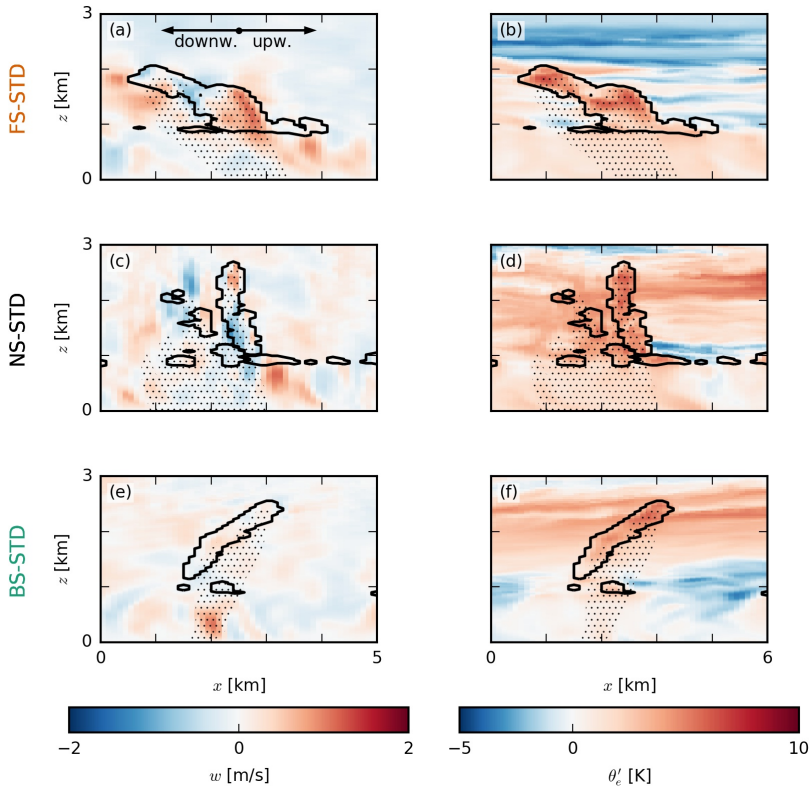
Figure 3.9: Snapshots of exemplary clouds in the (a–b) FS-NCP, (c–d) NS-NCP and (e–f) BS-NCP cases. The colourmaps in the x–z slices show (left column) the vertical velocity w and (right column) the equivalent potential temperature anomaly θ_e. Just as Fig. 3.4, the black outlines indicate clouds (i.e. the $q_l = 0$ isoline), and the dotted areas indicate precipitation. Each panel is 5 km wide, averaged over 1 km in the meridional direction and taken from the late stages of the simulation (around 40 h) to allow for a comparison with Fig. 3.4.

subcloud-layer roots of the clouds, where new updrafts develop. Under BS, precipitation tends to fall near the existing subcloud-layer updraft, which would essentially inhibit the updraft.

We may attempt to quantify where in our shear cases rain shafts are located in relation to the bulk of the clouds and liquid water. To this end, we organise the domain by column-integrated water vapour (CWV), where high CWV corresponds to regions where moisture converges to form (deep) clouds. In some sense, mapping all grid points by CWV allows us to create a cross section through the bulk water vapor and cloud structure, moving from clear sky regions (low CWV) to cloud centers (high CWV). Figure 3.10 shows the distribution of precipitation as a function of height and CWV. The shear cases have somewhat different distributions of CWV, but nonetheless, differences in the distribution of rain are visible. Under NS and even more under FS, the presence of rain in columns
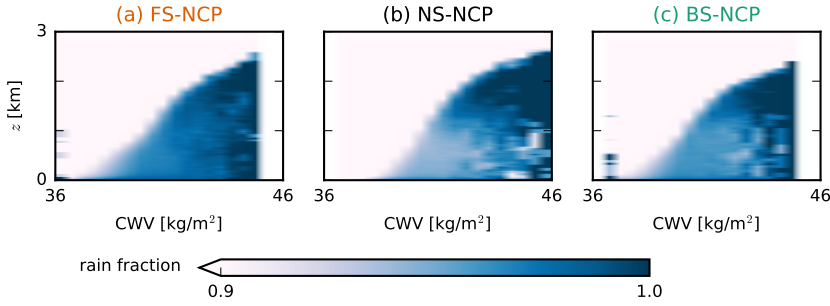
Figure 3.10: Composite profiles of the fraction of rainy grid points ($q_r > 0$) averaged over bins of column–integrated water vapour (CWV). All data are averaged from 30-minute output of the instantaneous 3D fields in the hours 12–18 of the NCP simulations.

with lower CWV is evident, whereas under BS, rain water below clouds is limited to the columns with highest CWV.

The differences in the CWV–binned cloud and rain distributions do not reveal whether rain is located upwind or downwind of clouds. To quantify the precipitation's preferred direction with respect to the clouds, we perform an analysis of the cross–correlation of the cloud-water field with the rain–water field. The cross–correlation is a measure for the similarity of two vectors as a function of shift relative to each other, which is commonly used in signal processing. Occasionally, it is also used in atmospheric science, for example to study coherent structures in the boundary layer (Schmidt & Schumann, 1989; Lohou et al., 2000). Generally, the cross–correlation of two discrete real functions f and g of length N is defined by:

$$X(\Delta) = \sum_{j=0}^{N} f(j)g(j + \Delta),$$
(3.1)

where Δ indicates the displacement (lag) of g with respect to f. We compute the cross–correlation of every row i of the q_l field (at 1 km, i.e. near cloud base) with every other row of the q_r field (averaged over the subcloud layer up to 1 km) and sum up the resulting vectors. Making use of the periodicity of the fields (i.e. $N + i \,\widehat{=}\, i$), this yields a matrix,

$$X(\Delta_i, \Delta_j) = \sum_{i=0}^{N_i} \sum_{j=0}^{N_j} q_l(i, j) q_r(i + \Delta_i, j + \Delta_j),$$
(3.2)

with positive values where similarities between the two fields occur. The 'coordinates' (Δ_i, Δ_j) of the centre of mass of this matrix are assumed to form a good measure of the offset of the precipitation field with respect to the cloud field. The time series of these coordinates in Fig. 3.11 shows a clear signal in the first 24 h of the simulations, especially in the x-coordinate. During this time, there is a negative x-offset of the q_r field with respect to the q_l field in the FS and NS cases of up to 100 m (Fig. 3.11a). A negative offset here means downwind. In the BS case, however, the x-offset is much weaker and of inconsistent sign. Thus, in the FS and NS cases, rain falls downwind of clouds, while in the BS case, precipitation is located under clouds. Shear tilts clouds
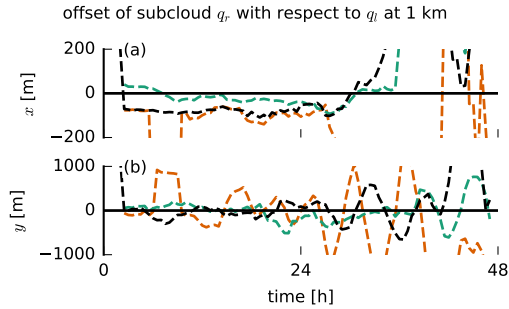
Figure 3.11: Lateral offset in (a) x and (b) y of the rain water specific humidity field averaged over 0–1 km with respect to the liquid water specific humidity field at 1 km. The offset is computed from the centre of mass of the matrix that contains the sum of the cross-correlation vectors of each row of the q_l field with every other row of the q_r field (Eq. 3.2). The analysis is done on 30-minute output of the instantaneous 3D fields. For clarity, we only show the NCP simulations here.

(resulting in a higher projected cloud cover, see Fig. 3.7f), which causes part of the rain to fall out of the sides of the clouds: downwind under FS and upwind under BS (as visible in Fig. 3.9). On the second day, the convection becomes more clustered and less random and the offset signal thus more inconsistent. The y-offset is more incoherent (Fig. 3.11b), suggesting a more random distribution of rain in the meridional direction, but this is not surprising given that the mean wind is in the zonal direction.

The tendency of new updrafts to emerge upwind of existing clouds in the FS and NS cases and then tilt forward (see Fig. 3.9) is because the subcloud layer is characterised by zonal forward shear (Fig. 3.8g). This means that clouds move faster than their roots (subcloud-layer thermals), which literally stay behind and can continue to feed moisture into the cloud layer right behind (upwind) of earlier cells. In the BS case, there is only little shear in the subcloud layer, and the wind speed is similar near the ground and at cloud base. This implies that the roots of thermals move at the same speed as the clouds above, making them more vulnerable to precipitative downdrafts, inhibiting the updraft.

3.5   Discussion and conclusion

In this paper, we used idealised LES experiments with and without cold pools and with different amounts of vertical wind shear, to investigate differences in cloud morphology and the structure of cold pools that develop due to wind shear and that may influence convective development and deepening. We find that shear has an influence on subcloud-layer circulations by separating updrafts from downdrafts, by setting the area and location of rain and rain evaporation, and thus the moistening of the subcloud layer, and by introducing different wind-speed anomalies through CMT, which may strengthen circulations (divergence and convergence) and convective triggering. We summarise our findings in the schematic in Fig. 3.12:

1. In the BS case, precipitative downdrafts are located near or upwind of existing clouds, which is also where new updrafts are located before cold pools are present
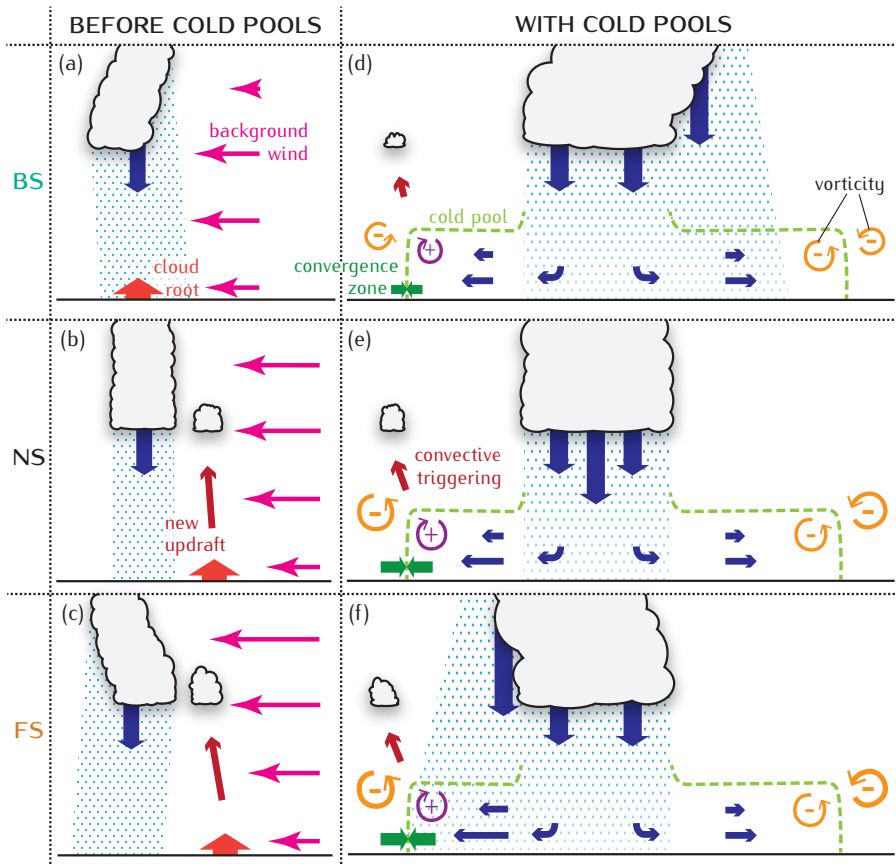
Figure 3.12: Conceptual picture of (a–b) the morphology of unorganised clouds and (c–d) the structure of cold pools in (a, c) the BS case, on the one hand, and (b, d) the FS and NS cases, on the other hand.

(Fig. 3.12a). The precipitation hence hampers new and existing convective cells in their development. In the FS and NS cases, precipitative downdrafts are located downwind, separated from the existing root and new updrafts (Fig. 3.12b, c).

2. Once cold pools are present, new convection is typically triggered downwind at the gust-front outflow boundary, where convergence triggers forced uplift (Fig. 3.12d–f). There is stronger horizontal convergence at the downwind gust front in the FS and NS cases. This facilitates the formation of stronger updrafts in these cases compared to the BS case.

3. In the FS and NS cases, the subcloud-layer is characterised by pronounced forward shear, which implies the presence of negative vorticity, which leads the updrafts to tilt more forward, possibly tapping into moister air ahead of the cold pool (Fig. 3.12e–f).

4. Stronger wind–speed anomalies develop under FS and NS compared to BS, even before cold pools develop and in the complete absence of cold pools. This suggests that CMT facilitates the development of stronger subcloud-layer circulations by introducing stronger winds and thus stronger divergence in the (raining) downdraft area downwind of existing cells, while introducing relatively weaker winds and thus more convergence in the updraft regions.

The mechanisms in the FS and NS cases are overall similar, as indicated in Fig. 3.12, because both cases have subcloud-layer forward shear. However, there are still some differences between them. For example, the FS case has a tendency to develop more column-moisture aggregations and deeper clouds at an earlier point in the simulation because this case has larger wind-speed anomalies and stronger updrafts, indicative of stronger circulations. Furthermore, the FS case has a moister subcloud layer, because of more rain evaporation. Preliminary analysis of simulations run on an even larger domain (150×150 km^2) support our findings here. On this large domain, the FS case develops deep convection with tops > 10 km and a large number of cold pools within half a day, while the BS clouds only reach 10 km after more than 40 h.

After a longer simulation time, the FS case looses its advantage over the NS case, as cold-pool fractions and cloud-top heights are lower. As shown in HSRN2020, this can be attributed to weaker cloud updrafts under FS (and BS) as compared to NS, due to a slanting of the updraft and a stronger downward oriented pressure gradient force. Additionally, precipitative downdrafts get weaker under FS, because they are subjected to more evaporation as they spread out over a larger area due to shear (Fig. 3.12f). Cold pools in the NS case become more vigorous in this stage because precipitation remains concentrated in narrow rain shafts. This is reflected by the significant increase of the variance of q_r (while q_r itself only increases slightly) from the NS–NCP to the NS–STD case (Fig. 3.8a, f), i.e. when convection transforms from more random organisation with precipitation throughout the domain (low variance) to cold pools with narrow strong rain shafts and dry areas surrounding them (high variance). On the other hand, cold pools in the FS case are less vigorous because precipitation is spread out over larger areas, as reflected in the similar variance of q_r in the FS–STD and FS–NCP cases (Fig. 3.8f). Furthermore, rain falling at the same downwind location where cold pools trigger new convection (see Fig. 3.4a) inhibits the FS case. The disadvantage of the BS case is diminished by the relocation of convective triggering to locations upwind instead of downwind once strong precipitative downdrafts lead to the formation of cold pools.

Overall, the cloud morphology is thus most favourable for convective deepening if forward shear is present in the subcloud layer (FS and NS cases) but no forward shear in the cloud layer (NS and BS cases). In the BS case, the low amount of shear in the subcloud layer and the presence of shear in the cloud layer is disadvantageous for cloud deepening, while in the FS case, only the cloud-layer shear forms a disadvantage. The NS case can ultimately develop the deepest clouds and most cold pools because it combines all advantages: forward shear in the subcloud layer and a lack of shear in the cloud layer.

HNRS20 showed that simulations with interactive surface fluxes have a similar response to wind shear as those with constant surface fluxes, and preliminary analysis suggests that this is also the case for the cold-pool characteristics presented here. Furthermore, Gentine et al. (2016) suggest that interactive surface fluxes are only of impor-

tance for cold pools over land and much larger cold pools, but further work on this question is ongoing (e.g. in the framework of EUREC[4]A; Stevens et al., 2021). It should be noted that a potential thermodynamic mechanism of triggering secondary convection (Tompkins, 2001) inherently requires interactive surface fluxes and was thus not investigated here. Exactly because such thermodynamic feedbacks are absent and the only difference is in wind shear, our study provides evidence that the proposed mechanisms of triggering secondary convection through moisture convergence at cold-pool edges (e.g. Böing et al., 2012; Schlemmer & Hohenegger, 2014; Mulholland et al., 2021) and through mechanical uplift (e.g. Li et al., 2014; Meyer & Haerter, 2020) may be facilitated through CMT, which is known to matter for deep convective organization. This underlines the notion that it is not a single mechanism that is responsible for the triggering of secondary convection at cold-pool gust fronts (Torri et al., 2015).

3

DALES is open-source software, which is distributed under the terms of the GNU GPL version 3. The exact version of the code as well as the input files used in this work are available via `https://doi.org/10.5281/zenodo.4668479`.

4

The role of shallow convection
in the momentum budget of the trades

Motivated by the abundance of low clouds in the subtropics, where the easterly trade winds prevail, we study the role of shallow convection in the momentum budget of the trades. To this end, we use ICON-LEM hindcasts run over the North Atlantic for twelve days corresponding to the NARVAL1 (winter) and NARVAL2 (summer) flight campaigns. The simulation protocol consists of several nested domains, and we focus on the inner domains ($\approx 100 \times 100$ km^2) that have been run at resolutions of 150–600 m and are forced by analysis data, thus exhibiting realistic conditions. Combined, the resolved advection and the subgrid stresses decelerate the easterly flow over a frictional layer that balances the prevailing geostrophic wind forcing. Irrespective of the horizontal resolution, this layer is about 2 km deep in the strong winter trades and 1 km in summer, as winds and geostrophic forcing weaken and cloudiness reduces. The unresolved processes are strongest near the surface and are well captured by traditional K-diffusion theory, but convective-scale motions that are not considered in K-diffusion theory contribute the most in the upper part of mixed layer and are strongest just below cloud base. The results point out that convection in the mixed-layer — the roots of trade-wind cumuli and subcloud layer circulations — plays an important role in slowing down easterly flow below cloud base (but little in the cloud layer itself), which helps make the zonal wind jet more distinct. Most of the friction within the clouds and near the wind jet stems from smaller-scale turbulence stresses.

4.1   Introduction

The trade winds are easterly winds that prevail over the tropical and subtropical oceans north and south of the equator. They form the inflow branches of the large-scale Hadley circulation and influence patterns of convergence and tropical rainfall. Furthermore, they modulate turbulent heat fluxes and stresses at the sea surface, and through these sea-surface temperatures and ocean mixing. Therefore, it is important to understand the structure of the trade winds and the processes that influence this structure. One of those processes is shallow convection, which leads to ubiquitous cumulus clouds across the trades and has long been known to play an important role in setting boundary-layer temperature and humidity (Riehl et al., 1951; Malkus, 1958; Tiedtke et al., 1988; Neggers et al., 2007). However, its role in the horizontal momentum budget, such as whether it contributes to mixing slow near-surface momentum upwards (and hence acts as a frictional force), is not well understood.

Earlier works investigating the vertical wind structure in the trades include studies by Riehl et al. (1951) using WWII weather ship data collected in the North Pacific as well as the momentum budget reconstructions using radiosonde arrays from the Barbados Oceanographic and Meteorological Experiment (BOMEX; Holland & Rasmusson, 1973) and the Atlantic Tradewind Experiment (ATEX; Augstein et al., 1974; Brümmer et al., 1974). In these studies, the frictional force arising from Reynolds stresses is derived as a residual from other terms in the momentum budget, e.g. the large-scale advection, pressure-gradient and Coriolis forces. In their reconstruction of the momentum budget during ATEX, Brümmer et al. (1974) in particular pointed out that turbulent stresses do not vanish at the mixed-layer top or base of the cloud layer. They hypothesized that an additional source of stress could stem from convection, which would help explain discrepancies between derived and measured surface-drag coefficients.

A similar point has been made by studies that explain patterns of surface winds over tropical oceans. Traditionally, tropical surface winds have been explained using Rayleigh damping models that take the generalised Ekman balance as a starting point (e.g. Deser, 1993). These models assume a balance between pressure gradients, Coriolis acceleration and friction:

$$f\mathbf{k} \times \overline{\mathbf{u}} + \frac{1}{\rho_0}\nabla\overline{p} = \frac{\partial\tau}{\partial z},\tag{4.1}$$

where the overbar $\overline{\cdot}$ indicates slab averages, f is the Coriolis parameter, $\mathbf{u}$ is the wind vector, ρ_0 is a reference density (that depends on the specific model implementation), p is the pressure and τ is the stress tensor. These models neglect viscosity and model the friction as a linear function of the surface wind speed ($\partial_z\tau = -\eta\mathbf{U}$) that goes to zero at the top of the boundary layer, which in the tropics is typically taken as the subcloud layer. This implies that there is no vertical mixing of momentum at the boundary-layer top that can play a role in setting surface (and boundary) layer winds. However, using a mixed-layer model that includes a bulk parametrisation for entrainment at the top of the boundary layer to estimate boundary-layer winds, Stevens et al. (2002) and Back & Bretherton (2009) demonstrate that the acceleration of near-surface winds by mixing momentum between the boundary layer and the free troposphere is key to explaining the climatology of surface winds in the tropics. The mixed-layer model does not explicitly take into account convective momentum transport (CMT), but a convective mass flux is implicit

in the formulation of an entrainment or exchange flux at the mixed-layer (boundary-layer) top. In another study, Carr & Bretherton (2001) derived CMT as a residual from the large-scale budget of momentum using reanalysis data and found CMT to be larger in the lower troposphere than in the upper troposphere, suggesting that the abundance of shallow convection could lead to a source of shallow CMT that would be important for large-scale circulations. Similarly, Lin et al. (2008) stated that CMT is a factor that damps the low-level trade wind. Using general-circulation-model (GCM) simulations, Richter et al. (2014) suggested that CMT is crucial for explaining the strength and direction of surface winds over the equatorial Atlantic.

In none of these studies, the relative influence of small-scale turbulence versus more coherent thermal plumes associated with convection on the total momentum transport within the boundary layer is specifically analysed. This is the objective of our study, in which we ask: What is the role of shallow convection in the momentum budget of the trades? In our answer, we aim to differentiate between different scales of motion from turbulent to overturning motions. We also address whether moist convection contributes meaningfully to turbulent stresses at the mixed-layer top (approximately cloud base) and whether the profile of the momentum flux within the well-mixed subcloud layer behaves according to the established K-diffusion model. This parametrisation models the momentum flux τ as the product of the mean wind shear $\partial_z \overline{\mathbf{u}}$ and a height-dependent exchange coefficient K, thus assuming that turbulent momentum mixing is isotropic in the horizontal but dependent on the mixing length scale in the vertical (e.g. Holtslag & Boville, 1993; Stevens, 2000). Such K-diffusion models can be extended by a non-local term or even be combined with a mass-flux approach to account for counter-gradient transport and mixing at longer length scales (Soares et al., 2004; Siebesma et al., 2007).

We make use of a unique set of high-resolution simulations run with the ICON large-eddy model in hindcast mode over a domain spanning the entire North Atlantic trades (Stevens et al., 2019). Unlike conventional large-eddy-simulation (LES) cases, these hindcasts are initialized and forced with ECMWF analysis data at the outer domain boundaries, so that smaller inner domains on the order of a few 100×100 km^2 feel a realistically varying large-scale state with air masses moving in at one boundary and moving out at the other — as opposed to the traditionally used periodic boundary conditions. The dataset covers twelve days in both summer and winter with a variety of atmospheric states and cloud regimes, including days with shallow and deeper convection. The inner domains have been run with different resolutions, which allows us to infer the importance of eddies of different scales. The dataset has already offered a wealth of new insights, for example on the diurnal cycle of marine shallow convection (Vial et al., 2019), the shallow-convective mass flux (Vogel et al., 2020), the vertical distribution of lower-tropospheric water vapour (Naumann & Kiemle, 2020) and counter-gradient momentum transport (which we also briefly discuss below; Dixit et al., 2021).

This paper is structured as follows: We first describe the ICON-LEM simulations and our analysis of the momentum budget (Section 4.2). In Section 4.3, we analyse the momentum budget for winter and summer days and look closer at the role of shallow convection versus small-scale turbulence in setting the frictional force, in particular. Section 4.4 discusses the momentum flux and, in particular, how it relates to the K-diffusion model. Finally, we summarise our findings in Section 4.5.
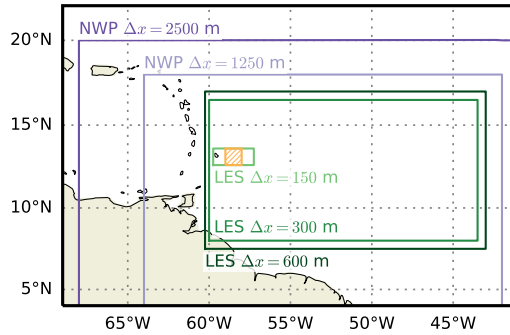
Figure 4.1: Overview of the simulation protocol of Stevens et al. (2019) with two outer domains that use NWP physics (purple) and three inner domains that use LES physics (green). The domains are coupled via a one-way nesting, and the horizontal resolution Δx increases as the domain size decreases. The hatched orange square indicates the area of interest of the present paper.

4.2   Data description

We analysed large-eddy-simulation (LES) hindcasts that were performed on specific days of the Next-Generation Advanced Remote Sensing for Validation (NARVAL) expeditions (Stevens et al., 2019), using the Icosahedral Nonhydrostatic (ICON) model (Zängl et al., 2015) as an LES (ICON-LEM; Dipankar et al., 2015). These simulations cover an extensive part of the tropical North Atlantic (Fig. 4.1). Six days in December 2013 and six days in August 2016 have been simulated (Table 4.1). The simulation protocol consisted of five nested domains that decrease both in size and in horizontal grid spacing from 2500 m to 150 m (Fig. 4.1); the domains were coupled via a one-way nesting. The vertical grid was the same in all domains, and its spacing was stretched from about 30 m at the lowest level to about 300 m at 20 km, implying that in the lower troposphere vertical transport is well resolved. Here, we only consider the three smallest domains, which used LES physics, while the two largest domains used NWP physics (discussed by Klocke et al., 2017). The LES runs had horizontal resolutions of 600, 300 and 150 m. While even 150 m is probably on the coarser end of what is needed to simulate shallow cumuli (e.g. Sato et al., 2018), comparison with satellite imagery shows that the simulations are able to capture many important features of the cloud field (Vial et al., 2019). Besides, one should also value the great size of the simulation domain and the realistic forcing. The runs were initialised at 0900 UTC each day, using data from the larger domains, which in turn were initialised using ECMWF analysis data and forced at the outermost boundaries using three-hourly ECMWF forecasts. The model was then run for 27 hours, whereby the first three hours were disregarded as model spin-up. We emphasise that the modelling approach here is unlike typical idealised LES studies. In particular, there were no periodic boundary conditions, subsidence was not prescribed and the runs were not initialised with laterally homogeneous profiles. Further details can be found in Stevens et al. (2019).

Here, we consider a subset of the smallest simulation domain with an area of $1° \times 1°$ ($\approx 100 \times 100$ km^2), which is similar to a typical GCM grid box. The box is located east of Barbados (58–59° W, 12.6–13.6° N; orange square in Fig. 4.1) and coincides with the

Table 4.1: Overview of the simulated days

Campaign	Research flight	Date
NARVAL1	RF 2	11 Dec. 2013
	RF 3	12 Dec. 2013
	RF 4	14 Dec. 2013
	RF 5	15 Dec. 2013
	RF 6	16 Dec. 2013
	RF 8	20 Dec. 2013
NARVAL2	RF 2	10 Aug. 2016
	RF 3	12 Aug. 2016
	RF 5	17 Aug. 2016
	RF 6	19 Aug. 2016
	RF 7	22 Aug. 2016
	RF 8	24 Aug. 2016

main operational area of the EUREC⁴A field campaign that took place in early 2020 (Stevens et al., 2021).

Within that area, we a posteriori calculated all contributions to the horizontal momentum equation at every grid point of the LES output, which is available every 15 minutes. The LES solves the filtered Boussinesq-approximated momentum equation, which for the horizontal wind components reads (e.g. Stull, 1988):

$$\frac{\partial \tilde{u}_i}{\partial t} = \underbrace{f \varepsilon_{ij3} \tilde{u}_j}_{C} \underbrace{- \frac{1}{\rho} \frac{\partial p}{\partial x_i}}_{P} \underbrace{- \tilde{u}_j \frac{\partial \tilde{u}_i}{\partial x_j}}_{A} \underbrace{- \frac{\partial \tau_{ij}}{\partial x_j}}_{R},$$
(4.2)

where the tildes ˜ indicate the LES-filtered variables, u_i are the horizontal wind components in the x- and y-direction ($i = 1, 2$), f is the Coriolis parameter, ε_{ij3} is the Levi-Civita symbol, ρ is the density, p is the pressure and τ_{ij} is the subgrid stress tensor. (In the following, we drop the tildes for convenience.) The first term on the right-hand side of the equation depicts the Coriolis effect (C), the second the pressure-gradient force (P) and the third the resolved advection (A), which may be decomposed into a horizontal and a vertical component:

$$\underbrace{-u_j \frac{\partial u_i}{\partial x_j}}_{A} = \underbrace{-u \frac{\partial u_i}{\partial x} - v \frac{\partial u_i}{\partial y}}_{A_h} \underbrace{-w \frac{\partial u_i}{\partial z}}_{A_v}.$$
(4.3)

The fifth term of Eq. 4.2 corresponds to stresses introduced on scales smaller than the LES model grid: the subgrid turbulence, calculated using a Smagorinsky turbulence scheme. This term is calculated as a residual R, while output of the subgrid tendencies or fluxes (apart from the surface fluxes) are not available. Note that this approach implies that R may also contain any other errors that may occur in the analysis (e.g. from the re-gridding mentioned below). Furthermore, we remark that due to ICON's triangular grid the exact form of the Navier-Stokes equation solved by the model is slightly different, though the principles discussed before still hold (see Dipankar et al., 2015).
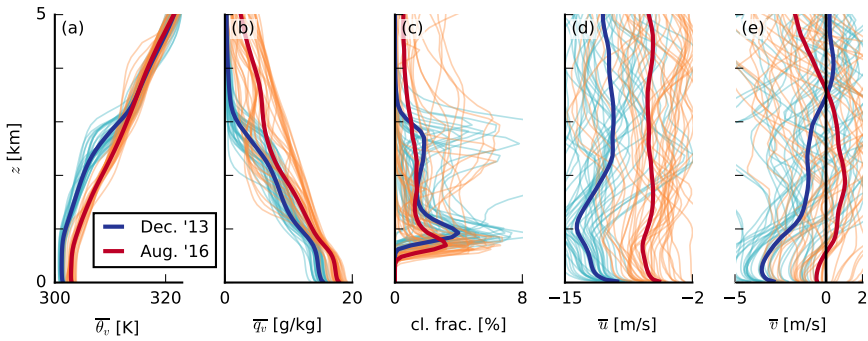
4

Figure 4.2: Slab-averaged profiles of (a) virtual potential temperature θ_v, (b) water vapour specific humidity q_v, (c) cloud fraction, (d) zonal wind velocity u and (e) meridional wind velocity v. The thin lines indicate 2-hour averages and the thick lines indicate averages over all simulated days in December (blue) and August (red).

To calculate the budget terms, the model output was first re-gridded from the model's unstructured grid to a Cartesian grid of similar resolution. Derivatives were computed using second-order central differences. The storage term on the left-hand side of the equation was calculated as the temporal derivative of the outputted wind field. We then spatially averaged each term of Eq. 4.2 on each model level over the whole 1° × 1° area. These spatial averages were consecutively averaged over six two-hour periods (1200–1400 UTC, 1600–1800 UTC and so on until 0800–1000 UTC of the following day) of each of the twelve simulation days. This gave us a reliable statistical basis for our analysis of the mean momentum budget, while keeping the computational demand in check. Furthermore, by analysing the budget throughout the day, we were mindful of the diurnal cycle that is present even over the ocean (Vial et al., 2019). Mesoscale variability that can introduce large hourly variations are beyond the scope of this study.

4.3   The momentum budget

4.3.1   Mean state of winter and summer NARVAL days

The area upstream of Barbados is governed by two distinct seasons: a wet season from about June until November and a dry season throughout the rest of the year (Brueck et al., 2015). These seasons are tied to the location of the inter-tropical convergence zone (ITCZ). In the dry season, the ITCZ is located at lower latitudes, and the area east of Barbados experiences steady trade winds from east to north-east, moderate large-scale subsidence and an inversion at around 800 hPa visible in profiles of both temperature and relative humidity. In contrast to this, in the wet season, the ITCZ is located much closer to Barbados, leading to weaker winds from the east (at times even south-east), moderate upward motion and a less-defined trade inversion.

Figure 4.2 showcases these differences between August (red lines) and December days (blue lines): typical trade-wind conditions with shallow convection in boreal winter and deeper convection in boreal summer. The figure shows two-hour averages as thin
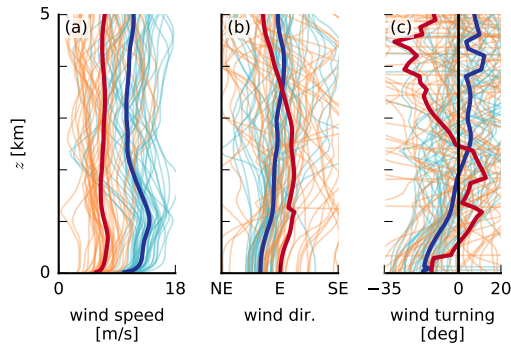
Figure 4.3: Slab-averaged profiles of (a) total wind speed, (b) wind direction and (c) wind turning (with respect to purely geostrophic flow). A negative wind turning angle here means more northerly wind and a positive angle more southerly wind. The line types and colours are the same as in Fig. 4.2.

lines and the mean over all winter days as thick blue lines and all summer days as thick red lines. In December, we have a trade-wind layer with a clear inversion, trade winds from east-north-east at the surface and a cloud fraction profile that always has a maximum just above cloud base and frequently also near the inversion. Such a cloud fraction profile is typical for the winter trades near Barbados where shallow cumuli are often accompanied by a stratiform cloud layer near the trade-wind inversion (Nuijens et al., 2014). On average, the December cloud fraction maximum in our simulations is around 4 per cent, which is also in line with the observations of Nuijens et al. (2014). In August, the boundary layer is somewhat warmer and moister without an inversion, surface winds are much weaker and from the east, and the cloud fraction profile often has one maximum only near cloud base as well as higher cloud tops.

The typical wind profile in the North Atlantic trades is dominated by the zonal component and is characterised by steady easterlies to north-easterlies near the surface, a wind speed-maximum near cloud base and decreasing wind speed further aloft (e.g. Holland & Rasmusson, 1973; Brümmer et al., 1974; Brueck et al., 2015). Figure 4.2d shows that we find most of these features on the simulated days. In particular, the dominance of the zonal component and the wind-speed maximum near cloud base are well captured during winter. An important difference between the wind as calculated from the simulation output and for example the BOMEX wind profiles is the wind above 2.5 km: While in BOMEX the zonal wind velocity continues to decrease with height, i.e. become less negative (Holland & Rasmusson, 1973), the mean zonal wind during NARVAL is approximately constant with height. Such a near-constant wind with height is not typical on individual days, but reflects the large high day-to-day variability in wind shear at those levels.

We define the wind turning angle as the difference between the actual wind direction and the geostrophic wind direction and show it in Fig. 4.3 together with the total wind speed and the wind direction. In winter, the wind turning angle is negative near the surface and decreases to zero throughout a layer of about 1.5 km deep. The negative angle indicates that the actual wind comes from the north-east, rather than from the
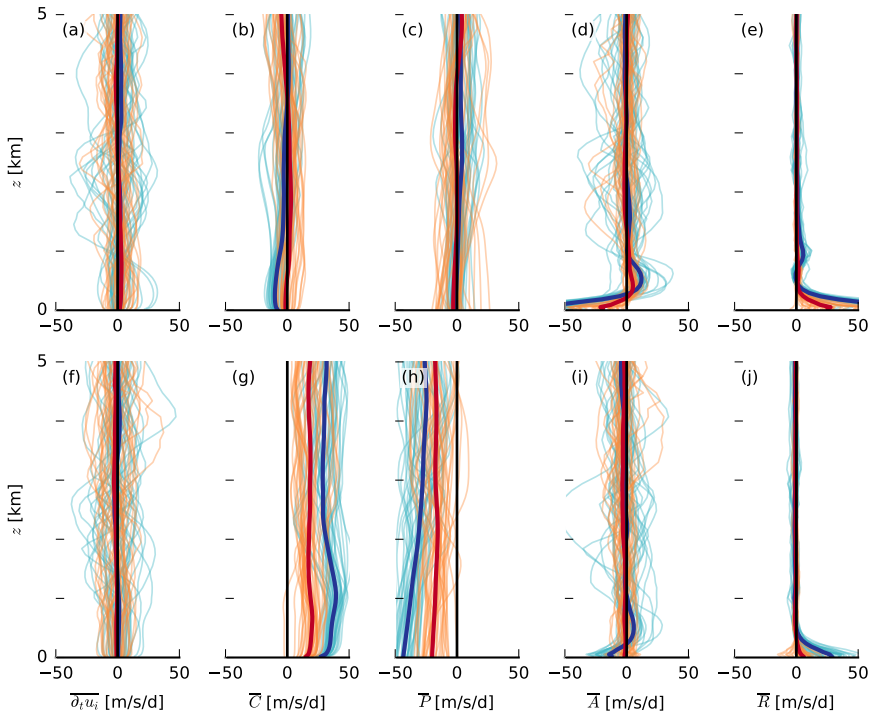
Figure 4.4: Slab–averaged profiles of the terms of the momentum budget (cf. Eq. 4.2) for (a–e) the zonal wind component and (f–j) the meridional component: (a, f) total tendency $\partial_t u_i$, (b, g) Coriolis force C, (c, h) pressure–gradient force P, (d, i) resolved advection A and (e, j) residual R. The line types and colours are the same as in Fig. 4.2.

east, which implies that the wind has turned across isobars towards lower pressure at the equator, as identified in earlier studies of (sub)tropical winds (Brümmer et al., 1974; Stevens et al., 2002). In summer, there is much more variability in the wind turning and an ageostrophic wind component is more common even at higher altitudes. This would be in line with slow momentum from near the surface being transported across a deeper layer in summer due to deeper convection, introducing a so-called 'cumulus friction'. In the next sections, we look closer at the different processes in the momentum budget to identify the role of convection.

4.3.2   Momentum tendencies

First considering the simulations at the highest horizontal resolution of 150 m, the different momentum tendencies as defined in Eq. 4.2 are shown in Fig. 4.4 with the means for winter and summer separately. The top row shows the zonal component and the bottom row the meridional component. All tendencies except for the residual show significant variability in both sign and magnitude in the two-hourly profiles (thin lines in Fig. 4.4). However, on average, the storage term is negligible at all heights. The pressure gradient dominates
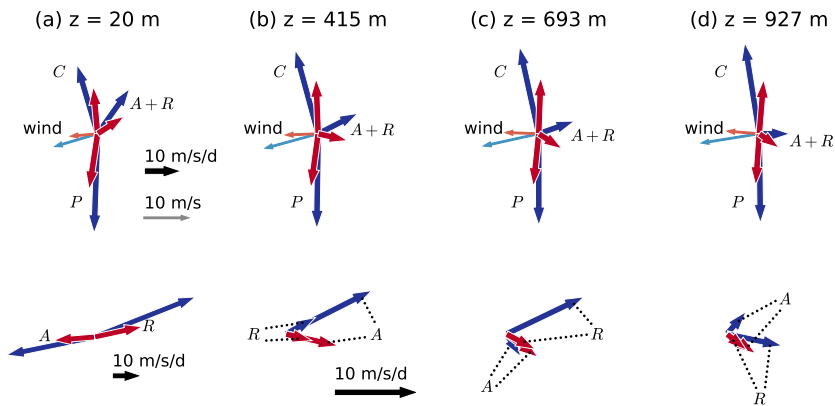
Figure 4.5: Vector representation of the momentum budget averaged over (blue) all December days and (red) all August days (a) near the surface ($\sim$ 20 m), (b) in the mixed layer ($\sim$ 400 m), (c) near cloud base ($\sim$ 700 m) and in the cloud layer ($\sim$ 900 m). The thinner arrows indicate the wind speed and direction at each height level. The length of the arrows indicates the magnitude of the overall average of the respective budget term or the wind speed (thick lines in Figs. 4.3 and 4.4). The scale is the same for the whole top row but different for the panels in the bottom row, as indicated by the black and grey arrows.

in the north–south direction (Fig. 4.4h) and is largely balanced by the Coriolis force (Fig. 4.4g), which leads to the development of predominantly zonal flow. All forces are much weaker in summer than in winter, caused by the weaker pressure–gradient force (Fig. 4.4h, in red) due to the northward wander of the ITCZ.

The resolved advective tendency and the residual tendency (Fig. 4.4d–e, i–j) exhibit large values in the lower 2 km of the atmosphere, whereas above 2 km they are on average negligible. The advective tendency includes all motions on scales equal to and larger than the model grid, whereas the residual tendency is interpreted as subgrid turbulence not resolved by the model grid. These two mostly act in the opposite direction. For instance, the advective tendency is negative close to the surface in both wind components, which indicates an acceleration in the direction of the mean north-easterly wind, whereas the residual tendency is positive, which indicates a deceleration in the direction of the mean wind.

Perhaps the vectors in Fig. 4.5 offer a more intuitive view of these results. The top row shows the direction of the wind, the pressure gradient and Coriolis force, as well as the forcing from the advection and residual tendencies combined, using a vector representation for winter (blue) and summer (red). The vectors are shown at different altitudes: (a) in the surface layer, (b) well into the mixed layer, (c) near cloud base and (d) at the zonal wind jet in the cloud layer. This vector view shows more clearly that the combined vector $A + R$ is not simply opposing the mean surface wind. This implies that it is not merely surface friction that is at play here, but instead mixing across the boundary layer may introduce air masses whose wind is closer to geostrophy, thereby reducing the turning across isobars (Brümmer et al., 1974; Stevens et al., 2002). The bottom panel separates the advective from the residual tendencies, and shows that near the surface, the subgrid
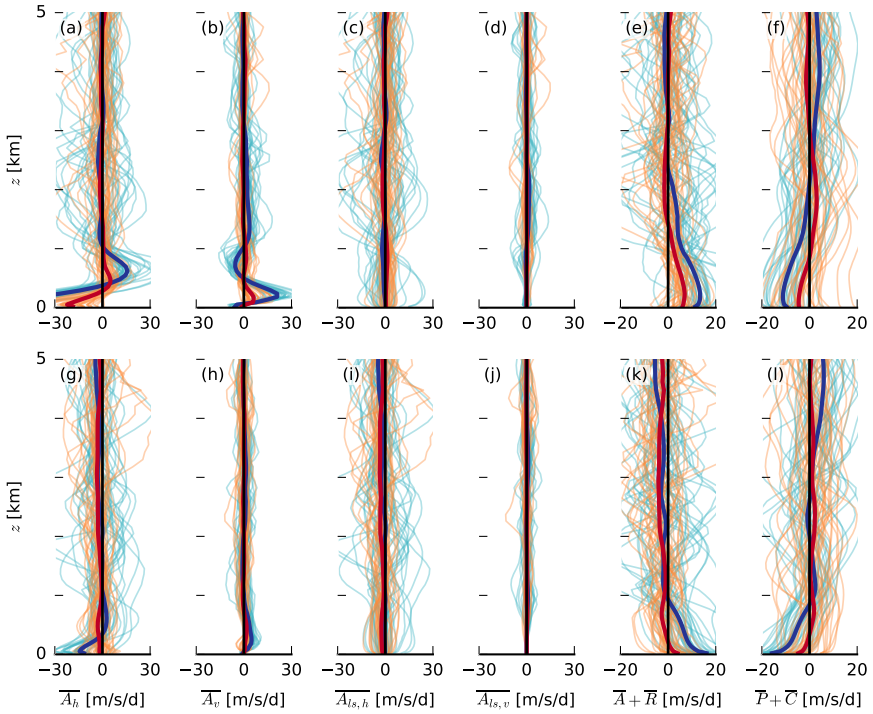
Figure 4.6: Slab–averaged profiles of (a, g) horizontal and (b, h) vertical advection, A_h and A_v, respectively, (c, i) large–scale horizontal and (d, j) large–scale vertical advection, $A_{ls,h}$ and $A_{ls,v}$, respectively, (e, k) the sum of total resolved advection and residual $A + R$ and (f, l) the sum of pressure–gradient and coriolis force $P + C$ for (a–f) the zonal wind component and (g–l) the meridional component. The line types and colours are the same as in Fig. 4.2.

turbulence (R) is as expected directed almost opposite to the mean wind, whereas the resolved flow (A) is aligned with the mean wind. In the mixed layer (400 m) A is instead directed against the mean wind, and maximizes near cloud base (Fig. 4.4d, i). In other words, resolved advection here tends to reduce the easterly wind component. In the lower cloud layer, near the zonal wind jet ($\sim$1 km), the advective tendency is closer to zero, only to become slightly positive in the cloud layer between 1 and 2 km (Fig. 4.4d, i). In the lower cloud layer the subgrid turbulence R is again larger with positive values, but only in winter, presumably because the zonal wind jet and thus shear is more pronounced (Fig. 4.4e, j; Fig. 4.5c,d). Combined, $A + R$ have a considerable magnitude at cloud base, which is at least a third of $A + R$ present near the surface.

The advective tendency includes contributions from resolved horizontal and vertical advection (Eq. 4.3). In Fig. 4.6a–b, g–h, the horizontal and vertical components A_h and A_v of the total advection are shown. The structure of the total advective tendency (Fig. 4.4e) is similar to that of A_h, which acts to accelerate the flow near the surface and slow down the flow in the mixed layer and near cloud base (Fig. 4.6a, g). Vertical advection A_v partially balances these tendencies (Fig. 4.6b, h).

We may ask what the contribution of large-scale wind gradients (both horizontal and vertical) acting on the mean wind is. In absence of an estimate of the large-scale horizontal wind gradient, we may estimate the contribution from 'large scales' by applying a horizontal low-pass filter with a cutoff scale of 10 km to the wind data and then calculating the horizontal advective tendency $A_{ls,h}$ (which is plotted in Fig. 4.6c and i) from this 'smoothed' wind field. Using a Reynolds decomposition of the wind into a mean and a fluctuating part ($u_i = \overline{u}_i + u'_i$), the large-scale zonal advection (e.g. averaged over our area of interest) may be written as:

$$\overline{u\frac{\partial u}{\partial x} + v\frac{\partial u}{\partial y} + w\frac{\partial u}{\partial z}} \approx \overline{u}\frac{\partial \overline{u}}{\partial x} + \overline{v}\frac{\partial \overline{u}}{\partial y} + \overline{w}\frac{\partial \overline{u}}{\partial z} + \overline{u'\frac{\partial u'}{\partial x}} + \overline{v'\frac{\partial u'}{\partial y}} + \overline{w'\frac{\partial u'}{\partial z}} \qquad (4.4)$$

We dropped all cross terms (e.g. $\overline{\overline{u}\partial_x u'} + \overline{u'\partial_x \overline{u}}$), in accordance with Reynolds averaging rules. The first three terms on the right-hand side represent larger-scale advection and the last three terms smaller-scale advection on scales smaller than 10 km. The large-scale vertical advection may be estimated from the product of the domain-mean vertical velocity and the vertical gradient of horizontal wind, which is shown in Fig. 4.6d and j. Neither of the large-scale terms (first three on the right-hand side of Eq. 4.4) have a systematic structure and sign in the lower atmosphere, with large hour-to-hour variations, which on average are close to zero. This implies that horizontal wind fluctuations ($\overline{u'\partial_x u'} + \overline{v'\partial_y u'} + \overline{w'\partial_z u'}$) on scales smaller than 10 km (i.e. convection and turbulence rather than large-scale circulations) dominate the advective tendencies. Note that the choice of 10 km is somewhat arbitrary, and though we have investigated different values as well (not shown), a longer length scale seems hardly justified, given that even advection from scales larger than 10 km is negligible.

As in Fig. 4.5, we may combine the advection and residual into one term ($A + R$, Fig. 4.6d, i) and the same for the pressure-gradient and Coriolis forces ($P + C$, Fig. 4.6e, j). The two terms mirror nicely, which reflects the overall balanced budget (Fig. 4.4a, f). This also more clearly reveals the depth of the frictional layer, which we interpret as the layer where the dominant easterlies are decelerated, which extends up to about 2 km in winter and 1 km during summer. Thinking about the concept of cumulus friction (Schneider & Lindzen, 1976) in studies of deep convection, it appears that there is a friction between 1 and 2 km that is about a third of the value in the well-mixed subcloud layer. This is not surprising because of the strong turbulence associated with the clouds at these altitudes.

4.3.3 Resolved momentum fluxes

Further manipulation of the Reynolds-decomposed advection term (Eq. 4.4) shows that the divergence of the momentum flux represents the influence of turbulent stress on the mean motion (e.g. Stull, 1988):

$$\overline{u_j\frac{\partial u_i}{\partial x_j}} \approx \overline{u}_j\frac{\partial \overline{u}_i}{\partial x_j} + \frac{\partial \overline{u'_i w'}}{\partial z}. \qquad (4.5)$$

Note that while in the previous section (Eq. 4.4), the primes indicated deviations at scales smaller than 10 km, here, they more traditionally indicate deviations from slab averages over the entire 1° × 1° area. To arrive here, the continuity equation multiplied by u'_i was added to Eq. 4.4 and the horizontal momentum flux divergences (e.g. $\partial_x \overline{u'u'} + \partial_y \overline{u'v'}$)
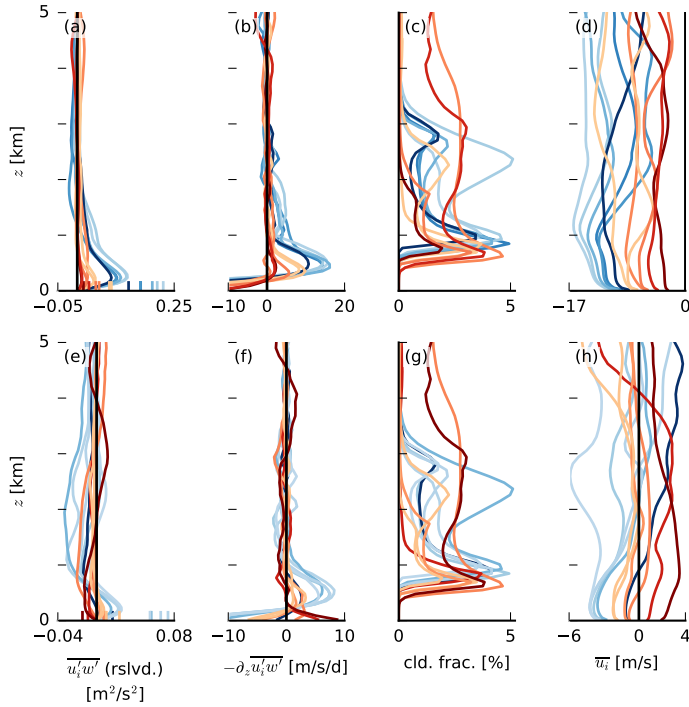
Figure 4.7: Slab–averaged daily profiles of (a, e) the momentum fluxes $u'w'$ and $v'w'$, (b, f) their negative vertical divergence $-\partial_z \overline{u'w'}$ and $-\partial_z \overline{v'w'}$, (c, g) the cloud fraction and (d, h) the zonal and meridional wind velocities. In the top row the lines are coloured by surface zonal wind velocity and in the bottom row by the surface meridional wind velocity, where blue shades indicate winter days and red shades summer days. The coloured tick marks in (a) and (e) indicate the surface momentum fluxes.

were dropped because, according to Gauss's theorem, they are equivalent to the difference between the lateral fluxes at the boundaries, which are found to be small.

We find that the profile of the total advective tendency (Fig. 4.4d, i) is close to that of the vertical divergence of the resolved momentum flux (Fig. 4.7b, f). Given that the large–scale advective tendency (first term on the right–hand side of Eq. 4.5) is mostly negligible (Fig. 4.6c, d, i, j), this confirms that the horizontal divergence of horizontal momentum flux, which was omitted (and which represents small–scale horizontal advection), indeed plays no important role (Eq. 4.5). We may thus interpret the resolved momentum fluxes as the main contributors to what we call CMT, including dry and moist convection on scales of 150 m and larger.

As we show in Fig. 4.7, the magnitude of the momentum fluxes is largely determined by the magnitude and structure of the zonal and meridional (geostrophic) wind. The figure shows the daily–averaged profiles of resolved momentum fluxes in the zonal (top row) and meridional direction (bottom row), along with their negative vertical divergence $-\partial_z \overline{u_i'w'}$. On the horizontal axis of Fig. 4.7a and e, the coloured tick marks correspond

to the total turbulent momentum flux at the surface, which reveals the contribution of unresolved fluxes, which is generally largest near the surface. The profiles are coloured by the strength of the respective zonal and meridional surface wind velocity, for winter (blue) and summer (red). Stronger surface wind velocities during winter are accompanied by larger shear in the surface and subcloud layers and larger turbulent fluxes. Above approximately 2 km the fluxes are small, even if clouds are still present at those heights (Fig. 4.7c). Deep convection on some of the summer days does not lead to more momentum flux at greater heights. The meridional momentum flux (Fig. 4.7e) is persistently negative from cloud base upwards, suggesting that faster (more negative) momentum from the near-surface meridional jet (Fig. 4.7h) is transported through the clouds. On two summer days with positive surface v and without a near-surface jet, the meridional momentum flux is negative even at the surface.

Near the surface, the resolved zonal flux divergence is negative, which is associated with an acceleration of easterly flow, as seen in Fig. 4.4d. This may be interpreted as CMT removing air from near the surface, where it has gained a westerly wind component due to surface layer turbulent stresses. Similarly, the resolved meridional flux divergence mostly has the same sign as the surface v, indicating an acceleration of the surface wind due to CMT. At cloud base, both the zonal and the meridional flux divergences act to decelerate the flow. In the zonal component and in winter, this continues to be the case up to about 2 km. The grid size of 150 m is an inherent length-scale limit in the discussion of the effects of CMT above; but this is an artificial cut-off. Hence, in the following section, we question how these results change if we increase the length scale (horizontal resolution) to 300 or 600 m.

4.3.4   Sensitivity to horizontal resolution

Our area of interest has three LES domains with different horizontal resolutions of 150, 300 and 600 m (see Fig. 4.1). Investigating the resolution dependency of our findings allows us to evaluate the role of unresolved motions versus resolved turbulence or convection. We find that the simulated winds and the total advective plus residual tendencies hardly change with resolution (Fig. 4.8a, d, f, i), which shows the large-scale forcing largely sets the frictional tendencies or perhaps that the small-scale processes cannot meaningfully feedback on the large-scale atmosphere. We wonder if this would have been different if a two-way coupling between the LES and the NWP model had been used.

The tendencies from resolved advection (Fig. 4.8b, g) and from the residual (Fig. 4.8c, h) do change with resolution. The differences are most pronounced when the grid is coarsened from 300 m to 600 m, which reduces the resolved zonal momentum flux in the subcloud layer to half its value (Fig. 4.8e), as less turbulence is resolved by the model. Furthermore, the zonal wind tendency due to advection is reduced to zero (or to slightly negative values) in the subcloud layer (Fig. 4.8b), where the residual takes over. Because 600 m is approximately the subcloud layer depth, this implies that overturning circulations associated with dry convection play a key role at introducing friction below and near cloud base. The deceleration of easterly winds by unresolved turbulence in the lower cloud layer is independent of resolution (Fig. 4.8c, h) and presumably caused by
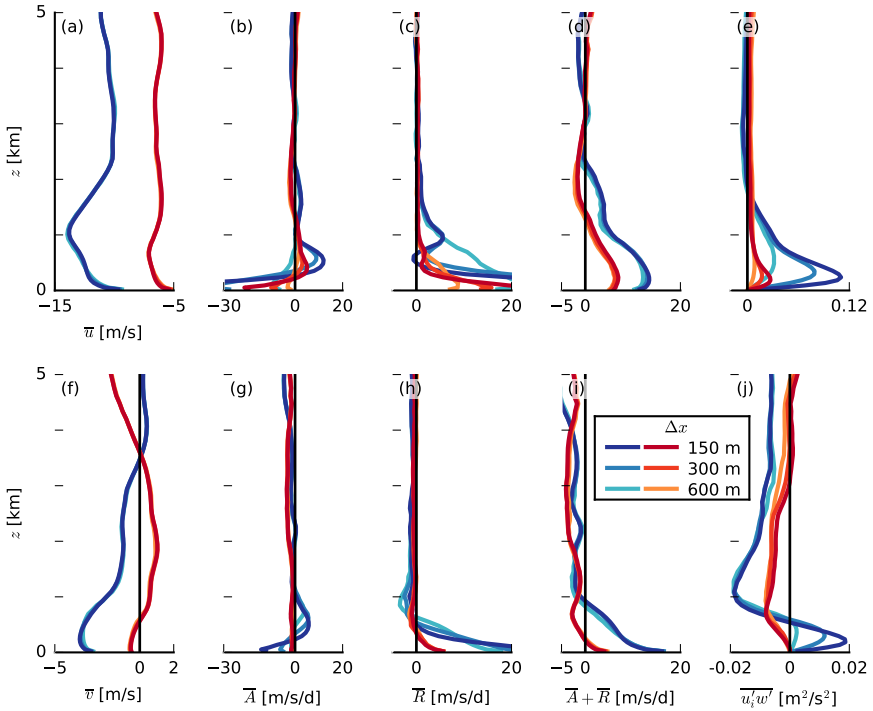
Figure 4.8: Seasonally averaged profiles of (a, f) the wind components u and v, (b, g) advection A, (c, h) residual R, (d, i) the sum of resolved advection and residual $A + R$ and (e, j) turbulent momentum flux $u'w'$ for different horizontal LES resolutions Δx and for (a-e) the zonal wind component and (f-j) the meridional component. Blue/cyan lines depict winter and red/orange lines summer.

the zonal wind jet above cloud base (Fig. 4.8a) (and the meridional wind jet in the surface layer (Fig. 4.8f)), which can introduce significant shear–induced stresses.

4.3.5   Momentum transport in moist regions

To highlight the action of moist convection in setting the momentum flux divergence, we may sample the moistest grid points using the upper quartile of the distribution of column–integrated water vapour (CWV) and contrast them with the driest quartile, presumably representing cloudy and clear sky regions, respectively. We calculate daily averaged momentum flux profiles for the individual quartiles, and average these over winter and summer days (Fig. 4.9a–b for winter and c–d for summer).

First considering winter (Fig. 4.9a–b), we find that the momentum flux profile in the first (Q1, dry) and the second and third quartiles (Q2&Q3) approaches zero at 1 km, whereas the moistest columns (Q4) have a much deeper layer of positive momentum flux (Fig. 4.9a). The differences are not due to different wind profiles, which in fact are very similar for Q1 and Q4 (Fig. 4.9b). Near the cloud–fraction maximum and the zonal–wind jet at about 1 km, there is a thin layer in which the divergence of $u'w'$ in the
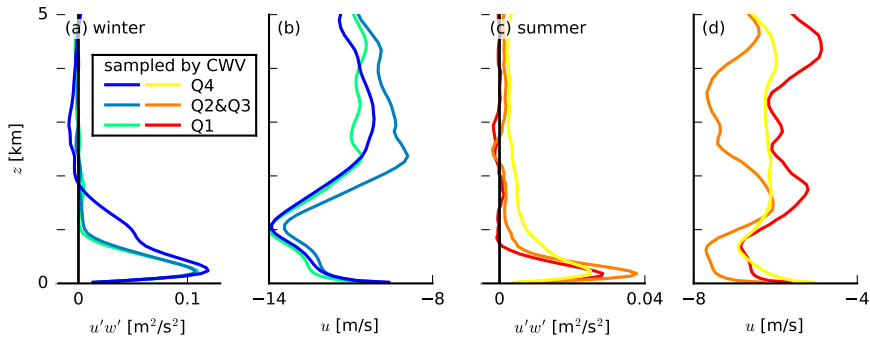
Figure 4.9: Profiles of (a, c) the zonal momentum flux $u'w'$ and (b, d) zonal wind velocity averaged over quartiles of the daily column water vapour (CWV) distribution for (a–b) all December days and (c–d) all August days.

moistest columns is clearly reduced, indicating a layer of only weak deceleration due to momentum transport, as also seen in Fig. 4.7b. Using the same ICON-LEM data, Dixit et al. (2021) show that the momentum flux in positively buoyant updrafts is indeed constant with height or even increases with height in the lower cloud layer. In summer, we find a similar result, whereby moist quartiles with presumably deeper convection lead to the presence of positive momentum flux extending far above the mixed layer, but little divergence (Fig. 4.9c).

4.4 Counter–gradient momentum transport and K–diffusion

Coming back to our main question, *What is the role of shallow convection in the momentum budget of the trades?*, we can summarise our findings as follows: The resolved momentum flux associated with cloud-scale and mesoscale circulations (CMT) acts to: (1) accelerate easterly flow near the surface, (2) slow down easterly flow in the upper mixed–layer and near cloud base and (3) slow down easterly flow in the cloud layer. However, CMT introduces little tendency at the level of the zonal wind jet near 1 km.

Equally important as in the cloud layer appears to be the (dry) convection in the well–mixed subcloud layer. We may use the widely applied K–diffusion approach (also referred to as eddy diffusivity) to evaluate whether the observed momentum fluxes act as so-called down–gradient local turbulent diffusion or as more non-local organised convection. This approach yields a conceptual model for boundary–layer turbulence that has demonstrated skill in explaining surface and boundary layer winds and is a common boundary–layer parametrisation used in global models. It is based on the theoretical assumption that momentum transport is down–gradient and acts to reduce vertical shear in the wind. In the following, we infer how well a K–diffusion model alone would explain the simulated momentum fluxes.
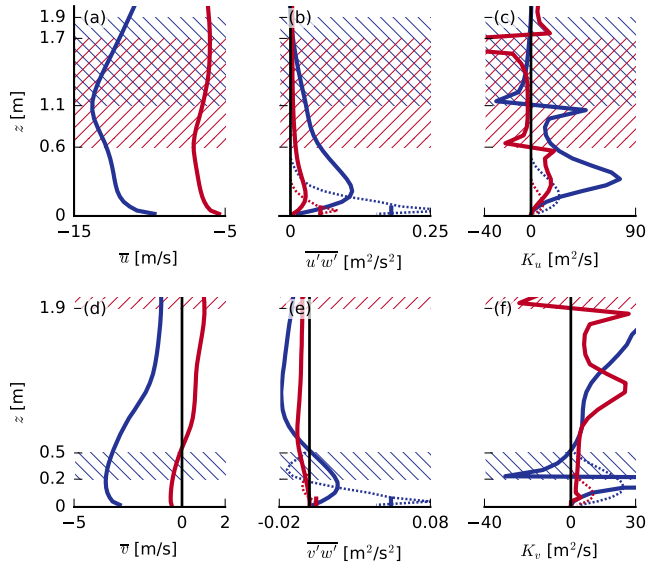
Figure 4.10: Seasonally averaged profiles of (a, d) the wind components u and v, (b, e) the momentum fluxes $\overline{u'w'}$ and $\overline{v'w'}$ and (c, f) the turbulent diffusivity parameter K_u and K_v (calculated as the negative ratio of momentum flux and shear; see Eq. 4.8). The hatching indicates altitudes where $K_i < 0$. Blue lines and hatching from top left to bottom right depict winter and red lines and hatching from top right to bottom left summer. The dotted lines in (c) and (f) indicate the K profile that is computed following Eq. 4.7, and the dotted lines in (b) and (e) indicate the momentum flux computed from that K (Eq. 4.6).

In K–diffusion, the turbulent momentum flux is modelled as the product of the turbulent diffusivity parameter K and the vertical wind gradient:

$$\tau = -\overline{u_i'w'} = K\frac{\partial \overline{u_i}}{\partial z}. \tag{4.6}$$

This expression represents the simplest form of the K–diffusion model, in which a non–local term (as discussed in, e.g., Stevens, 2000) is ignored. One may account for non–local turbulence by combining the K–diffusion approach with a mass–flux approach (Soares et al., 2004; Siebesma et al., 2007; Han et al., 2016).

We show that even the simple approach in Eq. 4.6 is able to adequately predict the unresolved momentum fluxes, reconstructing the turbulent momentum flux produced by the K–diffusion approach with input from the LES and comparing it against the actual resolved fluxes. Following Holtslag & Boville (1993), K may be calculated as:

$$K = \kappa w_m z \left(1 - \frac{z}{h}\right)^2, \tag{4.7}$$

where $\kappa = 0.4$ is the von Kármán constant, w_m is a turbulent scale velocity and h is the boundary–layer height (here, the cloud–base height). For unstable conditions (such as in the present cases), w_m is proportional to the convective velocity scale w_* (Holtslag & Boville, 1993). Using seasonally averaged surface fluxes (of momentum, heat and moisture)

and cloud–base heights h from the simulations, we computed one K profile per season (shown as dotted lines in both Fig. 4.10c and f). These profiles are used to compute momentum fluxes (shown as dotted lines in Fig. 4.10b and e). Also shown in Fig. 4.10 (which zooms in on the lowest 2 km of the atmosphere) are the slab–averaged wind and momentum–flux profiles as calculated from the LES output.

The K–diffusion model seems to produce a reasonable estimation of the (subgrid) turbulent stresses near the surface, where they are close to the surface momentum fluxes output by the LES (indicated by the coloured tick marks in Fig. 4.10b, e). However, above 200 m, coherent structures and larger eddies presumably take over much of the transport. It is these fluxes that introduce important tendencies at cloud base. This is also reflected by the fact that the resolved momentum fluxes become more and more resolution–independent with height, which suggests that large–scale overturning is responsible for the friction introduced near cloud base (see Fig. 4.8). As mentioned before, combined K–diffusion/mass–flux schemes have been shown to better account for this (Han et al., 2016).

Instead of estimating K based on simulated bulk boundary–layer properties, it can be calculated from our wind and momentum–flux profiles. We rearrange Eq. 4.6 to obtain the turbulent diffusivity parameter K for the zonal and meridional wind separately:

$$K_i = -\frac{\overline{u_i' w'}}{\partial_z \overline{u_i}}. \tag{4.8}$$

By definition, a positive K_i denotes down–gradient transport, whereby the momentum flux acts to diffuse existing gradients in wind. If $K_i < 0$, the momentum transport is counter–gradient (also referred to as up–gradient), meaning that the momentum flux acts to increase vertical gradients (shear).

The profiles of K_i (shown as solid lines in Fig. 4.10c and f) reveal several layers of counter–gradient momentum transport both in the zonal and the meridional components (indicated by the hatching in Fig. 4.10). From the surface up to the zonal wind jet, turbulent flux of zonal wind is overall down–gradient, but with a notable reduction in K_u between 400 m and 1 km, i.e. near cloud base. Above the zonal wind jet, the zonal momentum transport is counter–gradient. The flux vanishes and K_u is zero above 1.7 km.

Although we could not include the subgrid fluxes, which introduce considerable tendencies near the surface and cloud base (Fig. 4.8c, h), we find a similar layered structure in the zonal momentum fluxes as Larson et al. (2019) did. While in their BOMEX runs, the counter–gradient layer is some 300 m thick, here it is about twice as thick. In their analysis of the zonal momentum flux budget of the present ICON–LEM simulations, Dixit et al. (2021) note that besides the effective buoyancy production in updrafts, horizontal circulations on scales of several tens of kilometres help increase the presence of (counter–gradient) flux in the cloud layer. However, the production of flux by horizontal circulations is negligible when sampling traditional LES domains on the order of a few 10×10 km^2, which might explain the differences between momentum fluxes in BOMEX and the NAR–VAL days. During boreal summer, $K_u < 0$ over an even deeper layer, but the gradient in $\overline{u}$ is only very slightly negative and the momentum flux is rather weak across that layer. As described in Larson et al. (2019), the counter–gradient flux is a result of updrafts that carry slower momentum ($u' > 0$) across the jet maximum; the momentum flux remains

positive until the updraft wind speed has adjusted to the environment at greater heights, even though the local wind gradient has switched sign.

In the meridional component, a jet is present during winter just above the surface layer, along with a roughly 300-m-thick counter-gradient layer above (Fig. 4.10d–f). In summer, this layer is not present because the meridional wind velocity is close to zero. Instead, a thick layer of weak counter-gradient flux is present above 1.9 km (reaching up to about 3 km; not shown).

4.5   Conclusions

In this paper, we utilised a unique set of large-eddy-simulation (LES) hindcasts that were run over the North Atlantic (Stevens et al., 2019) to study the role of convective momentum transport (CMT) and small-scale turbulence in the momentum budget of the trades. To our knowledge, the present study is the first one to disentangle small-scale and coherent convective-scale influences on the momentum budget for different seasons from LES. Because the inner LES domains for which we constructed the momentum budget do not have periodic boundary conditions and have been run at different horizontal resolutions, the data allows a unique view on the relative roles of turbulent stresses and resolved motions for a variety of synoptic conditions (in contrast to idealised LES cases).

Asking what the role of shallow convection in the momentum budget of the trades is, our analysis focused on boreal-winter days with steady north-easterly winds and shallow cumulus convection under a strong inversion — typical trade-wind conditions — as well as boreal-summer days with weaker winds from the east, somewhat deeper convection and no inversion. In both seasons the combined pressure-gradient and Coriolis force (setting the geostrophic wind) are of a similar order of magnitude as the combined resolved advection and unresolved turbulent stresses. The influence of 'large-scale' mean horizontal and vertical wind advection appears minor, and we interpret the resolved advection largely as CMT, including thermal and mesoscale circulations that take place in the subcloud and cloud layers. Its structure closely matches that of the vertical divergence of the resolved momentum fluxes.

The combined effect of CMT and unresolved turbulence, which we may label as an ageostrophic or frictional term, is to decelerate the easterly trade winds. Especially in winter, when the wind profile exhibits a strong zonal wind jet near cloud base and larger vertical shear in the easterly wind in the cloud layer, the frictional layer is pronounced and extends up to 2 km. However, CMT has a very different effect depending on the altitude considered: It acts to accelerate near-surface winds, by removing air that has gained a westerly component due to surface friction, slow down winds in the central and upper mixed layer and finally, introduce a small amount of 'cumulus friction' in the cloud layer. Notably, CMT introduces little tendency at cloud base where the zonal wind jet resides. By decelerating easterly flow below the jet, it appears to help make the jet more pronounced. In summer, the frictional layer is shallower (only extending up to 1 km) and the friction is overall weaker. The lower depth of the layer reflects the differences in convection: Although in summer, there is also deeper convection at times, this hardly contributes to mean cloudiness, and the remaining shallow convection is shallower (Nuijens et al., 2014; Brueck et al., 2015). The weaker frictional force can

be attributed to the closer location of the ITCZ in summer, which lessens the pressure gradients, requiring less friction to balance the momentum budget.

On the other hand, unresolved turbulence introduces a frictional force that is largest near the surface, as expected, and reduces in magnitude throughout the mixed layer. However, near cloud base and the zonal wind jet, there is significant unresolved turbulence from scales smaller than 150 m that comprise all of the frictional force there. The momentum flux predicted by a K–diffusion model shows that the flux goes to zero about halfway into the mixed-layer, which is where the resolved momentum flux peaks, and where dry convective circulations appear to play an important role. Smaller fluxes that correspond to counter–gradient momentum transport are present above the zonal wind jet (in the cloud layer) and meridional wind jet (above the surface layer), which are a result of slower momentum being carried across these wind speed maxima (Larson et al., 2019).

In conclusion, shallow convection plays an important role in the North Atlantic momentum budget, in particular in decelerating easterly winds below cloud base where momentum fluxes converge. 'Cumulus friction' — a term coined by Schneider & Lindzen (1976) to describe a decelerating effect by (deep) convective momentum transport in the cumulus layer — is not readily present here, as cloud fractions appear too small to introduce large fluxes in the cloud layer. However, there is significant friction near cloud base, which appears associated with smaller–scale turbulent stresses introduced by the zonal wind jet and from the clouds themselves.

4

5

Conclusions

5.1 Recapitulation

The main goal of this thesis was to shed more light on the interaction of the trade winds with cumulus convection. Specifically, the research questions that were formulated in Chapter 1 asked about (1) the influence of the wind profile on shallow cumulus convection and its properties and (2) the role of cumulus convection in the momentum budget and in particular at which scales this role is played. The main research object was precipitating convection of medium depth (congestus species), which in recent studies has been shown to be most typical of the trades (Schulz et al., 2021). Both classical, idealised (Chapters 2 and 3) and modern, realistic (Chapter 4) LES set-ups were utilised in this thesis.

Chapter 2 presented LES experiments of idealised trade-wind conditions in which the same surface wind but different amounts and directions of zonal shear were prescribed. It was distinguished between profiles with backward shear (BS), which is most commonly found in the trades where surface easterlies weaken with height and eventually become westerlies, forward shear (FS), where surface easterlies strengthen with height, and with-out shear (NS). Simulations were run on a rather small (ca. 12×12 km^2) and a larger domain (ca. 50×50 km^2) with both interactive and constant surface fluxes. In all set-ups, the NS case developed the deepest clouds, closely followed by the FS case, and clouds in the BS case stay much shallower. Through momentum transport, different wind profiles lead to different surface winds and thus surface fluxes, which affects cloud depth. Lowest surface winds, surface fluxes and cloud-top heights were found under BS. However, even when suppressing this effect by fixing the surface fluxes, differences in cloud-top heights were evident with deepest clouds in the absence of shear. It was shown that any wind shear in the cloud layer weakens cloud updrafts by enhancing the downward oriented pressure perturbation force. However, the FS case still developed clouds that were much deeper than in the BS case, which was attributed to the FS case's enhanced potential to aggregate moisture and form cloud clusters.

Chapter 3 directly followed up on the findings from the previous chapter and further analysed the same large-domain simulations with constant surface fluxes. In addition, simulations were run in which the evaporation of precipitation was turned off in the LES, which suppressed the formation of cold pools but nonetheless only delayed convective deepening to little extent. In these runs without cold pools, new convection develops up-wind of existing clouds. In the absence of shear, this implies that rain falls into emerging updrafts, which hinders the convective development. Conversely, under subcloud-layer forward shear, clouds move away from their subcloud-layer roots, and precipitative down-drafts do not interfere with new convective cells. This aids the deepening of clouds and ultimately the formation of cold pools. Furthermore, subcloud-layer forward shear fa-cilitates lifting at cold-pool edges through a favourable interaction of background and gust-front vorticity.

In Chapter 4, the terms of the horizontal momentum budget were calculated from LES hindcasts that were run on 6 days in December 2013 and 6 days in August 2016 over a large portion of the tropical and subtropical North Atlantic. The simulation set-up consisted of several nested domains that used different resolutions and were forced by analysis data. Resolved advection and subgrid stresses together act as a friction on the trade winds in the lowest 2 km of the atmosphere in boreal winter and the lowest 1 km in boreal summer. Well captured by traditional K-diffusion theory, unresolved stresses are strongest near the surface, where resolved motions (CMT) act to accelerate the flow. Within the upper mixed layer, CMT acts as a friction, but within the cloud layer it has only little influence on the momentum balance. Instead, unresolved turbulence slows down the wind at these altitudes.

5.2   Synthesis

In Chapters 2 and 3, the focus was on the influence that wind shear has on cumulus convection. In the simulations, idealised wind profiles with height-independent shear were prescribed. In reality, however, wind profiles are a lot more complicated: In Chapter 2, a reanalysis climatology of cloud-layer shear in the trades was discussed, and in Chapter 4, LES-modelled wind profiles from that region were presented. They show that during most of the year, backward shear is common in the cloud layer. However, a high day-to-day variability is present and forward shear occurs occasionally in boreal winter and especially during boreal summer months, when the ITCZ is located at higher latitudes. The subcloud layer in the trades is always characterised by forward shear, and a jet is present near cloud base. Both these features are more pronounced during winter than during summer, which can again be attributed to the wander of the ITCZ.

Following these arguments, it is most insightful to summarise the effect of wind shear on trade-wind convection (first research question) by distinguishing shear at different altitudes, i.e. to diverge from the idealised BS/FS profiles that were discussed in Chap-ters 2 and 3. Altogether, wind shear affects trade-wind convection in the following ways (compared to a purely barotropic wind profile):

- In addition to the well-known tilting of clouds (e.g. Neggers et al., 2003; Yamaguchi et al., 2019), wind shear slightly increases cloud fraction near cloud base by up to 10 per cent, regardless of the shear direction. Both effects lead to an increase in overall cloud cover, which matters for cloud-radiative effects.

- Due to convective momentum transport, different wind profiles lead to different surface winds, which alter the surface enthalpy fluxes. A wind profile with backward shear (where slow momentum is transported downward), has weaker surface winds and thus weaker latent heat fluxes especially than without or (even more) with forward shear. This limits the convection's potential to grow deep (see also Nuijens & Stevens, 2012).

- Forward shear in the subcloud layer implies that clouds move faster than their roots (thermal updrafts), letting precipitation fall downwind of the updraft. This can facilitate cloud deepening and, as a consequence, the aggregation of moisture and the formation of cold pools. Conversely, if no or only little shear is present in the subcloud layer, clouds and roots do not get spatially separated and precipitative downdrafts impede updraft regions, resulting in shallower clouds, less moisture aggregation and rarer cold pools.

- Regardless of its direction, wind shear in the cloud layer enhances the downward oriented pressure perturbation force, which leads to weaker cloud updrafts. This is a another mechanism that limits convective depth under shear (see also Peters et al., 2019). However, in our experiments clouds under backward shear are significantly shallower than under forward shear (which are still a bit shallower than without shear), suggesting that the aforementioned cloud-morphology disadvantage in the presence of backward shear is more dominant (at least in our experiments). This in turn implies only a minor disadvantage in the presence of forward shear due to weaker updrafts compared to a non-sheared wind profile.

- In the presence of cold pools, backward shear can hamper the triggering of secondary convection at the cold-pool front (see also Li et al., 2014). The preferred location of such secondary convection is at the cold pool's downwind front, where negative vorticity due to the near-surface forward shear and positive vorticity within the front facilitate mechanical lifting. This vorticity contrast depends on the strength of the cold-pool front (which in turn may be affected by CMT) and the amount of near-surface forward shear.

- As a result of the mechanisms that affect convective depth (morphology, surface fluxes, updrafts), the cloud-layer properties are altered. In our experiments, this is most clearly evident in the relative humidity. When clouds remain shallower and detrain their moisture in a layer of limited depth, the cloud layer is moister in terms of relative humidity and characterised by a sharper hydrolapse at its top. Conversely, when conditions are favourable for deepening (forward shear), the boundary-layer top becomes less well-defined, and relative humidity above the boundary layer increases.

The knowledge of the typical shape of the trade-wind profile throughout the year and of the effect that wind shear at certain heights has on convection allows us to gauge the role that wind shear plays in the trades as a whole. The forward shear in the trade-wind subcloud layer allows for a cloud morphology that favours convective deepening and facilitates the triggering of secondary convection at cold-pool fronts. Furthermore, convective momentum transport helps to strengthen surface winds, leading to surface-flux conditions that are also favourable for convective deepening. The common backward

5

shear in the cloud layer leads to a disadvantage for the convection, as it weakens cloud updrafts, and thus mostly caps further growth once clouds reach the congestus phase. It is noteworthy that precipitating congestus clouds organised as 'gravel' form the most common type of convective organisation in the trades (Schulz et al., 2021), but to what extent this pattern is determined by wind shear is a not yet fully answered question (Bony et al., 2020). This underlines the great importance to focus on this species of clouds as well as their organisation.

   The unique set of realistic, large–domain LES simulations that was utilised in Chapter 4 proved to be extremely useful to answer my second research question. It allowed for the disentanglement of the influence of small–scale turbulence and larger–scale convective motions within the momentum budget and to obtain detailed knowledge of the vertical structure of each of the forces within that budget. Overall, the following main conclusions can be synthesised from that study:

- Advection that is resolved by the LES (which can be interpreted as CMT) and turbulent stress at subgrid scales, combined, act to decelerate the trade winds up to a height of about 2 km in boreal winter and 1 km in boreal summer, thus turning the wind across the isobars. These differences in the depth of the frictional layer are due to differences in the convective structure: In summer, shallow convection is shallower despite occasional deep convective events, which have a low statistical weight (Nuijens et al., 2014; Brueck et al., 2015). The frictional force is also weaker in summer, which is a consequence of the reduced wind speed due to the weaker pressure gradient associated with the northward wander of the ITCZ.

- Taken by itself, CMT accelerates near–surface winds, by removing air masses that have been slowed down through surface friction. As mentioned above, this is favourable for convective deepening. While in the upper subcloud layer, it acts as a friction, it only has very little effect on the cloud–layer wind. Though this latter effect can be directly attributed to cloudy areas, the term 'cumulus friction' seems hardly justified in the context of shallow convection. Even on days with deeper convection (which may occur under more barotropic conditions, for instance), only little momentum flux is present at greater heights.

- Subgrid–scale turbulence introduces significant friction near the surface, overcoming the accelerating effect of CMT. Quickly decreasing with height, subgrid turbulence is also of importance from cloud base upwards where it decelerates the wind. Traditional K–diffusion models, which are still a common way of parametrising subgrid turbulence in large–scale models, capture the behaviour of this term near the surface and within the lower subcloud layer well but not the friction from cloud base upwards, which can be associated with in–cloud turbulence.

- Layers of (resolved) counter–gradient momentum transport commonly occur above the zonal jet near cloud base and the meridional jet above the surface layer. They might therefore play a role in maintaining these wind speed maxima (see also Larson et al., 2019; Dixit et al., 2021).

This is a good point to reflect on the premise of this dissertation: the CloudBrake project. Its main hypothesis was that CMT weakens the Hadley circulation by accelerating the surface winds. This may sound counter–intuitive at first. The idea is that by counteracting

surface friction, CMT reduces the turning of the wind across the isobars and thus the meridional component of the trade winds, which form the lower branch of the Hadley circulation. It can be concluded that the findings from Chapter 4 support this hypothesis.

5.3 Uncertainties

The focus of the work presented here was implicitly (Chapters 2 and 3) or explicitly (Chapter 4) on the North Atlantic trade-wind region east of Barbados, but there is reason to believe that this is not a limitation and that the findings from this region can be applied to the trades in general (Medeiros & Nuijens, 2016). It also seems reasonable to assume that the insights about the momentum budget that were gained from a location upstream of Barbados (see Fig. 4.1) can be applied to other marine locations (of the same latitude). Proximity to land (upwind) may be a factor that causes differences in the momentum budget, and over land itself, the budget will likely look entirely different, for example due to stronger surface friction and orographic effects.

Although in Chapter 2, some simulations with an interactive surface-flux scheme were presented, most of the analysis on the effect of wind shear on convection was done using simulations with constant surface enthalpy fluxes. This was done to eliminate one factor that causes strong feedbacks and to isolate the effect of wind shear itself as much as possible. It was also shown that the overall response of convection on changes in wind shear (i.e. that clouds stay shallower under shear) is independent of the surface-flux scheme. However, only limited analysis was done on how the cold-pool structure and the triggering of secondary convection is affected by interactive surface fluxes. While some studies suggest that marine cold pools of the size considered here can be captured well in simulations with constant surface fluxes (Gentine et al., 2016), especially the possible thermodynamic mechanism of triggering secondary convection is dependent on thermo-dynamic feedback with the surface (Tompkins, 2001). A complication is that interactive fluxes in the set-up used here lead to much deeper convection and thus stronger cold pools. A possible approach to circumnavigate this challenge is to identify to what extent surface-flux variability is caused by surface-wind gustiness or by downward mixing of air from the free troposphere. By fixing only the winds or the near-surface gradient in the surface-flux parametrisation (see Eq. 2.5), this would in itself provide important insights into the physics of cold pools.

Another possible shortcoming of the LES studies in Chapters 2 and 3 is the domain size. While 50×50 km^2 is still much larger than conventional LES studies, it is still only sufficient to contain one or two large cold pools at a time (see for example Fig. 3.3). It would be desirable to run such simulations on even larger domains (say 200×200 km^2) to better capture large-scale organisation and the interaction of cold pools. A factor related to this are the periodic boundary conditions used here, which have been shown to unphysically constrain horizontal circulations (Badlan et al., 2017; Dixit et al., 2021). Nested set-ups with open boundaries as utilised in Chapter 4 offer a possible solution for this problem.

An oddity that was encountered while designing the LES case for Chapter 2 was DALES's tendency to produce unphysical turbulence at great heights where the vertical grid is more and more coarsened. This turbulence originated in the model's advection module and could under some conditions even cause model crashes. The problem was

5

ultimately circumvented by choosing a lower coarsening factor in the vertical grid, through which the vertical grid length was kept below 200 m even at the top of the domain and no spurious turbulence developed. It is thus unlikely that this problem affects the results presented here, but a further investigation of the issue is recommendable.

5.4   Recommendations

An obvious line of future research is to confirm the findings of this thesis through observations. To this end, data from the EUREC[4]A field campaign that took place east and south of Barbados may be an invaluable source of information (Stevens et al., 2021). Among others, it deployed hundreds of radiosondes and dropsondes, which may be used to estimate the momentum budget as we did here in Chapter 4. Additionally, data from two wind lidars onboard the research vessel Meteor may be used to constrain momentum fluxes within the boundary layer. Furthermore, the complementing data from for example cloud radars may be useful to test the findings from Chapters 2 and 3. However, cloud structure and depth is influenced by a multitude of factors and finding correlation or even causality between two (e.g. wind shear and cloud depth) is not an easy feat (Brueck et al., 2015). Therefore, even the wealth of observations from the one-month-long EUREC[4]A campaign will likely not be sufficient to this end. Instead, one could also make use of long-standing records of satellite and ground-based remote-sensing data, for example from the Barbados Cloud Observatory. However, even with this approach one may face difficulties because wind-profile measurements are only sparsely available, although the launch of ESA's Aelous satellite in 2018 may offer some relief in that respect (Straume et al., 2020).

Once backed up by observations, the next step would be to verify that parametrisations in large-scale models capture the findings of this thesis. Here, the NARVAL simulations could once again offer valuable insight. The area of interest in Chapter 4 is not only covered by three LES domains but also by two domains that use NWP physics (see Fig. 4.1). Expanding the resolution comparison that was already carried out in Chapter 4 to those domains would provide insights into the performance of the parametrisations.

Intriguing differences with shear in wind speed within cold pools were described in Chapter 3. In particular, cold pools were shown to have an asymmetric structure in the absence of shear and under forward shear. Inspired by studies of deep convection (Mahoney et al., 2009; Grant et al., 2020), it was hypothesised that these asymmetries could be attributed to CMT. To find evidence for this, one could sample the horizontal momentum budget within cold pools. This would constrain the role of CMT in shallow convective cold pools.

By design, the study at hand only allows for very limited conclusions as to what the findings imply for Earth's climate and global warming. In particular, it can only be speculated what the wind shear's influence on clouds means for their radiative effect. Low clouds (like stratocumulus or shallow cumuli) mainly have a cooling effect because they mostly act as reflectors of short-wave radiation. However, cloud deepening implies lower cloud-top temperatures and higher cloud optical depth, which results in less emission of long-wave radiation and thus a potential warming effect (Kubar et al., 2007). One could thus hypothesise that by keeping trade-wind clouds shallow, wind shear weakens the (likely) positive cloud feedback (and consequently, lowers the equilibrium climate

sensitivity). Note that this assumes that wind shear remains the same in a warmer climate, which may not be a valid assumption (e.g. Lu et al., 2007; Vecchi & Soden, 2007). Nonetheless it would be worthwhile to test the hypothesis by repeating (some of) the experiments from Chapter 2 with an interactive radiation scheme and be it only to test the robustness of the finding from this thesis in a more realistic setting. One has to keep in mind though that switching to interactive radiation itself seems to have an effect on cloud depth and structure (Vogel et al., 2016).

Traditionally, the main limiting factor of convective depth in the trades is thought to be the presence of a strong inversion, which is maintained by the interplay of convection and the Hadley cell's strong subsidence (e.g. Siebesma, 1998; Stevens, 2005). However, it was shown in this thesis that wind shear plays some role too. What remains unclear is exactly how important each of these two players are: Does wind shear affect cumulus convection in other weather systems in mid-latitudes and over land in similar ways? Some hints to answer this question can be found in studies of deep convection (i.e. in the absence of subsidence) where it has been found that wind shear limits convective depth by 'blowing off' cloud tops (e.g. Sathiyamoorthy et al., 2004; Koren et al., 2010). Furthermore, both here and elsewhere (e.g. Rotunno & Klemp, 1982; Rotunno et al., 1988; Hildebrand, 1998; Weisman & Rotunno, 2004; Chen et al., 2015), shear has been shown to favour convective organisation.

The analysis of the NARVAL simulations in Chapter 4 shows the great value of such datasets beyond their original purpose. In this case, the main intention of the ICON-LEM simulations was to assess the model quality and to test the sampling strategy that was followed during the NARVAL flight campaigns (Stevens et al., 2019). However, by making the dataset available to a wider group of researchers, a great amount of insight on other aspects could be gained here and by other authors (Vial et al., 2019; Vogel et al., 2020; Naumann & Kiemle, 2020; Dixit et al., 2021). Rightly, there is an increasing tendency to carry out such expensive simulations (see for example Stevens et al., 2020a), and it is desirable to continue on a path where detailed output of such simulations is readily available to other researchers. To allow for a wide range of possible analyses, it is however necessary to record a large amount of output (including 3D fields), and the immense size of such datasets is a practical challenge that needs to be addressed.

5

Bibliography

Asai, T. (1964). Cumulus Convection in the Atmosphere with Vertical Wind Shear: Numerical Experiment. *Journal of the Meteorological Society of Japan. Ser. II*, 42(4), 245–259. doi:10.2151/jmsj1923.42.4_245.

Augstein, E., Schmidt, H. & Ostapoff, F. (1974). The vertical structure of the atmospheric planetary boundary layer in undisturbed trade winds over the Atlantic Ocean. *Boundary-Layer Meteorology*, 6(1), 129–150. doi:10.1007/BF00232480.

Back, L. E. & Bretherton, C. S. (2009). On the Relationship between SST Gradients, Boundary Layer Winds, and Convergence over the Tropical Oceans. *Journal of Climate*, 22(15), 4182–4196. doi:10.1175/2009JCLI2392.1.

Badlan, R. L., Lane, T. P., Moncrieff, M. W. & Jakob, C. (2017). Insights into convective momentum transport and its parametrization from idealized simulations of organized convection. *Quarterly Journal of the Royal Meteorological Society*, 143(708), 2687–2702. doi:10.1002/qj.3118.

Bellon, G. & Stevens, B. (2012). Using the Sensitivity of Large-Eddy Simulations to Evaluate Atmospheric Boundary Layer Models. *Journal of the Atmospheric Sciences*, 69(5), 1582–1601. doi:10.1175/JAS-D-11-0160.1.

Betts, A. K. (1975). Parametric Interpretation of Trade-Wind Cumulus Budget Studies. *Journal of the Atmospheric Sciences*, 32(10), 1934–1945. doi:10.1175/1520-0469(1975)032<1934:PIOTWC>2.0.CO;2.

Black, P. G. (1978). Mesoscale Cloud Patterns Revealed by Apollo-Soyuz Photographs. *Bulletin of the American Meteorological Society*, 59(11), 1409–1419. doi:10.1175/1520-0477(1978)059<1409:MCPRBA>2.0.CO;2.

Böing, S. J., Jonker, H. J. J., Siebesma, A. P. & Grabowski, W. W. (2012). Influence of the Subcloud Layer on the Development of a Deep Convective Ensemble. *Journal of the Atmospheric Sciences*, 69(9), 2682–2698. doi:10.1175/JAS-D-11-0317.1.

Bony, S. & Dufresne, J.-L. (2005). Marine boundary layer clouds at the heart of tropical cloud feedback uncertainties in climate models. *Geophysical Research Letters*, 32(20). doi:10.1029/2005GL023851.

Bony, S., Stevens, B., Held, I. H., Mitchell, J. F., Dufresne, J.-L., Emanuel, K. A., Friedlingstein, P., Griffies, S. & Senior, C. (2013). Carbon Dioxide and Climate: Perspectives on a Scientific Assessment. In: G. R. Asrar & J. W. Hurrell (eds.), *Climate Science for Serving Society*, pp. 391–413. Springer Netherlands, Dordrecht. doi:10.1007/978-94-007-6692-1_14.

Bony, S., Stevens, B., Frierson, D. M. W., Jakob, C., Kageyama, M., Pincus, R., Shepherd, T. G., Sherwood, S. C., Siebesma, A. P., Sobel, A. H., Watanabe, M. & Webb, M. J. (2015). Clouds, circulation and climate sensitivity. *Nature Geoscience*, 8(4), 261–268. doi:10.1038/ngeo2398.

Bony, S., Stevens, B., Ament, F., Bigorre, S., Chazette, P., Crewell, S., Delanoë, J., Emanuel, K., Farrell, D., Flamant, C., Gross, S., Hirsch, L., Karstensen, J., Mayer, B., Nuijens, L., Ruppert, J. H., Sandu, I., Siebesma, P., Speich, S., Szczap, F., Totems, J., Vogel, R., Wendisch, M. & Wirth, M. (2017). EUREC4A: A Field Campaign to Elucidate the Couplings Between Clouds, Convection and Circulation. *Surveys in Geophysics*, 38(6), 1529–1568. doi:10.1007/s10712-017-9428-0.

Bony, S., Schulz, H., Vial, J. & Stevens, B. (2020). Sugar, Gravel, Fish, and Flowers: Dependence of Mesoscale Patterns of Trade-Wind Clouds on Environmental Conditions. *Geophysical Research Letters*, 47(7), 1–9. doi:10.1029/2019GL085988.

Bretherton, C. S. (2015). Insights into low-latitude cloud feedbacks from high-resolution models. *Philosophical Transactions of the Royal Society A: Mathematical, Physical and Engineering Sciences*, 373(2054), 20140415. doi:10.1098/rsta.2014.0415.

Bretherton, C. S. & Blossey, P. N. (2017). Understanding Mesoscale Aggregation of Shallow Cumulus Convection Using Large-Eddy Simulation. *Journal of Advances in Modeling Earth Systems*, 9(8), 2798–2821. doi:10.1002/2017MS000981.

Brown, A. R. (1999). Large-eddy simulation and parametrization of the effects of shear on shallow cumulus convection. *Boundary-Layer Meteorology*, 91(1), 65–80. doi:10.1023/A:1001836612775.

Brueck, M., Nuijens, L. & Stevens, B. (2015). On the seasonal and synoptic time-scale variability of the North Atlantic trade wind region and its low-level clouds. *Journal of the Atmospheric Sciences*, 72(4), 1428–1446. doi:10.1175/JAS-D-14-0054.1.

Brümmer, B., Augstein, E. & Riehl, H. (1974). On the low-level wind structure in the Atlantic trade. *Quarterly Journal of the Royal Meteorological Society*, 100(423), 109–121. doi:10.1002/qj.49710042310.

Caldwell, P. M., Zelinka, M. D., Taylor, K. E. & Marvel, K. (2016). Quantifying the Sources of Intermodel Spread in Equilibrium Climate Sensitivity. *Journal of Climate*, 29(2), 513–524. doi:10.1175/JCLI-D-15-0352.1.

Carr, M. T. & Bretherton, C. S. (2001). Convective momentum transport over the tropical pacific: Budget estimates. *Journal of the Atmospheric Sciences*, 58(13), 1673–1693. doi:10.1175/1520-0469(2001)058<1673:CMTOTT>2.0.CO;2.

Charney, J. G., Arakawa, A., Baker, J. D., Bolin, B., Dickinson, R. E., Goody, R. M., Leith, C. E., Stommel, H. M. & Wunsch, C. I. (1979). *Carbon dioxide and climate: a scientific assessment.* National Academy of Sciences, Washington, DC.

Chen, Q., Fan, J., Hagos, S., Gustafson, W. I. & Berg, L. K. (2015). Roles of wind shear at different vertical levels: Cloud system organization and properties. *Journal of Geophysical Research: Atmospheres*, 120(13), 6551–6574. doi:10.1002/2015JD023253.

Daleu, C. L., Woolnough, S. J. & Plant, R. S. (2012). Cloud-Resolving Model Simulations with One- and Two-Way Couplings via the Weak Temperature Gradient Approximation. *Journal of the Atmospheric Sciences*, 69(12), 3683–3699. doi:10.1175/JAS-D-12-058.1.

Deardorff, J. W. (1970). A numerical study of three-dimensional turbulent channel flow at large Reynolds numbers. *Journal of Fluid Mechanics*, 41(2), 453–480. doi:10.1017/S0022112070000691.

Deser, C. (1993). Diagnosis of the Surface Momentum Balance over the Tropical Pacific Ocean. *Journal of Climate*, 6(1), 64–74. doi:10.1175/1520-0442(1993)006<0064:dotsmb>2.0.co;2.

Dipankar, A., Stevens, B., Heinze, R., Moseley, C., Zängl, G., Giorgetta, M. & Brdar, S. (2015). Large eddy simulation using the general circulation model ICON. *Journal of Advances in Modeling Earth Systems*, 7(3), 963–986. doi:10.1002/2015MS000431.

Dixit, V., Nuijens, L. & Helfer, K. C. (2021). Counter-gradient momentum transport through subtropical shallow convection in ICON-LEM simulations. *Journal of Advances in Modeling Earth Systems*, 13(6). doi:10.1029/2020MS002352.

Fedorovich, E. & Conzemius, R. (2008). Effects of wind shear on the atmospheric convective boundary layer structure and evolution. *Acta Geophysica*, 56(1), 114–141. doi:10.2478/s11600-007-0040-4.

Feng, Z., Hagos, S., Rowe, A. K., Burleyson, C. D., Martini, M. N. & Szoeke, S. P. (2015). Mechanisms of convective cloud organization by cold pools over tropical warm ocean during the ¡scp¿AMIE/DYNAMO¡/scp¿ field campaign. *Journal of Advances in Modeling Earth Systems*, 7(2), 357–381. doi:10.1002/2014MS000384.

Fermepin, S. & Bony, S. (2014). Influence of low-cloud radiative effects on tropical circulation and precipitation. *Journal of Advances in Modeling Earth Systems*, 6(3), 513–526. doi:10.1002/2013MS000288.

Gentine, P., Garelli, A., Park, S. B., Nie, J., Torri, G. & Kuang, Z. (2016). Role of surface heat fluxes underneath cold pools. *Geophysical Research Letters*, 43(2), 874–883. doi:10.1002/2015GL067262.

Grabowski, W. W. (1998). Toward Cloud Resolving Modeling of Large-Scale Tropical Circulations: A Simple Cloud Microphysics Parameterization. *Journal of the Atmospheric Sciences*, 55(21), 3283–3298. doi:10.1175/1520-0469(1998)055<3283:TCRMOL>2.0.CO;2.

Grant, L. D., Moncrieff, M. W., Lane, T. P. & Heever, S. C. (2020). Shear-Parallel Tropical Convective Systems: Importance of Cold Pools and Wind Shear. *Geophysical Research Letters*, 47(12), 1–10. doi:10.1029/2020GL087720.

Han, J., Witek, M. L., Teixeira, J., Sun, R., Pan, H.-L., Fletcher, J. K. & Bretherton, C. S. (2016). Implementation in the NCEP GFS of a Hybrid Eddy-Diffusivity Mass-Flux (EDMF) Boundary Layer Parameterization with Dissipative Heating and Modified Stable Boundary Layer Mixing. *Weather and Forecasting*, 31(1), 341–352. doi:10.1175/WAF-D-15-0053.1.

Heinze, R., Dipankar, A., Henken, C. C., Moseley, C., Sourdeval, O., Trömel, S., Xie, X., Adamidis, P., Ament, F., Baars, H., Barthlott, C., Behrendt, A., Blahak, U., Bley, S., Brdar, S., Brueck, M., Crewell, S., Deneke, H., Di Girolamo, P., Evaristo, R., Fischer, J., Frank, C., Friederichs, P., Göcke, T., Gorges, K., Hande, L., Hanke, M., Hansen, A., Hege, H.-C., Hoose, C., Jahns, T., Kalthoff, N., Klocke, D., Kneifel, S., Knippertz, P., Kuhn, A., van Laar, T., Macke, A., Maurer, V., Mayer, B., Meyer, C. I., Muppa, S. K., Neggers, R. A. J., Orlandi, E., Pantillon, F., Pospichal, B., Röber, N., Scheck, L., Seifert, A., Seifert, P., Senf, F., Siligam, P., Simmer, C., Steinke, S., Stevens, B., Wapler, K., Weniger, M., Wulfmeyer, V., Zängl, G., Zhang, D. & Quaas, J. (2017). Large-eddy simulations over Germany using ICON: a comprehensive evaluation. *Quarterly Journal of the Royal Meteorological Society*, 143(702), 69–100. doi:10.1002/qj.2947.

Helfer, K. C. & Nuijens, L. (2021, in review). The morphology of simulated trade-wind congestus clouds under wind shear. *Earth and Space Science Open Archive*. doi:10.1002/essoar.10506905.1.

Helfer, K. C., Nuijens, L., de Roode, S. R. & Siebesma, A. P. (2020). How Wind Shear Affects Trade-wind Cumulus Convection. *Journal of Advances in Modeling Earth Systems*, 12(12). doi:10.1029/2020MS002183.

HELFER, K. C., NUIJENS, L. & DIXIT, V. V. (2021). The role of shallow convection in the momentum budget of the trades from large-eddy-simulation hindcasts. *Quarterly Journal of the Royal Meteorological Society*, 147(737), 2490–2505. doi:10.1002/qj.4035.

HEUS, T. & JONKER, H. J. J. (2008). Subsiding Shells around Shallow Cumulus Clouds. *Journal of the Atmospheric Sciences*, 65(3), 1003–1018. doi:10.1175/2007JAS2322.1.

HEUS, T., VAN HEERWAARDEN, C. C., JONKER, H. J. J., SIEBESMA, A. P., AXELSEN, S., VAN DEN DRIES, K., GEOFFROY, O., MOENE, A. F., PINO, D., DE ROODE, S. R. & VILÀ-GUERAU DE ARELLANO, J. (2010). Formulation of the Dutch Atmospheric Large-Eddy Simulation (DALES) and overview of its applications. *Geoscientific Model Development*, 3(2), 415–444. doi:10.5194/gmd-3-415-2010.

HILDEBRAND, P. H. (1998). Shear-Parallel Moist Convection over the Tropical Ocean: A Case Study from 18 February 1993 TOGA COARE. *Monthly Weather Review*, 126(7), 1952–1976. doi:10.1175/1520-0493(1998)126<1952:SPMCOT>2.0.CO;2.

HILL, G. E. (1968). On the orientation of cloud bands. *Tellus*, 20(1), 132–137. doi:10.3402/tellusa.v20i1.9936.

HOGAN, T. F. & PAULEY, R. L. (2007). The impact of convective momentum transport on tropical cyclone track forecasts using the Emanuel cumulus parameterization. *Monthly Weather Review*, 135(4), 1195–1207. doi:10.1175/MWR3365.1.

HOLLAND, J. Z. & RASMUSSON, E. M. (1973). Measurements of the Atmospheric Mass, Energy, and Momentum Budgets Over a 500-Kilometer Square of Tropical Ocean. *Monthly Weather Review*, 101(1), 44–55. doi:10.1175/1520-0493(1973)101<0044:MOTAME>2.3.CO;2.

HOLTSLAG, A. A. & BOVILLE, B. A. (1993). Local versus nonlocal boundary-layer diffusion in a global climate model. *Journal of Climate*, 6(10), 1825–1842. doi:10.1175/1520-0442(1993)006<1825:LVNBLD>2.0.CO;2.

INTRIERI, J. M., BEDARD, A. J. & HARDESTY, R. M. (1990). Details of Colliding Thunderstorm Outflows as Observed by Doppler Lidar. *Journal of the Atmospheric Sciences*, 47(9), 1081–1099. doi:10.1175/1520-0469(1990)047<1081:DOCTOA>2.0.CO;2.

KHAIROUTDINOV, M. & RANDALL, D. (2006). High-resolution simulation of shallow-to-deep convection transition over land. *Journal of the Atmospheric Sciences*, 63(12), 3421–3436. doi:10.1175/JAS3810.1.

KHANNA, S. & BRASSEUR, J. G. (1998). Three-dimensional buoyancy- and shear-induced local structure of the atmospheric boundary layer. *Journal of the Atmospheric Sciences*, 55(5), 710–743. doi:10.1175/1520-0469(1998)055<0710:TDBASI>2.0.CO;2.

KIM, D., KUG, J.-S., KANG, I.-S., JIN, F.-F. & WITTENBERG, A. T. (2008). Tropical Pacific impacts of convective momentum transport in the SNU coupled GCM. *Climate Dynamics*, 31(2–3), 213–226. doi:10.1007/s00382-007-0348-4.

KLEIN, S. A., HALL, A., NORRIS, J. R. & PINCUS, R. (2017). Low-Cloud Feedbacks from Cloud-Controlling Factors: A Review. *Surveys in Geophysics*, 38(6), 1307–1329. doi:10.1007/s10712-017-9433-3.

KLOCKE, D., BRUECK, M., HOHENEGGER, C. & STEVENS, B. (2017). Rediscovery of the doldrums in storm-resolving simulations over the tropical Atlantic. *Nature Geoscience*, 10(12), 891–896. doi:10.1038/s41561-017-0005-4.

KOREN, I., REMER, L. A., ALTARATZ, O., MARTINS, J. V. & DAVIDI, A. (2010). Aerosol-induced changes of convective cloud anvils produce strong climate warming. *Atmospheric Chemistry and Physics*, 10(10), 5001–5010. doi:10.5194/acp-10-5001-2010.

KUBAR, T. L., HARTMANN, D. L. & WOOD, R. (2007). Radiative and Convective Driving of Tropical High Clouds. *Journal of Climate*, 20(22), 5510–5526. doi:10.1175/2007JCLI1628.1.

LARSON, V. E., DOMKE, S. & GRIFFIN, B. M. (2019). Momentum Transport in Shallow Cumulus Clouds and Its Parameterization by Higher-Order Closure. *Journal of Advances in Modeling Earth Systems*, 11(11), 3419–3442. doi:10.1029/2019MS001743.

LEMONE, M. A. & PENNELL, W. T. (1976). The Relationship of Trade Wind Cumulus Distribution to Subcloud Layer Fluxes and Structure. *Monthly Weather Review*, 104(5), 524–539. doi:10.1175/1520-0493(1976)104<0524:TROTWC>2.0.CO;2.

LI, Z., ZUIDEMA, P. & ZHU, P. (2014). Simulated convective invigoration processes at trade wind cumulus cold pool boundaries. *Journal of the Atmospheric Sciences*, 71(8), 2823–2841. doi:10.1175/JAS-D-13-0184.1.

LILLY, D. K. (1962). On the numerical simulation of buoyant convection. *Tellus*, 14(2), 148–172. doi:10.1111/j.2153-3490.1962.tb00128.x.

LIN, J. L., MAPES, B. E. & HAN, W. (2008). What are the sources of mechanical damping in Matsuno-Gill-type models? *Journal of Climate*, 21(2), 165–179. doi:10.1175/2007JCLI1546.1.

LOHOU, F., DRUILHET, A., CAMPISTRON, B., REDELSPERGERS, J. L. & SAÏD, F. (2000). Numerical study of the impact of coherent structures on vertical transfers in the atmospheric boundary layer. *Boundary-Layer Meteorology*, 97(3), 361–383. doi:10.1023/A:1002641728075.

LU, J., VECCHI, G. A. & REICHLER, T. (2007). Expansion of the Hadley cell under global warming. *Geophysical Research Letters*, 34(6), L06805. doi:10.1029/2006GL028443.

MAHONEY, K. M., LACKMANN, G. M. & PARKER, M. D. (2009). The Role of Momentum Transport in the Motion of a Quasi-Idealized Mesoscale Convective System. *Monthly Weather Review*, 137(10), 3316–3338. doi:10.1175/2009MWR2895.1.

MALKUS, J. S. (1949). Effects of wind shear on some aspects of convection. *Transactions, American Geophysical Union*, 30(1), 19. doi:10.1029/TR030i001p00019.

MALKUS, J. S. (1952). The slopes of cumulus clouds in relation to external wind shear. *Quarterly Journal of the Royal Meteorological Society*, 78(338), 530–542. doi:10.1002/qj.49707833804.

MALKUS, J. S. (1958). On the structure of the trade wind moist layer. *Papers in Physical Oceanography and Meteorology*, 13(2). doi:10.1575/1912/5443.

MALKUS, J. S. (1963). Cloud Patterns over Tropical Oceans. *Science*, 141(3583), 767–778. doi:10.1126/science.141.3583.767.

MEDEIROS, B. & NUIJENS, L. (2016). Clouds at Barbados are representative of clouds across the trade wind regions in observations and climate models. *Proceedings of the National Academy of Sciences*, 113(22), E3062–E3070. doi:10.1073/pnas.1521494113.

MEYER, B. & HAERTER, J. O. (2020). Mechanical Forcing of Convection by Cold Pools: Collisions and Energy Scaling. *Journal of Advances in Modeling Earth Systems*, 12(11). doi:10.1029/2020MS002281.

MONCRIEFF, M. W. (1997). Momentum Transport by Organized Convection. In: R. K. Smith (ed.), *The Physics and Parameterization of Moist Atmospheric Convection*, pp. 231–253. Springer Netherlands, Dordrecht. doi:10.1007/978-94-015-8828-7_9.

MORRISON, H. & PETERS, J. M. (2018). Theoretical Expressions for the Ascent Rate of Moist Deep Convective Thermals. *Journal of the Atmospheric Sciences*, 75(5), 1699–1719. doi:10.1175/JAS-D-17-0295.1.

MULHOLLAND, J. P., PETERS, J. M. & MORRISON, H. (2021). How does vertical wind shear influence entrainment in squall lines? *Journal of the Atmospheric Sciences*, 78(6), 1931–1946. doi:10.1175/jas-d-20-0299.1.

NAUMANN, A. K. & KIEMLE, C. (2020). The vertical structure and spatial variability of lower-tropospheric water vapor and clouds in the trades. *Atmospheric Chemistry and Physics*, 20(10), 6129–6145. doi:10.5194/acp-20-6129-2020.

NEGGERS, R. A., JONKER, H. J. & SIEBESMA, A. P. (2003). Size statistics of cumulus cloud populations in large-eddy simulations. *Journal of the Atmospheric Sciences*, 60(8), 1060–1074. doi:10.1175/1520-0469(2003)60<1060:SSOCCP>2.0.CO;2.

NEGGERS, R. A., NEELIN, J. D. & STEVENS, B. (2007). Impact mechanisms of shallow cumulus convection on tropical climate dynamics. *Journal of Climate*, 20(11), 2623–2642. doi:10.1175/JCLI4079.1.

NIEUWSTADT, F. T. M. & BROST, R. A. (1986). The Decay of Convective Turbulence. *Journal of the Atmospheric Sciences*, 43(6), 532–546. doi:10.1175/1520-0469(1986)043<0532:TDOCT>2.0.CO;2.

NUIJENS, L. & SIEBESMA, A. P. (2019). Boundary Layer Clouds and Convection over Subtropical Oceans in our Current and in a Warmer Climate. *Current Climate Change Reports*, 5(2), 80–94. doi:10.1007/s40641-019-00126-x.

NUIJENS, L. & STEVENS, B. (2012). The Influence of Wind Speed on Shallow Marine Cumulus Convection. *Journal of the Atmospheric Sciences*, 69(1), 168–184. doi:10.1175/JAS-D-11-02.1.

NUIJENS, L., SERIKOV, I., HIRSCH, L., LONITZ, K. & STEVENS, B. (2014). The distribution and variability of low-level cloud in the North Atlantic trades. *Quarterly Journal of the Royal Meteorological Society*, 140(684), 2364–2374. doi:10.1002/qj.2307.

NUIJENS, L., MEDEIROS, B., SANDU, I. & AHLGRIMM, M. (2015). Observed and modeled patterns of covariability between low-level cloudiness and the structure of the trade-wind layer. *Journal of Advances in Modeling Earth Systems*, 7(4), 1741–1764. doi:10.1002/2015MS000483.

PARK, S.-B., BÖING, S. & GENTINE, P. (2018). Role of Surface Friction on Shallow Nonprecipitating Convection. *Journal of the Atmospheric Sciences*, 75(1), 163–178. doi:10.1175/JAS-D-17-0106.1.

PARKER, D. J. (1996). Cold pools in shear. *Quarterly Journal of the Royal Meteorological Society*, 122(535), 1655–1674. doi:10.1256/smsqj.53508.

PARKER, M. D. (2010). Relationship between System Slope and Updraft Intensity in Squall Lines. *Monthly Weather Review*, 138(9), 3572–3578. doi:10.1175/2010MWR3441.1.

PASTUSHKOV, R. S. (1975). The effects of vertical wind shear on the evolution of convective clouds. *Quarterly Journal of the Royal Meteorological Society*, 101(428), 281–291. doi:10.1002/qj.49710142811.

PETERS, J. M. (2016). The Impact of Effective Buoyancy and Dynamic Pressure Forcing on Vertical Velocities within Two-Dimensional Updrafts. *Journal of the Atmospheric Sciences*, 73(11), 4531–4551. doi:10.1175/JAS-D-16-0016.1.

PETERS, J. M., HANNAH, W. & MORRISON, H. (2019). The Influence of Vertical Wind Shear on Moist Thermals. *Journal of the Atmospheric Sciences*, 76(6), 1645–1659. doi:10.1175/JAS-D-18-0296.1.

PETERSEN, E. L. & TROEN, I. (2012). Wind conditions and resource assessment. *Wiley Interdisciplinary Reviews: Energy and Environment*, 1(2), 206–217. doi:10.1002/wene.4.

RAUBER, R. M., STEVENS, B., OCHS, H. T., KNIGHT, C., ALBRECHT, B. A., BLYTH, A. M., FAIRALL, C. W., JENSEN, J. B., LASHER-TRAPP, S. G., MAYOL-BRACERO, O. L., VALI, G., ANDERSON, J. R., BAKER, B. A., BANDY, A. R., BURNET, E., BRENGUIER, J.-L., BREWER, W. A., BROWN, P. R. A., CHUANG, R., COTTON, W. R., DI GIROLAMO, L., GEERTS, B., GERBER, H., GÖKE, S., GOMES, L., HEIKES, B. G., HUDSON, J. G., KOLLIAS, P., LAWSON, R. R., KRUEGER, S. K., LENSCHOW, D. H., NUIJENS, L., O'SULLIVAN, D. W., RILLING, R. A., ROGERS, D. C., SIEBESMA, A. P., SNODGRASS, E., STITH, J. L., THORNTON, D. C., TUCKER, S., TWOHY, C. H. & ZUIDEMA, P. (2007). Rain in Shallow Cumulus Over the Ocean: The RICO Campaign. *Bulletin of the American Meteorological Society*, 88(12), 1912–1928. doi:10.1175/BAMS-88-12-1912.

RICHTER, I., BEHERA, S. K., DOI, T., TAGUCHI, B., MASUMOTO, Y. & XIE, S.-P. (2014). What controls equatorial Atlantic winds in boreal spring? *Climate Dynamics*, 43(11), 3091–3104. doi:10.1007/s00382-014-2170-0.

RICHTER, J. H. & RASCH, P. J. (2008). Effects of Convective Momentum Transport on the Atmospheric Circulation in the Community Atmosphere Model, Version 3. *Journal of Climate*, 21(7), 1487–1499. doi:10.1175/2007JCLI1789.1.

RIEHL, H., YEH, T. C., MALKUS, J. S. & LA SEUR, N. E. (1951). The north-east trade of the Pacific Ocean. *Quarterly Journal of the Royal Meteorological Society*, 77(334), 598–626. doi:10.1002/qj.49707733405.

ROBE, F. R. & EMANUEL, K. A. (2001). The Effect of Vertical Wind Shear on Radiative–Convective Equilibrium States. *Journal of the Atmospheric Sciences*, 58(11), 1427–1445. doi:10.1175/1520-0469(2001)058<1427:TEOVWS>2.0.CO;2.

ROMPS, D. M. & CHARN, A. B. (2015). Sticky thermals: Evidence for a dominant balance between buoyancy and drag in cloud updrafts. *Journal of the Atmospheric Sciences*, 72(8), 2890–2901. doi:10.1175/JAS-D-15-0042.1.

ROMPS, D. M. & JEEVANJEE, N. (2016). On the sizes and lifetimes of cold pools. *Quarterly Journal of the Royal Meteorological Society*, 142(696), 1517–1527. doi:10.1002/qj.2754.

DE ROODE, S. R., SIEBESMA, A. P., JONKER, H. J. & DE VOOGD, Y. (2012). Parameterization of the vertical velocity equation for shallow cumulus clouds. *Monthly Weather Review*, 140(8), 2424–2436. doi:10.1175/MWR-D-11-00277.1.

ROTUNNO, R. & KLEMP, J. B. (1982). The Influence of the Shear-Induced Pressure Gradient on Thunderstorm Motion. *Monthly Weather Review*, 110(2), 136–151. doi:10.1175/1520-0493(1982)110<0136:TIOTSI>2.0.CO;2.

ROTUNNO, R., KLEMP, J. B. & WEISMAN, M. L. (1988). A Theory for Strong, Long-Lived Squall Lines. *Journal of the Atmospheric Sciences*, 45(3), 463–485. doi:10.1175/1520-0469(1988)045<0463:ATFSLL>2.0.CO;2.

SAGGIORATO, B., NUIJENS, L., SIEBESMA, A. P., DE ROODE, S., SANDU, I. & PAPRITZ, L. (2020). The Influence of Convective Momentum Transport and Vertical Wind Shear on the Evolution of a Cold Air Outbreak. *Journal of Advances in Modeling Earth Systems*, 12(6). doi:10.1029/2019MS001991.

SALESKY, S. T., CHAMECKI, M. & BOU-ZEID, E. (2017). On the Nature of the Transition Between Roll and Cellular Organization in the Convective Boundary Layer. *Boundary-Layer Meteorology*, 163(1), 41–68. doi:10.1007/s10546-016-0220-3.

SANDU, I., BECHTOLD, P. & NUIJENS, L. (2020). On the causes of systematic forecast biases in near-surface wind direction over the oceans. Tech. rep., ECMWF Technical Memoranda. doi:10.21957/wggbl43u.

SATHIYAMOORTHY, V., PAL, P. K. & JOSHI, P. C. (2004). Influence of the Upper-Tropospheric Wind Shear upon Cloud Radiative Forcing in the Asian Monsoon Region. *Journal of Climate*, 17(14), 2725–2735. doi:10.1175/1520-0442(2004)017<2725:IOTUWS>2.0.CO;2.

SATO, Y., SHIMA, S. & TOMITA, H. (2018). Numerical Convergence of Shallow Convection Cloud Field Simulations: Comparison Between Double-Moment Eulerian and Particle-Based Lagrangian Microphysics Coupled to the Same Dynamical Core. *Journal of Advances in Modeling Earth Systems*, 10(7), 1495–1512. doi:10.1029/2018MS001285.

SCHALKWIJK, J., JONKER, H. J. J., SIEBESMA, A. P. & VAN MEIJGAARD, E. (2015). Weather Forecasting Using GPU-Based Large-Eddy Simulations. *Bulletin of the American Meteorological Society*, 96(5), 715–723. doi:10.1175/BAMS-D-14-00114.1.

SCHLEMMER, L. & HOHENEGGER, C. (2014). The Formation of Wider and Deeper Clouds as a Result of Cold-Pool Dynamics. *Journal of the Atmospheric Sciences*, 71(8), 2842–2858. doi:10.1175/JAS-D-13-0170.1.

SCHLEMMER, L., BECHTOLD, P., SANDU, I. & AHLGRIMM, M. (2017). Uncertainties related to the representation of momentum transport in shallow convection. *Journal of Advances in Modeling Earth Systems*, 9(2), 1269–1291. doi:10.1002/2017MS000915.

SCHMIDT, H. & SCHUMANN, U. (1989). Coherent structure of the convective boundary layer derived from large-eddy simulations. *Journal of Fluid Mechanics*, 200(D11), 511–562. doi:10.1017/S0022112089000753.

SCHNEIDER, E. K. & LINDZEN, R. S. (1976). A discussion of the parameterization of momentum exchange by cumulus convection. *Journal of Geophysical Research*, 81(18), 3158–3160. doi:10.1029/JC081i018p03158.

SCHULZ, H., EASTMAN, R. & STEVENS, B. (2021, in review). Characterization and Evolution of Organized Shallow Convection in the Trades. *Earth and Space Science Open Archive*. doi:10.1002/essoar.10505836.1.

SEIFERT, A. & HEUS, T. (2013). Large-eddy simulation of organized precipitating trade wind cumulus clouds. *Atmospheric Chemistry and Physics*, 13(11), 5631–5645. doi:10.5194/acp-13-5631-2013.

SHERWOOD, S. C., WEBB, M. J., ANNAN, J. D., ARMOUR, K. C., FORSTER, P. M., HARGREAVES, J. C., HEGERL, G., KLEIN, S. A., MARVEL, K. D., ROHLING, E. J., WATANABE, M., ANDREWS, T., BRACONNOT, P., BRETHERTON, C. S., FOSTER, G. L., HAUSFATHER, Z., VON DER HEYDT, A. S., KNUTTI, R., MAURITSEN, T., NORRIS, J. R., PROISTOSESCU, C., RUGENSTEIN, M., SCHMIDT, G. A., TOKARSKA, K. B. & ZELINKA, M. D. (2020). An Assessment of Earth's Climate Sensitivity Using Multiple Lines of Evidence. *Reviews of Geophysics*, 58(4), 1–92. doi:10.1029/2019RG000678.

SIEBESMA, A. P. (1998). Shallow Cumulus Convection. In: *Buoyant Convection in Geophysical Flows*, pp. 441–486. Springer Netherlands, Dordrecht. doi:10.1007/978-94-011-5058-3_19.

SIEBESMA, A. P. & CUIJPERS, J. W. M. (1995). Evaluation of Parametric Assumptions for Shallow Cumulus Convection. *Journal of the Atmospheric Sciences*, 52(6), 650–666. doi:10.1175/1520-0469(1995)052<0650:EOPAFS>2.0.CO;2.

SIEBESMA, A. P., BRETHERTON, C. S., BROWN, A., CHLOND, A., CUXART, J., DUYNKERKE, P. G., JIANG, H., KHAIROUTDINOV, M., LEWELLEN, D., MOENG, C.-H., SANCHEZ, E., STEVENS, B. & STEVENS, D. E. (2003). A Large Eddy Simulation Intercomparison Study of Shallow Cumulus Convection. *Journal of the Atmospheric Sciences*, 60(10), 1201–1219. doi:10.1175/1520-0469(2003)60<1201:ALESIS>2.0.CO;2.

SIEBESMA, A. P., SOARES, P. M. M. & TEIXEIRA, J. (2007). A Combined Eddy-Diffusivity Mass-Flux Approach for the Convective Boundary Layer. *Journal of the Atmospheric Sciences*, 64(4), 1230–1248. doi:10.1175/JAS3888.1.

SMAGORINSKY, J. (1963). General circulation experiments with the primitive equations. *Monthly Weather Review*, 91(3), 99–164. doi:10.1175/1520-0493(1963)091<0099:GCEWTP>2.3.CO;2.

SOARES, P., MIRANDA, P., SIEBESMA, A. & TEIXEIRA, J. (2004). An eddy-diffusivity/mass-flux parametrization for dry and shallow cumulus convection. *Quarterly Journal of the Royal Meteorological Society*, 130(604), 3365–3383. doi:10.1256/qj.03.223.

SOMMERIA, G. (1976). Three-Dimensional Simulation of Turbulent Processes in an Undisturbed Trade Wind Boundary Layer. *Journal of the Atmospheric Sciences*, 33(2), 216–241. doi:10.1175/1520-0469(1976)033<0216:TDSOTP>2.0.CO;2.

STEPHAN, C. C. (2021). Mechanism for the Formation of Arc-Shaped Cloud Lines over the Tropical Oceans. *Journal of the Atmospheric Sciences*, 78(3), 817–824. doi:10.1175/JAS-D-20-0129.1.

STEVENS, B. (2000). Quasi-Steady Analysis of a PBL Model with an Eddy-Diffusivity Profile and Nonlocal Fluxes. *Monthly Weather Review*, 128(3), 824–836. doi:10.1175/1520-0493(2000)128<0824:QSAOAP>2.0.CO;2.

STEVENS, B. (2005). Atmospheric Moist Convection. *Annual Review of Earth and Planetary Sciences*, 33(1), 605–643. doi:10.1146/annurev.earth.33.092203.122658.

STEVENS, B., DUAN, J., MCWILLIAMS, J. C., MÜNNICH, M. & NEELIN, J. D. (2002). Entrainment, Rayleigh friction, and boundary layer winds over the tropical Pacific. *Journal of Climate*, 15(1), 30–44. doi:10.1175/1520-0442(2002)015<0030:ERFABL>2.0.CO;2.

STEVENS, B., SHERWOOD, S. C., BONY, S. & WEBB, M. J. (2016). Prospects for narrowing bounds on Earth's equilibrium climate sensitivity. *Earth's Future*, 4(11), 512–522. doi:10.1002/2016EF000376.

STEVENS, B., AMENT, F., BONY, S., CREWELL, S., EWALD, F., GROSS, S., HANSEN, A., HIRSCH, L., JACOB, M., KÖLLING, T., KONOW, H., MAYER, B., WENDISCH, M., WIRTH, M., WOLF, K., BAKAN, S., BAUER-PFUNDSTEIN, M., BRUECK, M., DELANOË, J., EHRLICH, A., FARRELL, D., FORDE, M., GÖDDE, F., GROB, H., HAGEN, M., JÄKEL, E., JANSEN, F., KLEPP, C., KLINGEBIEL, M., MECH, M., PETERS, G., RAPP, M., WING, A. A. & ZINNER, T. (2019). A High-Altitude Long-Range Aircraft Configured as a Cloud Observatory: The NARVAL Expeditions. *Bulletin of the American Meteorological Society*, 100(6), 1061–1077. doi:10.1175/BAMS-D-18-0198.1.

STEVENS, B., ACQUISTAPACE, C., HANSEN, A., HEINZE, R., KLINGER, C., KLOCKE, D., RYBKA, H., SCHUBOTZ, W., WINDMILLER, J., ADAMIDIS, P., ARKA, I., BARLAKAS, V., BIERCAMP, J., BRUECK, M., BRUNE, S., BUEHLER, S. A., BURKHARDT, U., CIONI, G., COSTA-SURÓS, M., CREWELL, S., CRÜGER, T., DENEKE, H., FRIEDRICHS, P., HENKEN, C. C., HOHENEGGER, C., JACOB, M., JAKUB, F., KALTHOFF, N., KÖHLER, M., VAN LAAR, T. W., LI, P., LÖHNERT, U., MACKE, A., MADENACH, N., MAYER, B., NAM, C., NAUMANN, A. K., PETERS, K., POLL, S., QUAAS, J., RÖBER, N., ROCHETIN, N., SCHECK, L., SCHEMANN, V., SCHNITT, S., SEIFERT, A., SENF, F., SHAPKALIJEVSKI, M., SIMMER, C., SINGH, S., SOURDEVAL, O., SPICKERMANN, D., STRANDGREN, J., TESSIOT, O., VERCAUTEREN, N., VIAL, J., VOIGT, A. & ZÄNGL, G. (2020a). The added value of large-eddy and storm-resolving models for simulating clouds and precipitation. *Journal of the Meteorological Society of Japan. Ser. II*, 98(2), 395–435. doi:10.2151/jmsj.2020-021.

STEVENS, B., BONY, S., BROGNIEZ, H., HENTGEN, L., HOHENEGGER, C., KIEMLE, C., L'ECUYER, T. S., NAUMANN, A. K., SCHULZ, H., SIEBESMA, P. A., VIAL, J., WINKER, D. M. & ZUIDEMA, P. (2020b). Sugar, gravel, fish and flowers: Mesoscale cloud patterns in the trade winds. *Quarterly Journal of the Royal Meteorological Society*, 146(726), 141–152. doi:10.1002/qj.3662.

STEVENS, B., BONY, S., FARRELL, D., AMENT, F., BLYTH, A., FAIRALL, C., KARSTENSEN, J., QUINN, P. K., SPEICH, S., ACQUISTAPACE, C., AEMISEGGER, F., ALBRIGHT, A. L., BELLENGER, H., BODENSCHATZ, E., CAESAR, K.-A., CHEWITT-LUCAS, R., DE BOER, G., DELANOË, J., DENBY, L., EWALD, F., FILDIER, B., FORDE, M., GEORGE, G., GROSS, S., HAGEN, M., HAUSOLD, A., HEYWOOD, K. J., HIRSCH, L., JACOB, M., JANSEN, F., KINNE, S., KLOCKE, D., KÖLLING, T., KONOW,

H., Lothon, M., Mohr, W., Naumann, A. K., Nuijens, L., Olivier, L., Pincus, R., Pöhlker, M., Reverdin, G., Roberts, G., Schnitt, S., Schulz, H., Siebesma, A. P., Stephan, C. C., Sullivan, P., Touzé-Peiffer, L., Vial, J., Vogel, R., Zuidema, P., Alexander, N., Alves, L., Arixi, S., Asmath, H., Bagheri, G., Baier, K., Bailey, A., Baranowski, D., Baron, A., Barrau, S., Barrett, P. A., Batier, F., Behrendt, A., Bendinger, A., Beucher, F., Bigorre, S., Blades, E., Blossey, P., Bock, O., Böing, S., Bosser, P., Bourras, D., Bouruet-Aubertot, P., Bower, K., Branellec, P., Branger, H., Brennek, M., Brewer, A., Brilouet, P.-E., Brügmann, B., Buehler, S. A., Burke, E., Burton, R., Calmer, R., Canonici, J.-C., Carton, X., Cato Jr., G., Charles, J. A., Chazette, P., Chen, Y., Chilinski, M. T., Choularton, T., Chuang, P., Clarke, S., Coe, H., Cornet, C., Coutris, P., Couvreux, F., Crewell, S., Cronin, T., Cui, Z., Cuypers, Y., Daley, A., Damerell, G. M., Dauhut, T., Deneke, H., Desbios, J.-P., Dörner, S., Donner, S., Douet, V., Drushka, K., Dütsch, M., Ehrlich, A., Emanuel, K., Emmanouilidis, A., Etienne, J.-C., Etienne-Leblanc, S., Faure, G., Feingold, G., Ferrero, L., Fix, A., Flamant, C., Flatau, P. J., Foltz, G. R., Forster, L., Furtuna, I., Gadian, A., Galewsky, J., Gallagher, M., Gallimore, P., Gaston, C., Gentemann, C., Geyskens, N., Giez, A., Gollop, J., Gouirand, I., Gourbeyre, C., de Graaf, D., de Groot, G. E., Grosz, R., Güttler, J., Gutleben, M., Hall, K., Harris, G., Helfer, K. C., Henze, D., Herbert, C., Holanda, B., Ibanez-Landeta, A., Intrieri, J., Iyer, S., Julien, F., Kalesse, H., Kazil, J., Kellman, A., Kidane, A. T., Kirchner, U., Klingebiel, M., Körner, M., Kremper, L. A., Kretzschmar, J., Krüger, O., Kumala, W., Kurz, A., L'Hégaret, P., Labaste, M., Lachlan-Cope, T., Laing, A., Landschützer, P., Lang, T., Lange, D., Lange, I., Laplace, C., Lavik, G., Laxenaire, R., Le Bihan, C., Leandro, M., Lefevre, N., Lena, M., Lenschow, D., Li, Q., Lloyd, G., Los, S., Losi, N., Lovell, O., Luneau, C., Makuch, P., Malinowski, S., Manta, G., Marinou, E., Marsden, N., Masson, S., Maury, N., Mayer, B., Mayers-Als, M., Mazel, C., McGeary, W., McWilliams, J. C., Mech, M., Mehlmann, M., Meroni, A. N., Mieslinger, T., Minikin, A., Minnett, P., Möller, G., Morfa Avalos, Y., Muller, C., Musat, I., Napoli, A., Neuberger, A., Noisel, C., Noone, D., Nordsiek, F., Nowak, J. L., Oswald, L., Parker, D. J., Peck, C., Person, R., Philippi, M., Plueddemann, A., Pöhlker, C., Pörtge, V., Pöschl, U., Pologne, L., Posyniak, M., Prange, M., Quiñones Meléndez, E., Radtke, J., Ramage, K., Reimann, J., Renault, L., Reus, K., Reyes, A., Ribbe, J., Ringel, M., Ritschel, M., Rocha, C. B., Rochetin, N., Röttenbacher, J., Rollo, C., Royer, H., Sadoulet, P., Saffin, L., Sandiford, S., Sandu, I., Schäfer, M., Schemann, V., Schirmacher, I., Schlenczek, O., Schmidt, J., Schröder, M., Schwarzenboeck, A., Sealy, A., Senff, C. J., Serikov, I., Shohan, S., Siddle, E., Smirnov, A., Späth, F., Spooner, B., Stolla, M. K., Szkó lka, W., de Szoeke, S. P., Tarot, S., Tetoni, E., Thompson, E., Thomson, J., Tomassini, L., Totems, J., Ubele, A. A., Villiger, L., von Arx, J., Wagner, T., Walther, A., Webber, B., Wendisch, M., Whitehall, S., Wiltshire, A., Wing, A. A., Wirth, M., Wiskandt, J., Wolf, K., Worbes, L., Wright, E., Wulfmeyer, V., Young, S., Zhang, C., Zhang, D., Ziemen, F., Zinner, T. & Zöger, M. (2021). EUREC^{4}A. *Earth System Science Data Discussions*. doi:10.5194/essd-2021-18.

Straume, A., Rennie, M., Isaksen, L., de Kloe, J., Marseille, G.-J., Stoffelen, A., Flament, T., Stieglitz, H., Dabas, A., Huber, D., Reitebuch, O., Lemmerz, C., Lux, O., Marksteiner, U., Weiler, F., Witschas, B., Meringer, M., Schmidt, K., Nikolaus, I., Geiss, A., Flamant, P., Kanitz, T., Wernham, D., von Bismarck, J., Bley, S., Fehr, T., Floberghagen, R. & Parinello, T. (2020). ESA's Space-Based Doppler Wind Lidar Mission Aeolus – First Wind and Aerosol Product Assessment Results. *EPJ Web of Conferences*, 237, 01007. doi:10.1051/epjconf/202023701007.

Stull, R. B. (1988). *An Introduction to Boundary Layer Meteorology*. Kluwer Academic Publishers, Dordrecht, 1st edn. doi:10.1007/978-94-009-3027-8.

Sykes, R. I. & Henn, D. S. (1989). Large-Eddy Simulation of Turbulent Sheared Convection. *Journal of the Atmospheric Sciences*, 46(8), 1106–1118. doi:10.1175/1520-0469(1989)046<1106:LESOTS>2.0.CO;2.

Thorpe, A. J., Miller, M. J. & Moncrieff, M. W. (1982). Two-dimensional convection in non-constant shear: A model of mid-latitude squall lines. *Quarterly Journal of the Royal Meteorological Society*, 108(458), 739–762. doi:10.1002/qj.49710845802.

Tian, Y., Kuang, Z., Singh, M. S. & Nie, J. (2019). The Vertical Momentum Budget of Shallow Cumulus Convection: Insights From a Lagrangian Perspective. *Journal of Advances in Modeling Earth Systems*, 11(1), 113–126. doi:10.1029/2018MS001451.

Tiedtke, M., Heckley, W. A. & Slingo, J. (1988). Tropical forecasting at ECMWF: The influence of physical parametrization on the mean structure of forecasts and analyses. *Quarterly Journal of the Royal Meteorological Society*, 114(481), 639–664. doi:10.1002/qj.49711448106.

Tompkins, A. M. (2001). Organization of Tropical Convection in Low Vertical Wind Shears: The Role of Cold Pools. *Journal of the Atmospheric Sciences*, 58(13), 1650–1672. doi:10.1175/1520-0469(2001)058<1650:OOTCIL>2.0.CO;2.

Torri, G., Kuang, Z. & Tian, Y. (2015). Mechanisms for convection triggering by cold pools. *Geophysical Research Letters*, 42(6), 1943–1950. doi:10.1002/2015GL063227.

Vecchi, G. A. & Soden, B. J. (2007). Increased tropical Atlantic wind shear in model projections of global warming. *Geophysical Research Letters*, 34(8). doi:10.1029/2006GL028905.

Vial, J., Dufresne, J.-L. & Bony, S. (2013). On the interpretation of inter-model spread in CMIP5 climate sensitivity estimates. *Climate Dynamics*, 41(11), 3339–3362. doi:10.1007/s00382-013-1725-9.

Vial, J., Bony, S., Stevens, B. & Vogel, R. (2017). Mechanisms and Model Diversity of Trade-Wind Shallow Cumulus Cloud Feedbacks: A Review. *Surveys in Geophysics*, 38(6), 1331–1353. doi:10.1007/s10712-017-9418-2.

Vial, J., Vogel, R., Bony, S., Stevens, B., Winker, D. M., Cai, X., Hohenegger, C., Naumann, A. K. & Brogniez, H. (2019). A New Look at the Daily Cycle of Trade Wind Cumuli. *Journal of Advances in Modeling Earth Systems*, 11(10), 3148–3166. doi:10.1029/2019MS001746.

Vogel, R., Nuijens, L. & Stevens, B. (2016). The role of precipitation and spatial organization in the response of trade-wind clouds to warming. *Journal of Advances in Modeling Earth Systems*, 8(2), 843–862. doi:10.1002/2015MS000568.

Vogel, R., Bony, S. & Stevens, B. (2020). Estimating the Shallow Convective Mass Flux from the Subcloud-Layer Mass Budget. *Journal of the Atmospheric Sciences*, 77(5), 1559–1574. doi:10.1175/JAS-D-19-0135.1.

Warner, C., Simpson, J., Martin, D. W., Suchman, D., Mosher, F. R. & Reinking, R. F. (1979). Shallow Convection on Day 261 of GATE: Mesoscale Arcs. *Monthly Weather Review*, 107(12), 1617–1635. doi:10.1175/1520-0493(1979)107<1617:SCODOG>2.0.CO;2.

Warren, S., Hahn, C., London, J., Chervin, R. & Jenne, R. (1988). Global distribution of total cloud cover and cloud type amounts over the ocean. Tech. rep., USDOE Office of Energy Research (ER). doi:10.2172/5415329.

Weckwerth, T. M. & Wakimoto, R. M. (1992). The Initiation and Organization of Convective Cells atop a Cold-Air Outflow Boundary. *Monthly Weather Review*, 120(10), 2169–2187. doi:10.1175/1520-0493(1992)120<2169:TIAOOC>2.0.CO;2.

Weisman, M. L. & Rotunno, R. (2004). "A Theory for Strong Long-Lived Squall Lines" Revisited. *Journal of the Atmospheric Sciences*, 61(4), 361–382. doi:10.1175/1520-0469(2004)061<0361:ATFSLS>2.0.CO;2.

Wing, A. A., Emanuel, K., Holloway, C. E. & Muller, C. (2017). Convective Self-Aggregation in Numerical Simulations: A Review. *Surveys in Geophysics*, 38(6), 1173–1197. doi:10.1007/s10712-017-9408-4.

Wu, X. & Yanai, M. (1994). Effects of Vertical Wind Shear on the Cumulus Transport of Momentum: Observations and Parameterization. *Journal of the Atmospheric Sciences*, 51(12), 1640–1660. doi:10.1175/1520-0469(1994)051<1640:EOVWSO>2.0.CO;2.

Wyant, M. C., Bretherton, C. S. & Blossey, P. N. (2018). The Sensitivity of Numerical Simulations of Cloud-Topped Boundary Layers to Cross-Grid Flow. *Journal of Advances in Modeling Earth Systems*, 10(2), 466–480. doi:10.1002/2017MS001241.

Xue, H., Feingold, G. & Stevens, B. (2008). Aerosol Effects on Clouds, Precipitation, and the Organization of Shallow Cumulus Convection. *Journal of the Atmospheric Sciences*, 65(2), 392–406. doi:10.1175/2007JAS2428.1.

Yamaguchi, T., Feingold, G. & Kazil, J. (2019). Aerosol-Cloud Interactions in Trade Wind Cumulus Clouds and the Role of Vertical Wind Shear. *Journal of Geophysical Research: Atmospheres*, 124(22), 12244–12261. doi:10.1029/2019JD031073.

Young, G. S. (1988). Turbulence Structure of the Convective Boundary Layer. Part III: The Vertical Velocity Budgets of Thermals and Their Environment. *Journal of the Atmospheric Sciences*, 45(14), 2039–2050. doi:10.1175/1520-0469(1988)045<2039:TSOTCB>2.0.CO;2.

Zängl, G., Reinert, D., Rípodas, P. & Baldauf, M. (2015). The ICON (ICOsahedral Non-hydrostatic) modelling framework of DWD and MPI-M: Description of the non-hydrostatic dynamical core. *Quarterly Journal of the Royal Meteorological Society*, 141(687), 563–579. doi:10.1002/qj.2378.

van Zanten, M. C., Stevens, B., Nuijens, L., Siebesma, A. P., Ackerman, A. S., Burnet, F., Cheng, A., Couvreux, F., Jiang, H., Khairoutdinov, M., Kogan, Y., Lewellen, D. C., Mechem, D., Nakamura, K., Noda, A., Shipway, B. J., Slawinska, J., Wang, S. & Wyszogrodzki, A. (2011). Controls on precipitation and cloudiness in simulations of trade-wind cumulus as observed during RICO. *Journal of Advances in Modeling Earth Systems*, 3(2). doi:10.1029/2011MS000056.

Zelinka, M. D., Klein, S. A., Taylor, K. E., Andrews, T., Webb, M. J., Gregory, J. M. & Forster, P. M. (2013). Contributions of Different Cloud Types to Feedbacks and Rapid Adjustments in CMIP5. *Journal of Climate*, 26(14), 5007–5027. doi:10.1175/JCLI-D-12-00555.1.

Zelinka, M. D., Myers, T. A., McCoy, D. T., Po-Chedley, S., Caldwell, P. M., Ceppi, P., Klein, S. A. & Taylor, K. E. (2020). Causes of Higher Climate Sensitivity in CMIP6 Models. *Geophysical Research Letters*, 47(1). doi:10.1029/2019GL085782.

Zhang, G. J. & McFarlane, N. A. (1995). Role of convective scale momentum transport in climate simulation. *Journal of Geophysical Research: Atmospheres*, 100(D1), 1417–1426. doi:10.1029/94JD02519.

Zhu, P. (2015). On the Mass-Flux Representation of Vertical Transport in Moist Convection. *Journal of the Atmospheric Sciences*, 72(12), 4445–4468. doi:10.1175/JAS-D-14-0332.1.

Zipser, E. J. (1969). The Role of Organized Unsaturated Convective Downdrafts in the Structure and Rapid Decay of an Equatorial Disturbance. *Journal of Applied Meteorology*, 8(5), 799–814. doi:10.1175/1520-0450(1969)008<0799:TROOUC>2.0.CO;2.

Zuidema, P., Li, Z., Hill, R. J., Bariteau, L., Rilling, B., Fairall, C., Brewer, W. A., Albrecht, B. & Hare, J. (2012). On trade wind cumulus cold pools. *Journal of the Atmospheric Sciences*, 69(1), 258–280. doi:10.1175/JAS-D-

11-0143.1.

ZUIDEMA, P., TORRI, G., MULLER, C. & CHANDRA, A. (2017). A Survey of Precipitation-Induced Atmospheric Cold Pools over Oceans and Their Interactions with the Larger-Scale Environment. *Surveys in Geophysics*, 38(6), 1283–1305. doi:10.1007/s10712-017-9447-x.

Acknowledgements

This chapter is usually the place where PhDs get all emotional and fill page after page with all the people who were important in those last years (and even beyond) and the stories around them. But if you know me (and if you find yourself somewhere below that's probably the case), you know that I'm not a very chatty person who is into big words. Hence, please excuse the brevity, but be assured that these words still come from the heart!

First of all, to Louise Nuijens, my daily advisor: I'm proud to have been your first PhD here in Delft. It was a great journey on which I started out as quite a noob in atmospheric science and ended with this book. Right from the beginning, you always challenged me to dig into the details and to not content myself with a broad overview. I'm convinced that this was vital to the success of this project. Thanks also for giving me the opportunity to travel to France, Australia, Austria, Germany, Iceland, Greece and Barbados for conferences, workshops and field work.

Equal thanks go to my promotor, Pier Siebesma: Your tremendous experience and fresh view on my results always led to new ideas and approaches. Similarly, thanks go to the other co-authors of my papers and most direct collaborators and advisors, Stephan de Roode and Vishal Dixit! I'm also grateful to the members of my doctoral committee for taking the time to read and assess this thesis.

Collaborations and exchange with other researchers are what keep the science going. Thus, there are many more people who inspired me, gave feedback, made suggestions and criticised my work — both people from down corridor and people I met at workshops and conferences. The most important ones are: Bjorn Stevens, Cathy Hohenegger, Chris Bretherton, Daniel Kirshbaum, Daniel Klocke, Daniel McCoy, Graham Feingold, Harm Jonker, Irina Sandu, Jordi Vilà, Kai Lochbihler, Matthias Brueck, Peter Blossey, Raphaela Vogel, Sandrine Bony, Steven Böing, Sukanta Basu as well as the seven anonymous reviewers of 'my' papers.

Equally important for my scientific progress, but probably even more as friends are my colleagues from the CloudBrake project (a.k.a the cloud dummies). Right from the start until the end (and hopefully beyond!), there were Bea and Mariska, with whom I shared an office, went to conferences and even on holidays. I wish you two all the best for the remaining months of your PhD, you deserve to write a chapter like this one soon too. Later, we were joined by Vishal and Alessandro whom we gladly welcomed in our group.

Some more scientists that need to be thanked: First, all the participants of the 2017 summer school on climate dynamics in Les Houches: Thanks for four amazing weeks in the French Alps with excellent lectures, a 'hands-on' experience of convection and countless rounds of 'Secret Hitler'! Second, to the crew of the RV Meteor's cruise M161 from Barbados to the Azores, especially the radiosonde gang: Thanks for all the nights in

'our' bar or on the pensioner's bench, the weirdest and funniest dance classes and an introduction to pen-and-paper games. And third, the folks from Scientists4Future in our local group in Delft, at the KlimaatHelpdesk and in the national body: Thanks for all the enlightening discussions, energising meetings and empowering projects.

As I'm slowly drifting from the professional to the personal world, it's a good point to mention all those colleagues from GRS that made the last four years in Delft much less dull. Thanks to Antoon, Geiske, Inger, Jonathan, Julien, Maaike, Marcel, Ricardo, Steven, Thomas and Thore, to name but a few. Furthermore, thanks to Benjamin, Esther, Kathelijne and Mark for letting me be on the Snellius board with you — I can't wait to finally open that box with your present that I've already been storing for over a year.

There are people without whom we scientists would be absolutely lost: our wonderful support staff. Thanks to all current and former secretaries and managers at GRS: Debbie, Irma, Josine, Lidwien, Minke and Suzanne. I would also like to express my admiration to TU Delft's graduate school for managing to not influence the quality of this thesis in a negative way. A special acknowledgement goes to our IT expert Erwin who passed away last year and who always had an answer to any of my computer-related questions (however silly they may have been) within the shortest time.

I'd also like to thank my friends back in Germany. It was always relaxing and energising to come by for a visit, to show you around in Holland, go on holidays, have a night out or meet for board games or pen and paper. Cheers to Benedikt, Dominik, Fabienne, Julia, Katharina, Lukas, Patrick and Veit!

One person has been left out so far because he deserves a premium spot: Simon, my best friend, climbing buddy, holiday companion, lifestyle and dating coach (more successful on the former than the latter), tv and YouTube guide, virtual office mate during the pandemic and much else. Thanks for your charming annoyingness, your open ear, countless pep talks and patience with grumpy me! VIELEN DANK!

Last but not least, my whole family, first and foremost my parents, Jaqueline and Victor, my brother Leon but also my step parents, Katharina and Chris. Thanks for being my family, your enduring support and your love. Two more people from the Helfer clan deserve to be picked out: Thanks to my aunt Maria for the regular care packages from Germany and to my cousin Florian for picking me up when I fall.

After all, this chapter didn't turn out quite as short as I announced at the beginning. Maybe that means that I'm not as cold-hearted as I thought. Or it just shows how many persons it needs to obtain a PhD: definitely more than one! Thank you everyone, all the best to you and let's keep in touch!

Curriculum Vitæ

Kevin Christopher Helfer

15 March 1992	Born in Wipperfürth, Germany
1998–2002	Catholic Primary School Marienheide, Germany
2002–2011	Archiepiscopal St.-Angela-Gymnasium Wipperfürth, Germany
2008	Sunnybank State High School, Brisbane, Australia (study abroad)
2011–2014	Westfälische Wilhelms-Universität Münster, Germany Bachelor of Science in Geophsysics Bachelor Thesis: *Internally heated double-diffusive convection at infinite Prandtl number*
2014	University of California, Santa Barbara, USA Research internship
2014–2016	Westfälische Wilhelms-Universität Münster, Germany Master of Science in Geophsysics Master Thesis: *Double-diffusive convection in the finger regime at low buoyancy ratios*
2017–2021	Delft University of Technology, The Netherlands PhD Candidate

List of publications

First authored:

- **Helfer, K. C.** & Nuijens, L. (2021). The morphology of simulated cumulus conges-
  tus systems under wind shear. *Journal of Geophysical Research: Atmospheres*, in
  review. doi:10.1002/essoar.10506905.1.

- **Helfer, K. C.**, Nuijens, L. & Dixit, V. V. (2021). The role of shallow convection in
  the momentum budget of the trades from large-eddy-simulation hindcasts. *Quarterly
  Journal of the Royal Meteorological Society*, 147(737), 2490–2505. doi:10.1002/qj.4035.

- **Helfer, K. C.**, Nuijens, L., de Roode, S. R. & Siebesma, A. P. (2020). How wind
  shear affects trade-wind cumulus convection. *Journal of Advances in Modeling Earth
  Systems*, 12(12). doi:10.1029/2020MS002183.

Co-authored:

- Hu, F., **Helfer, K. C.**, Siebesma, A. P. & Hanssen, R. F. (2021). Multi-temporal SAR
  Interferograms with Extremely High Temporal Resolution: Impact of Tropospheric
  Delay on A Future Geosynchronous Mission. *Transactions on Geoscience and
  Remote Sensing*, in review.

- Stevens, B., Bony, S., Farrell, D., Ament, F., Blyth, A., Fairall, C., Karstensen, J.,
  Quinn, P. K., Speich, S., Acquistapace, C., Aemisegger, F., Albright, A. L., Bellenger,
  H., Bodenschatz, E., Caesar, K.-A., Chewitt-Lucas, R., de Boer, G., Delanoë, J.,
  Denby, L., Ewald, F., Fildier, B., Forde, M., George, G., Gross, S., Hagen, M.,
  Hausold, A., Heywood, K. J., Hirsch, L., Jacob, M., Jansen, F., Kinne, S., Klocke,
  D., Kölling, T., Konow, H., Lothon, M., Mohr, W., Naumann, A. K., Nuijens, L.,
  Olivier, L., Pincus, R., Pöhlker, M., Reverdin, G., Roberts, G., Schnitt, S., Schulz,
  H., Siebesma, A. P., Stephan, C. C., Sullivan, P., Touzé-Peiffer, L., Vial, J., Vogel,
  R., Zuidema, P., Alexander, N., Alves, L., Arixi, S., Asmath, H., Bagheri, G., Baier,
  K., Bailey, A., Baranowski, D., Baron, A., Barrau, S., Barrett, P. A., Batier, F.,
  Behrendt, A., Bendinger, A., Beucher, F., Bigorre, S., Blades, E., Blossey, P., Bock,
  O., Böing, S., Bosser, P., Bourras, D., Bouruet-Aubertot, P., Bower, K., Branellec,
  P., Branger, H., Brennek, M., Brewer, A., Brilouet, P.-E., Brügmann, B., Buehler,
  S. A., Burke, E., Burton, R., Calmer, R., Canonici, J.-C., Carton, X., Cato Jr., G.,
  Charles, J. A., Chazette, P., Chen, Y., Chilinski, M. T., Choularton, T., Chuang, P.,
  Clarke, S., Coe, H., Cornet, C., Coutris, P., Couvreux, F., Crewell, S., Cronin, T., Cui,
  Z., Cuypers, Y., Daley, A., Damerell, G. M., Dauhut, T., Deneke, H., Desbios, J.-P.,
  Dörner, S., Donner, S., Douet, V., Drushka, K., Dütsch, M., Ehrlich, A., Emanuel,
  K., Emmanouilidis, A., Etienne, J.-C., Etienne-Leblanc, S., Faure, G., Feingold, G.,
  Ferrero, L., Fix, A., Flamant, C., Flatau, P. J., Foltz, G. R., Forster, L., Furtuna, I.,
  Gadian, A., Galewsky, J., Gallagher, M., Gallimore, P., Gaston, C., Gentemann, C.,
  Geyskens, N., Giez, A., Gollop, J., Gouirand, I., Gourbeyre, C., de Graaf, D., de
  Groot, G. E., Grosz, R., Güttler, J., Gutleben, M., Hall, K., Harris, G., **Helfer, K. C.**,
  Henze, D., Herbert, C., Holanda, B., Ibanez-Landeta, A., Intrieri, J., Iyer, S., Julien, F.,
  Kalesse, H., Kazil, J., Kellman, A., Kidane, A. T., Kirchner, U., Klingebiel, M., Körner,

M., Kremper, L. A., Kretzschmar, J., Krüger, O., Kumala, W., Kurz, A., L'Hégaret, P., Labaste, M., Lachlan-Cope, T., Laing, A., Landschützer, P., Lang, T., Lange, D., Lange, I., Laplace, C., Lavik, G., Laxenaire, R., Le Bihan, C., Leandro, M., Lefevre, N., Lena, M., Lenschow, D., Li, Q., Lloyd, G., Los, S., Losi, N., Lovell, O., Luneau, C., Makuch, P., Malinowski, S., Manta, G., Marinou, E., Marsden, N., Masson, S., Maury, N., Mayer, B., Mayers-Als, M., Mazel, C., McGeary, W., McWilliams, J. C., Mech, M., Mehlmann, M., Meroni, A. N., Mieslinger, T., Minikin, A., Minnett, P., Möller, G., Morfa Avalos, Y., Muller, C., Musat, I., Napoli, A., Neuberger, A., Noisel, C., Noone, D., Nordsiek, F., Nowak, J. L., Oswald, L., Parker, D. J., Peck, C., Person, R., Philippi, M., Plueddemann, A., Pöhlker, C., Pörtge, V., Pöschl, U., Pologne, L., Posyniak, M., Prange, M., Quiñones Meléndez, E., Radtke, J., Ramage, K., Reimann, J., Renault, L., Reus, K., Reyes, A., Ribbe, J., Ringel, M., Ritschel, M., Rocha, C. B., Rochetin, N., Röttenbacher, J., Rollo, C., Royer, H., Sadoulet, P., Saffin, L., Sandiford, S., Sandu, I., Schäfer, M., Schemann, V., Schirmacher, I., Schlenczek, O., Schmidt, J., Schröder, M., Schwarzenboeck, A., Sealy, A., Senff, C. J., Serikov, I., Shohan, S., Siddle, E., Smirnov, A., Späth, F., Spooner, B., Stolla, M. K., Szkó lka, W., de Szoeke, S. P., Tarot, S., Tetoni, E., Thompson, E., Thomson, J., Tomassini, L., Totems, J., Ubele, A. A., Villiger, L., von Arx, J., Wagner, T., Walther, A., Webber, B., Wendisch, M., Whitehall, S., Wiltshire, A., Wing, A. A., Wirth, M., Wiskandt, J., Wolf, K., Worbes, L., Wright, E., Wulfmeyer, V., Young, S., Zhang, C., Zhang, D., Ziemen, F., Zinner, T. & Zöger, M. (2021). EUREC[4]A. *Earth System Science Data*, accepted. doi:10.5194/essd-2021-18.

- Dixit, V. V., Nuijens, L. & **Helfer, K. C.** (2021). Counter-gradient momentum transport through subtropical shallow convection in ICON-LEM simulations. *Journal of Advances in Modeling Earth Systems*, 13(6). doi:10.1029/2020MS002352.

- Stephan, C. C., Schnitt, S., Schulz, H., Bellenger, H., de Szoeke, S. P., Acquistapace, C., Baier, K., Dauhut, T., Laxenaire, R., Morfa-Avalos, Y., Person, R., Quiñones Meléndez, E., Bagheri, G., Böck, T., Daley, A., Güttler, J., **Helfer, K. C.**, Los, S. A., Neuberger, A., Röttenbacher, J., Raeke, A., Ringel, M., Ritschel, M., Sadoulet, P., Schirmacher, I., Stolla, M. K., Wright, E., Charpentier, B., Doerenbecher, A., Wilson, R., Jansen, F., Kinne, S., Reverdin, G., Speich, S., Bony, S. & Stevens, B. (2021). Ship- and island-based atmospheric soundings from the 2020 EUREC[4]A field campaign. *Earth System Science Data*, 13(2), 491–514. doi:10.5194/essd-13-491-2021.

Miscellaneous, non-peer-reviewed:

- **Helfer, K. C.** (2020). Do the media treat the crisis like a crisis? *Scientists4Future Delft blog*. `http://delft.scientists4future.nl/2020/11/16/do-the-media-treat-the-crisis-like-a-crisis/`

- **Helfer, K. C.** (2020). Can we make TU Delft carbon-neutral? *Scientists4Future Delft blog*. `http://delft.scientists4future.nl/2020/09/12/can-we-make-tu-delft-carbon-neutral/`

- **Helfer, K. C.** (2020). Onderzoeker over de grens — Atlantic. *ExtraCT*, 23(2), 70–71. `https://online.fliphtml5.com/emngs/uzgl/#p=70`

List of presentations

Oral presentations

- Nederlands Aardwetenschappelijk Congres, 13 March 2020, Utrecht, The Netherlands

- AES Seminar, Max Planck Institute for Meteorology, 1 October 2018, Hamburg, Germany

- European Geosciences Union General Assembly, 9 April 2018, Vienna, Austria

- BBOS Boundary Layer and Turbulence workshop, 6 April 2018, Wageningen, The Netherlands

Poster presentations

- BBOS Autumn Symposium, 24 October 2019, 's-Hertogenbosch, The Netherlands

- CFMIP Meeting on Clouds, Precipitation, Circulation, and Climate Sensitivity, 3 October 2019, Mykonos, Greece

- GRS/GSE Science for Society Research Day, 15 April 2019, Delft, The Netherlands (Best Poster Award)

- Understanding Clouds and Precipitation, 26 February 2019, Berlin, Germany

- GSE/GRS Research Day, 20 March 2018, Delft, The Netherlands

- Understanding and Modelling Atmospheric Processes, 28 February 2018, Lorne, Australia

- Geoscience and Remote Sensing Research Day, 12 May 2017, Delft, The Netherlands

Digital displays

- American Geophysical Union Fall Meeting, 14 December 2020

- EGU2020: Sharing Geoscience Online, 7 May 2020